PhD-FSTM-2021-047
The Faculty of Sciences, Technology and Medicine

DISSERTATION

Defence held on 08/07/2021 in Esch-sur-Alzette

to obtain the degree of

DOCTEUR DE L'UNIVERSITÉ DU LUXEMBOURG

EN PHYSIQUE

by

Cosme MILESI-BRAULT
Born on 1 March 1994 in Blois, (France)

OLD AND NEW ANTIFERROELECTRICS: EXPERIMENTAL STUDIES OF PHASE TRANSITIONS IN MODEL MATERIALS

Dissertation defence committee

Dr Mael Guennou, dissertation supervisor
Associate Professor, Université du Luxembourg

Dr Ludger Wirtz, Chairman
Professor, Université du Luxembourg

Dr Emmanuel Defaÿ, Vice Chairman
Unit leader, Luxembourg Institute of Science and Technology

Dr Mario Maglione
Director, Institut de Chimie de la Matière Condensée de Bordeaux

Dr Elena Buixaderas
Researcher, Institute of Physics of the Czech Academy of Sciences

Acknowledgements

These acknowledgements sections are always a bit strange to write and even cornier to read, but how better can I thank everyone who helped from up close or further away during the almost four years that lasted my Ph.D. project? I'll do my best to thank each and everyone of you, in no specific order.

First, I'd like to thank the members of jury who did not work directly with me, Drs. Elena Buixaderas and Mario Maglione, for accepting to review and assess my thesis work and participating to my defence. Thanks to Prof. Ludger Wirtz for being part of my CETs and raising points and questions which helped me go deeper in the understanding and importance of my work. Then, I'd like to thank you, Mael. for supervising me during my time in Luxembourg. I don't think anyone else could have helped me more than you to get a taste at how complex and rich antiferroelectrics are. I know I probably wasn't always up to your speed or standards but I truly am proud of the work we've achieved together. It was great working with you and I'll keep fond memories of our chats, jokes and beers shared. Thanks a lot to you Emmanuel for your all of your input during CETs and group talks, your management of the group and to allow me to be part of really nice outreach and cultural events such as the Science Festival, the Researchers' Days or Esch 2022. Our group is really special and I'll miss it when I leave. Thanks to you, Sebastjan, for all your input and guidance on the CSD synthesis. The unsuccessful first year and a half working on AFE BFO was tough but I'm glad we could get great results on PZO. Thanks a lot to you Constance for everything you taught me on a scientific level on multiferroics, Raman, how to make presentations, posters and graphs look *much* better, for putting me in contact with many great scientists and more personally for all the deep discussions and laughs. Thanks to you Hugo, my antiferroelectric colleague, for always answering all of my incessant questions about your vision of antiferroelectrics and your computations, for always giving such insightful talks and for being a great friend overall. Thanks to you and Laura for always being great hosts! Thanks to you Yves, Brahime, Nathalie, Evan, Virginie, Sophie, Brendan and all of our collaborators with whom I worked and/or published during these four years of PhD. Thanks a lot to you Stéphanie and Veronika for all of your work in the deposition of electrodes. I wouldn't have been able to get so nice results on sol-gel without your help and all of your work on the seed layer Nicolas, thanks so much for that! Thanks to you Jorge for everything you taught me directly or indirectly on ferroics. Thanks Torsten for the dielectric measurements, the school days at the Science Festival and for running the sadly now-defunct Ferroelectric Characterisation Cluster.

Thank you Carlos, I wouldn't have such a fun time in Luxembourg without you and both our wild and serious discussions, but also if you hadn't invited me to be a part of this flat I shared with so many great people. Thanks Mauro, you beautiful bastard, for everything. You know what, so I won't make you blush here, but you were one of the cornerstones of all the fun I had here. Our paths will cross again and I'm not sure the world is ready for it. Thanks so much for keeping it real. Conrad, du bist eine Marke. Thanks for being a great flatmate always full of energy and fun ideas. You and Naveen joined me in the middle of COVID time so it was not the ideal moment to share even crazier adventures but we really did have some fun all together. Naveen, I knew you'd be a great friend, flatmate and eating and drinking buddy as soon as we flew to Corsica and spent some more time together. Thanks for shining so bright during all of these fun evenings and long nights we had with everyone. We need to go on a trip somewhere as soon as possible. John, you're the next! We have and we'll have a great time in our short overlap.

Thanks to all of the Corsica ISOE luxembourgish team: Àlvar, Christina, Hugo, Naveen, Sangita and *of course* Youri. This 2-week summer school was so great thanks to all of you. I wish we could have done more of these trips all together. I'll miss the office most us shared and all of its kind drama, wild discussions and nice coffee breaks. Thanks Christina for all of our discussions around Raman and everything else, I think I can speak on behalf of everyone else than we missed you in the office... but that was for the best reason possible! I know you'll be the best mother for Clemens. Sangita, you might be the next one to defend! Either you or Àlvar. All the best to you both for the writing and this whole process of wrapping up four years of work, but I know you'll make us all proud. I'm not worried at all for both of you, you're going to do a great job. Thanks for the laughter, the stories and everything Youri, I'll dearly miss all of those. Thanks for the karaoke, the lunches and the fun nights Mónica. Thank Alfredo for all the fun and all of the scientific discussions, you're doing a great job with BFO. Don't let the reviewers destroy all your enthusiasm! Thanks Poorani, keep being great and partying and good luck for the rest of your Ph.D.! Merci Pierre for all the games, food and beer! I know I wasn't so available or punctual to our games but I truly and sincerely enjoyed them. Good luck Longfei, Diana and (now Ashwath!) for the rest of your Ph.D.İ'm sure you'll do great things here at LIST! Thanks to you Veronika, our neighbor, for always organising nice weekend gatherings which I sadly couldn't come to often enough... Thanks for the fun dinner and games evenings Natalya, sadly Covid prevented us from interacting too much and having many more. Special thanks to you Paola, for all the fun and the discussions. With you, Nayia and Conrad, we formed a great Berlin Team! I was lucky to spend my last trip pre-corona with you all. Thanks to all of the others who joined us for a while before leaving for other scientific adventures, especially Pablo and Miquel.

Thanks to my family, particular Mum & Dad, Clément, Mymy & Milo, Niko, Marion & Paul, MM, Carlos and all of the others for always supporting me during these four years and for trying your best to understand – with more or less success – what I was doing during these four years!

Thanks to my old CSC guys Jean-Philippe and Sébastien for the boardgames weekend mornings. Thanks to my former Uni holiday team: Aurore, Geoffrey, Léo, Dorian & Les Chloés, for nice mountain trips every single year that were a great breath of fresh air and change of pace. Thanks to you Pierre and Min for welcoming me in Grenoble and Basel and show me around your new homes. Thanks to you Léo, Kevin, Etienne, Val and Dorian for being my trusted D&Tea RPG group. I miss all of our non-sense together. I also would like to thank all of our Wine Cellar group: Adriaan, Jurġis, Pieter, James, Rikke, Marius, Eric, Liam, Lennart, Maxine, Cecilia & Mikael amongst many others, for the laughs, the banter, the food, the wild games and the so refreshing overall messy exuberance, especially during Eurovision times. Let's keep this thing running! Thanks to you Benoit, Etienne, Jules, Emilien, Antoine, Adeline, Samuel, Maxime and all of the others for the impromptu and/or traditional reunions during winter and summer breaks. Nostalgia has some good sometimes.

Abstract

Antiferroelectrics are a subcategory of ferroic materials that display no spontaneous polarisation due to antiparallel ionic displacements. These materials undergo an electric field-induced transition to a polar phase accompanied by the emergence of a spontaneous polarisation. As for ferroelectrics, heating up an antiferroelectric material above a certain temperature T_c will cause another phase transition towards a paraelectric phase.

Antiferroelectricity is currently the subject of a renewed interest, mostly due to a rising need of new smart materials for applications such as energy storage, electrocaloric cooling or micro-electronics. The most-studied antiferroelectric is lead zirconate $PbZrO_3$ perovskite. However, the understanding of its switching mechanism is still incomplete. In this work, we will first present our study on the sol-gel synthesis and characterisation of antiferroelectric polycrystalline thin films of canonical lead zirconate $PbZrO_3$. We will notably highlight the realisation of an in-plane switching of our antiferroelectric samples grown on transparent substrates, as well as the optical observation of this switching through birefringence changes.

On a more fundamental side, the oldest and best-known model of antiferroelectricity was defined by Kittel in 1951. No real unidimensional Kittel-like model material has, to our knowledge, been identified yet. We will detail our spectroscopic study of the lattice dynamics of francisite $Cu_3Bi(SeO_3)_2O_2Cl$ which combines several inelastic scattering experiments. We will then discuss how this study proves that francisite is, to our knowledge, the best candidate of a material displaying a displacive antiferroelectric phase transition.

Index

List of Figures

Introduction

In condensed matter and material physics, ferroic materials are of particular interest due to their rich physical properties at the crossroads of many different disciplines and interests. A ferroic material is one displaying a spontaneous physical quantity which disappears above a certain critical temperature due to a transition towards another phase of higher symmetry. This spontaneous physical quantity is polarisation for ferroelectrics, magnetisation for ferromagnets and strain for ferroelastics. On the application side, ferromagnets, ferroelastics and ferroelectrics communities all contribute to the development of new functional materials that can be used in a wide range of devices. Amongst other uses, ferroelectrics can be taken advantage of as capacitors, sensors, memories, actuators or surface acoustic wave filters in microelectronic applications. Ferromagnets can be used in hard drives or memories as a media for digital data storage. Macroscopic computational studies enabled by first- and second-principles calculations or phase field theory have recently played a major role in ferroics, by predicting or helping to explain certain newly-found phenomena such as magnetic and ferroelectric skyrmions, for instance. For ferroelectrics, more and more topics have risen in popularity in the last few decades, such as multiferroics, superlattices and domain walls creation and properties, notably due to the development of thin film processing.

Antiferroelectrics are ferroic materials that do not display a spontaneous polarisation but do undergo a phase transition to a high-symmetry phase above a certain temperature. This phase transition is accompanied by an anomaly in the dielectric permittivity of the material. Another transition to a polar phase can be induced by applying an electric field to the material and comes with the emergence of a spontaneous polarisation. The canonical example of an antiferroelectric is the perovskite lead zirconate $\mathrm{PbZrO_3}$which has been continuously studied since the 1950s. This material is of particular interest as it is part of the $\mathrm{PbZrO_3{-}PbZiO_3}$ solid solution that notably includes the broadly-used ferroelectric lead zirconate titanate $\mathrm{PbZr_xTi_{1-x}O_3}$ (PZT).

In the last years, antiferroelectrics have gained a rising interest due to the possibility and the need to store energy in solid-state devices and the global rising of cooling needs but are still much less investigated than ferroelectrics, partly due to a prior lack of applications exclusive to antiferroelectrics. This relative lack of study leads to some unanswered questions. First, even if lead zirconate $PbZrO_3$is the current model antiferroelectric perovskite, its antiferroelectric switching has still some blind spots. For instance, the symmetry of the polar phase of $PbZrO_3$is generally considered to be rhombohedral but there is little experimental proof currently available. The switching mechanism was extensively debated, including recent studies. This lack of information on the symmetry of the polar is not only important on a fundamental side but also because of it hindering the optimisation of devices, notably for material fatigue. On a more fundamental side, the first model of antiferroelectricity was proposed by Kittel in 1951. Yet, no uni-dimensional material was found to perfect match this model. For example, most current antiferroelectrics are also ferroelastics which does not agree with Kittel's model.

In this thesis, we will cover some of the fundamental and more applied aspects of antiferroelectricity by characterising experimentally two different model antiferroelectrics.

The first chapter will cover the fundamentals of ferroic and the subcategory of antiferroelectric materials. First, we will start by defining a ferroic materials and describe the different types of ferroics. We will then shortly describe the phenomenological Landau theory of phase transitions applied to ferroics and discuss the displacive or order-disorder character of ferroic materials. We will define antiferroelectricity and its experimental signatures, then cover the canonical example of lead zirconate $PbZrO_3$before shortly mentioning other antiferroelectric materials. We will highlight a few of the applications of antiferroelectrics discussed. Finally, we will summarise some of the relevant topics on antiferroelectricity and the objectives of this thesis.

In chapter II, we will describe the methods used in this experimental work. First, we will cover Chemical Solution Deposition (CSD) which is the synthesis methods used in this work to process polycrystalline thin films of $PbZrO_3$. We will discuss how x-ray diffraction techniques can help us characterise the structure, orientation and strain of our thin films. Then, we will highlight how to perform dielectric permittivity and polarisation measurements of thin films and which are the relevant parameters for antiferroelectric thin films. Raman spectroscopy and the underlying Stokes and anti-Stokes inelastic scattering, will be detailled as a way to measure phonon frequencies. Two synchrotron-based techniques, inelastic x-ray scattering and thermal diffuse scattering, will then be shortly described as other means to measure phonon frequencies and dispersions.

In chapter III, we will begin by a literature review on the sol-gel synthesis of $PbZrO_3$thin films. We will then discuss which parameters can influence the wide distribution of critical fields observed and also shortly review studies on the polar phase of lead zirconate. We will then present the synthesis and the characterisation of our films without any electric field before displaying the results of our dielectric measurements. The influence of the previously-reviewed parameters on the difference of critical fields observed in our films will be discussed.

To start chapter IV, we will review the literature on francisite materials with a special focus on the 115 K phase transition in $Cu_3Bi(SeO_3)_2O_2Cl$. Then, we will describe and discuss our spectroscopic study of this material focused on the soft-mode dynamics above and below the transition temperature. The atomic contributions to the soft-mode will be extracted from DFT-calculated eigenvectors and compared to the measured behaviour of the soft-mode frequency. Finally, these results will be summarised to highlight that $Cu_3Bi(SeO_3)_2O_2Cl$ is the current best candidate for a displacive antiferroelectric.

Chapter I

Antiferroelectric phase transitions

In that chapter, we will present and choose a working definition of our materials of interest, antiferroelectrics, in the particular framework of functional ferroic materials.

Before defining antiferroelectrics, we will take a few steps back and introduce the more general concept of ferroic materials and ferroic phase transitions. The three main sub-categories of ferroics will then be described. We will then quickly introduce Landau phenomenological model of ferroic phase transitions. An explanation of the different types of ferroic phase transitions, order-disorder or displacive, will be given.

The oldest definition of antiferroelectricity will then be presented, as well as the experimental criteria needed to prove a material antiferroelectric.

First-discovered antiferroelectric lead zirconate $PbZrO_3$and its properties will be presented. We will then review known antiferroelectrics and antiferroelectric-candidate materials.

Applications of antiferroelectrics will also be shortly summarised.

Finally, a few of the open questions regarding antiferroelectricity will be formulated, together with the main objectives of this work.

I.1 Ferroic phase transitions

I.1.a A spontaneous physical quantity induced by symmetry-breaking

Ferroic materials are materials with a prototypical high-symmetry phase that is paired to a ferroic phase of a lower point symmetry [1]. The phase transition from this prototypical phase to the ferroic one is accompanied by a symmetry-breaking of the system but also by the emergence of a physical quantity called order parameter. By definition, this symmetry has to be non-disruptive, i.e. without bond breaking.

This phase transition happens when the prototypical material cools down below a certain critical temperature called Curie temperature that will henceforth be noted T_c.

Domains in ferroic materials are parts of the crystal displaying homogeneous physical quantities. Below the transition, the ferroic material breaks into domains of different orientations, i.e. with different directions of order parameter. These domains can be switched between the different ferroic states by applying an external field (electric, magnetic, stress...) to the material. Varying this external field while measuring the conjugate physical quantity gives rise to an hysteretic behaviour.

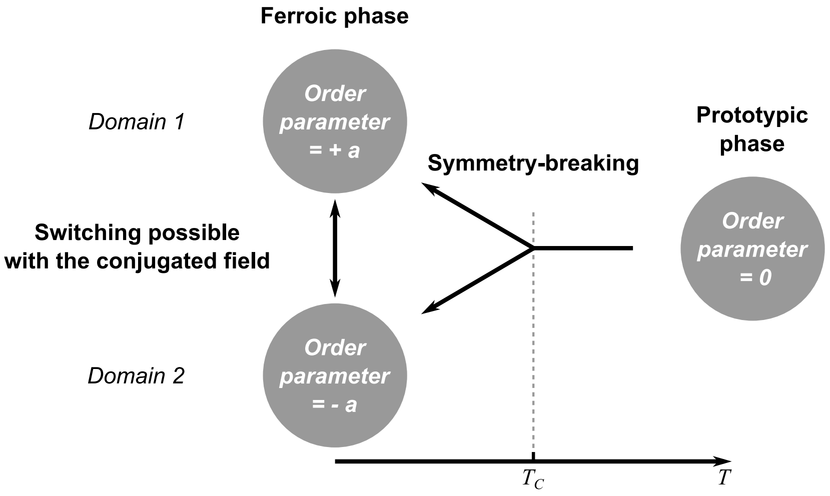

Figure I.1: Schematic principle of ferroicity, in the case of a ferroic with two possible ferroic states.

Ferroic materials can be classified according to the symmetries broken at the transition, the physical quantity used as order parameter and the conjugate field needed to switch the ferroic state, as shown in Table I.1.

We will now focus on three of the existing categories of ferroics. First, ferroelastics that break neither time-inversion symmetry nor inversion symmetry, and have a spontaneous strain ϵ. In ferromagnets, time-inversion symmetry is broken but space inversion is preserved, leading to a spontaneous magnetization $\vec{M}$. Finally, ferroelectrics break only inversion symmetry and display a spontaneous polarisation $\vec{P}$. These three types of ferroics will be discussed in a more detailed fashion later on, in specific subsections.

Ferrotoroidic materials are here set apart from the other ferroic materials as they are significantly less well-known. They break both time-inversion and inversion symmetry, which creates a spontaneous ferrotoroidic moment $\vec{T}$ [2]. As they are the least common ferroic materials, ferrotoroidics will not be discussed more thoroughly later on.

Some materials can also display several ferroic order parameters, i.e., multiple spontaneous physical quantities. In that case, they are said to be multiferroic.

Ferroic	Time-inversion sym.	Inversion sym.	Order parameter	Conjugate field
Ferroelastic	Conserved	Conserved	Strain ϵ	External stress σ
Ferromagnet	Broken	Conserved	Magnetization $\vec{M}$	Magnetic field $\vec{H}$
Ferroelectric	Conserved	Broken	polarisation $\vec{P}$	Electric field $\vec{E}$
Ferrotoroidic	Broken	Broken	Ferrotoroidic moment $\vec{T}$	Toroidal field $\vec{S}$

Table I.1: The four types of ferroic materials organised by symmetry-breaking

I.1.b Ferroelasticity

Ferroelastics are a type of ferroics that do not break inversion or time-inversion symmetry but do show a change of crystal family at the transition. This geometrical change gives rise to a spontaneous strain. Strain $\bar{\bar{\varepsilon}}$ is a tensor of rank 2 representing the unit cell deformation of the ferroelastic material compared to the reference prototypical paraelastic unit cell.

The typical ferroelastic presented is $Pb_3(PO_4)_2$ where, below 453 K, Pb atoms can shift inside the material in the bc-plane, as shown by the black arrows represented in Fig. I.2b, effectively lowering the symmetry of the crystal from a trigonal paraelastic $R\bar{3}m$ to a monoclinic ferroelastic $C2/c$ (or $C2$) structure and creating a spontaneous strain $e_s = \sum_i je_ij^2$, as shown in Fig. I.2a. This strain can be switched to different states by applying an external stress on the crystal, as shown by the hysteretic behaviour on Fig. I.2b.

Ferroelastics will tend to separate into domains with different strain states [4]. The domain orientation is governed only by the symmetry operations lost at the phase transition between the paraelastic and the ferroelastic phases, hence why materials undergoing the same symmetry descent will have the same domain structure. These domains can take different shapes, such as needles or stripes, which are linked to the elastic energy and hence will be unique to every material.

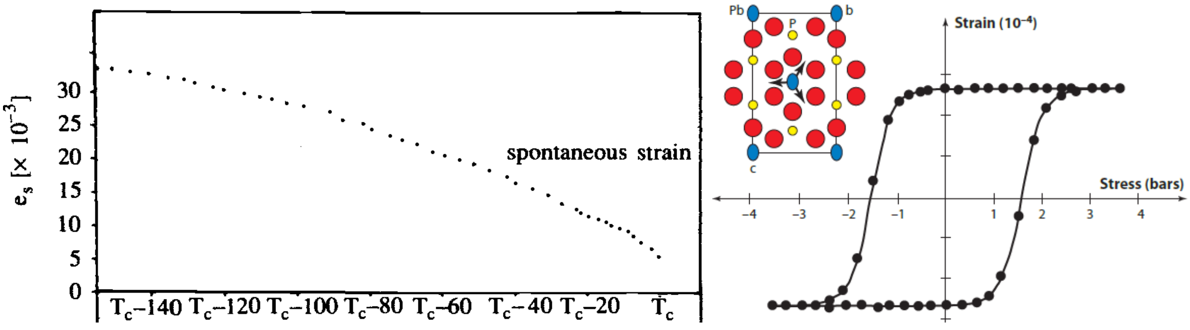

(a) (b)

Figure I.2: (a) Spontaneous strain in lead phosphate $Pb_3(PO_4)_2$. Adapted from [3]. (b) Ferroelastic switching of $Pb_3(PO_4)_2$. The arrows represent lead shifts at the ferroelastic transition. Adapted from [4].

I.1.c Ferromagnetism

Ferromagnets are ferroics that break the time-inversion symmetry. The prototypical phase is here called paramagnetic. A spontaneous magnetization M_s rises through this loss of symmetry (see Fig. I.4a) and the conjugate field is the magnetic field $\vec{H}$. This magnetization is carried by spins that are arranged in the crystal network.

When spins are randomly oriented, the system is paramagnetic as it has in average zero magnetization: $M = 0$. However, if spins all align in the same direction, the system is a ferromagnet (Fig. I.3).

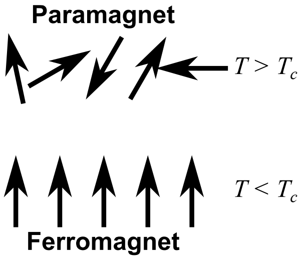

Figure I.3: Schematic representation of spin lattices leading to ferromagnetism.

Applying $\vec{H}$ in the opposite direction will flip spins in the direction of the magnetic field, when the magnitude of $\vec{H}$ is above a threshold value of the magnetic field, called generically critical field or coercive field. An hysteretic behaviour is then expected when measuring magnetization and applying a varying magnetic field, see Fig. I.4b.

Transition metals (iron, cobalt, nickel...), rare-earths (terbium, gadolinium, dysprosium...) and some alloys composed of these atoms are often ferro- or antiferromagnets.

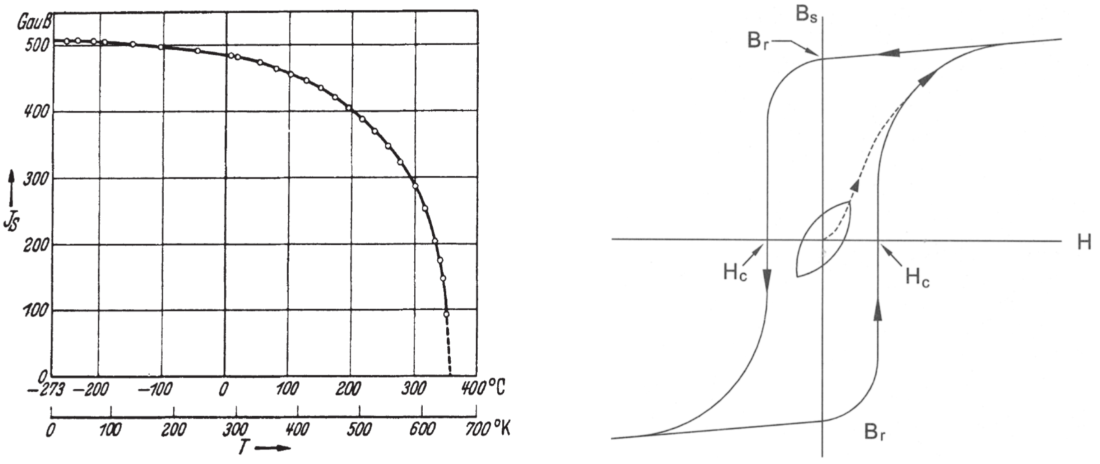

(a) (b)

Figure I.4: (a) Temperature-dependency of the spontaneous magnetization of nickel. Adapted from [5]. (b) Typical ferromagnetic hysteresis loop. Adapted from [1].

Antiferromagnetism

Spins aligned in an antiparallel fashion give an antiferroic system: an antiferromagnet, see Fig. I.5a. Here, the net total magnetization is zero below the critical Néel temperature T_c but the magnetization of each sub-lattice is non-zero.

Depending on the way the spin arrange themselves in the crystal lattice, different types of antiferromagnetism exist, as shown in Fig. I.5b. A-type antiferromagnetism can be seen as an alternance of ferromagnetic planes of opposite magnetisation. In B-type antiferromagnetism, lines of colinear spins have nearest neighbouring lines of opposite magnetisation. In a G-type, every spin has nearest neighbouring spins of opposite directions.

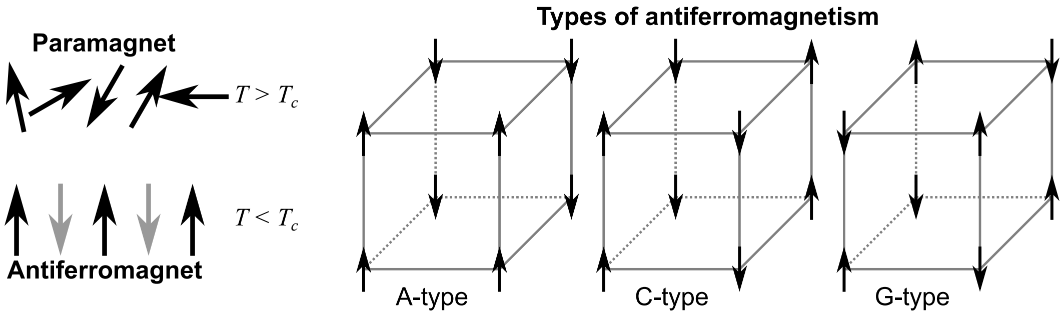

(a) (b)

Figure I.5: (a) Schematic representation of ferromagnetic 2D spin lattices above and below T_c. (b) Three types of 3D spin networks lead to the three types of antiferromagnetism.

I.1.d Ferroelectricity

Ferroelectrics are a type of ferroics for which the inversion symmetry breaking allows a switchable electrical polarisation to develop (see Fig. I.2a). Any polar space group allows a spontaneous polarisation P_s to build up inside the crystal unit cell. If that polarisation can be switched with an applied electric field, the material is then a ferroelectric. It is worth noting that the polarisation of a ferroelectric will vary as temperature changes, creating a voltage upon cooling or heating: any ferroelectric is also a pyroelectric. Also, any stress (respectively electric field) applied on a ferroelectric will lead to a change of polarisation and create a voltage (respectively deform the material): this is the piezoelectric effect, also present in any ferroelectric.

Ferroelectrics break into domains due to depolarising fields and electrical boundary conditions. As in ferroelastics and ferromagnets, these domains can be switched by application of an external electric field, as shown in Fig. I.6b. Important quantities are annotated on the figure. Remnant polarisation P_r is the macroscopic polarisation at zero electric applied field, coercive field E_c is the electric field at zero polarisation, which corresponds to the minimum field to apply to switch the ferroelectric state, and the saturation polarisation P_s is the extrapolation to zero field of the maximum polarisation.

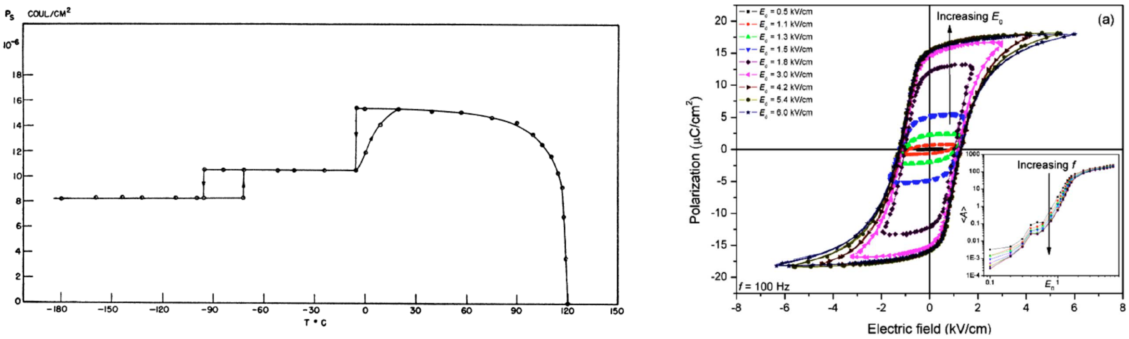

(a) (b)

Figure I.6: (a) Spontaneous polarisation of $BaTiO_3$ with respect to temperature. Each jump in spontaneous polarisation is due to a ferroelectric to ferroelectric phase transition and the disappearance of the spontaneous polarisation at $T_c \approx 100\,°C$ highlights the ferroelectric to paraelectric phase transition. Adapted from [6]. (b) Ferroelectric switching of {001}-oriented single crystals of $BaTiO_3$. Adapted from [7].

Model ferroelectrics in the perovskite family are barium titanate $BaTiO_3$ and lead titanate $PbTiO_3$, which will be presented later on. Lead zirconate titanate $Pb(Zr_xTi_{1-x})O_3$ (or PZT) and lithium niobate $LiNbO_3$ are also ferroelectrics widely used in applications. Ferroelectrics polymers [8], such as PVDF, are also of increasing interest for research and applications, due to their low costs, ease of production and mechanical flexibility.

It is worth noting that many ferroelectrics are actually also ferroelastics. This coupling of polarisation and strain is particularly important for piezoelectric applications but also for its effect on the material domain structure.

I.1.e Landau theory in ferroics

Landau theory is a phenomenological mean-field model based on the thermodynamics and symmetries of the system free energy $\mathcal{F}$. In that section, we will shortly introduce Landau theory, without rederiving it fully, and in the specific case of uni-dimensional ferroics near the prototypical to ferroic phase transition, following reference [9].

Given the previous approximations, the free energy of the system can be developed as a Taylor expansion of the ferroic order parameter η. Below T_c, the two ferroic states of order parameter $+\eta$ and $-\eta$ have the same energy, leading to all odd powers of η to be zero, by symmetry. Indeed, these odd terms would induce an asymmetry in the free energy development that would stabilize preferentially some ferroic states over others.

Hence, the following formulation of the free energy for a ferroic with an order parameter η:

$$\mathcal{F} = \frac{1}{2}\alpha\eta^2 + \frac{1}{4}\beta\eta^4 + \frac{1}{6}\gamma\eta^6 + ... \tag{I.1}$$

Around T_c, it is also assumed that only the coefficient α associated to η^2 has a linear dependency with respect to the temperature T, i.e. $\alpha = \alpha_0(T - T_c)$:

$$\mathcal{F} = \frac{1}{2}\alpha_0(T - T_c)\eta^2 + \frac{1}{4}\beta\eta^4 + \frac{1}{6}\gamma\eta^6 + ... \tag{I.2}$$

If an external field h conjugate to the order parameter η is applied to the system, we need to add the coupling term $-\eta h$ to Eq. (I.2). Generally, α and γ are positive or null while The sign of β will determine the type of the phase transition. Truncating above the fourth order will give the potential "2-4" $\mathcal{F} = \frac{1}{2}\alpha_0(T - T_c)\eta^2 + \frac{1}{4}\beta\eta^4$. Above the sixth order, the potential "2-4-6" is: $\mathcal{F} = \frac{1}{2}\alpha_0(T - T_c)\eta^2 + \frac{1}{4}\beta\eta^4 + \frac{1}{6}\eta^6$.

Continuous (second-order) phase transition

For the sake of the example, we will prove the stability of the different phases above and below T_c in the simple case of a unidimensional 2-4 Landau potential. In such a potential, the coefficient β has to be strictly positive for the system to be stable. As the free energy describes the system, looking at the mathematical stability of $\mathcal{F}$ will give information on the physical stability of the different phases of the ferroic material. At equilibrium, the system will be at an extremum of the potential, i.e. $\left(\frac{\partial F}{\partial \eta}\right)_{eq} = 0$.

$$\left(\frac{\partial F}{\partial \eta}\right)_{eq} = \alpha_0(T - T_c)\eta_{eq} + \beta\eta_{eq}^3 = 0 \tag{I.3}$$

$$\Longrightarrow \begin{cases} \eta_{eq} = 0 \\ \eta_{eq} = \pm\sqrt{\frac{\alpha_0}{\beta}(T_c - T)} \end{cases} \tag{I.4}$$

Extrema of $\mathcal{F}$ are reached for these three values of the ferroic order parameter: $\eta_{eq} = 0$, $\eta_{eq} = +\sqrt{\frac{\alpha_0}{\beta}(T_c - T)}$ (if $T_c < T$) or $\eta_{eq} = -\sqrt{\frac{\alpha_0}{\beta}(T_c - T)}$ (if $T_c < T$). Now, to find the minima of the energy, we need to check if these extrema are stable, i.e. if $\left(\frac{\partial^2 F}{\partial \eta^2}\right)_{eq} > 0$.

$$\left(\frac{\partial^2 F}{\partial \eta^2}\right)_{eq} = \alpha_0(T - T_c) + 3\beta\eta_{eq}^2 > 0 \tag{I.5}$$

$$= \begin{cases} \alpha_0(T - T_c) + 0 > 0 \\ \alpha_0(T - T_c) + 3\beta\frac{\alpha_0}{\beta}(T_c - T) \end{cases} \tag{I.6}$$

$$= \begin{cases} \alpha_0(T - T_c) > 0 \text{ true only if } T > T_c \\ 2\alpha_0(T_c - T) > 0 \text{ true only if } T < T_c \end{cases} \tag{I.7}$$

These stability conditions confirm that above T_c, the order parameter $\eta_{eq} = 0$ is stable i.e, the material is in its prototypical phase. Below T_c, the order parameter has a value different from zero ($\eta_{eq} = \pm\sqrt{\frac{\alpha_0}{\beta}(T_c - T)}$) which indicates that the ferroic phase is the most stable. The evolution of the order parameter η with respect to T is represented on Fig. I.7.

Susceptibility χ of the material for a second-order phase transition

When a field h is applied to a ferroic of order parameter η, the material will have a response to the field, measured as the susceptibility χ defined by the relation $\chi = \frac{\partial \eta}{\partial h}$.

In ferroelectrics, the dielectric susceptibility χ is linked to the polarisation P, the electric field E and the vacuum permittivity ε_0 via the following relation: $P = \varepsilon_0\chi E$. In that case, χ is directly linked to the material permittivity $\varepsilon_r = 1 + \chi$.

Let's now determine χ above and below T_c for a second-order ferroic transition driven by a 2-4 potential with $\beta > 0$ and field-coupling term $-\eta h$. At equilibrium, i.e. when $\frac{\partial F}{\partial \eta} = 0$, we have:

$$\frac{\partial F}{\partial \eta} = \alpha\eta + \beta\eta^3 - h = 0 \Longrightarrow h = \alpha\eta + \beta\eta^3$$

Deriving with respect to h, we obtain:

$$\begin{aligned}
\frac{\partial}{\partial h}h &= \frac{\partial}{\partial h}(\alpha\eta + \beta\eta^3) \\
1 &= \frac{\partial \eta}{\partial h}\frac{\partial}{\partial \eta}(\alpha\eta + \beta\eta^3) \\
1 &= \frac{\partial \eta}{\partial h}\frac{\partial}{\partial \eta}(\alpha\eta + \beta\eta^3) \\
1 &= \chi(\alpha + 3\beta\eta^2) \\
\Longrightarrow \chi &= \frac{1}{\alpha + 3\beta\eta^2} = \frac{1}{\alpha_0(T - T_c) + 3\beta\eta^2}
\end{aligned}$$

At small fields, we have $h \longrightarrow 0$, meaning that $\eta \longrightarrow \eta_{eq}$:

- For $T > T_c$, $\eta \longrightarrow \eta_{eq} = 0$ hence $\chi \longrightarrow 1/\alpha_0(T - T_c)$
- For $T < T_c$, $\eta^2 \longrightarrow \eta_{eq}^2 = -\alpha_0(T - T_c)/\beta$ hence $\chi \longrightarrow -1/2\alpha_0(T - T_c)$

The susceptibility χ follows a Curie-Weiss law ($\chi \propto 1/(T - T_c)^\gamma$) around T_c with an exponent γ of 1, in the limit of small applied fields. It is also important to note the link between susceptibility χ and the second derivative of the Landau free energy with respect to the ferroic order parameter η (see also Fig. I.7):

$$\frac{\partial^2 F}{\partial \eta^2} = \alpha_0(T - T_c) + 3\beta\eta^2 = \frac{1}{\chi}$$

.

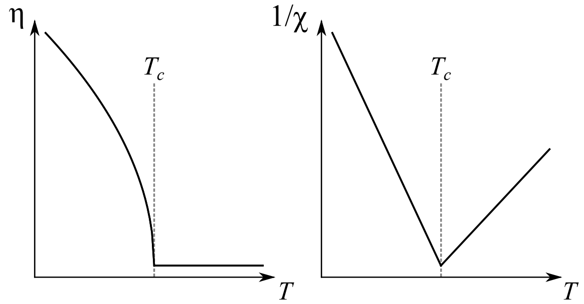

Figure I.7: Schematic temperature-dependency of order parameter η and $1/\chi = \frac{\partial^2 F}{\partial \eta^2}$ for a second-order transition driven by a 2-4 Landau potential.

Order of the phase transition

In Eq. I.2, for $\beta > 0$, the phase transition is discontinuous (i.e., first-order), for $\beta < 0$ it is continuous (i.e., second-order) and for $\beta = 0$ it is tricritical. 2-4-6 potentials are represented in those three cases on Fig. I.8a. For any order of the phase transition, $\mathcal{F}$ will still show a double well below T_c and a unique minimum above.

For first-order phase transitions, the order parameter η displays a discontinuity at T_c as well as the susceptibility χ, see Fig. I.8b. This discontinuity is linked to the latent heat released or absorbed at the ferroic phase transition.

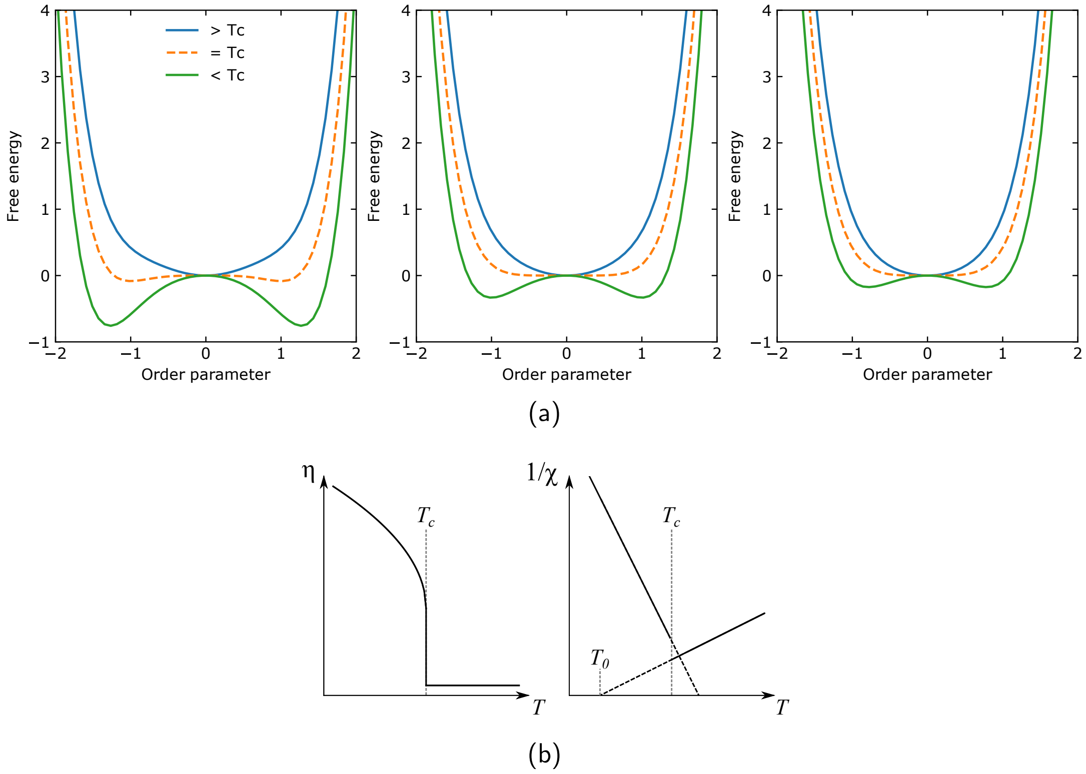

Figure I.8: (a) Schematic representation of the free energy above, at and below T_c in a first-order (left), tricritical (middle) and second-order (right) phase transition. (b) Schematic temperature-dependency of order parameter η and $1/\chi$ for a first-order phase transition.

I.1.f Order-disorder vs displacive phase transitions

Ferroic phase transitions can be divided in two broad categories of phase transitions: order-disorder and displacive phase transitions [10].

We can model ferroic phase transitions by assuming that the crystal is composed only of atoms interacting through harmonic forces, i.e. springs. The rest of the crystal that is invariant through the ferroic phase transition is simply represented by a double-well potential V, see Fig. I.9.

Below T_c, atoms fall into the potential wells, creating a non-zero order parameter for ferroics (or, in the case of an antiferroic, atoms fall in alternance on each side of the potential, leading to $\eta = 0$).

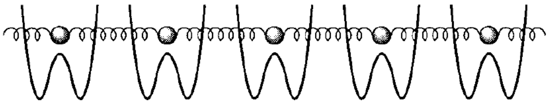

Figure I.9: Schematic model of a crystal. Adapted from [10].

The Hamiltonian representing this system can be written as the sum of the kinetic Hamiltonian $\mathcal{H}_{kinetic}$, the potential V created by the crystal structure and the nearest-neighbour interaction Hamiltonian $\mathcal{H}_{interaction}$ to:

$$\mathcal{H} = \mathcal{H}_{kinetic} + \mathcal{H}_{interaction} + V \tag{I.8}$$

Let's note u the vector for which any component u_i represents the atomic displacement of the atom i compared to its equilibrium position ($u_i = 0$). Then each term of the Hamiltonian can be written as:

$$\mathcal{H}_{kinetic}(u) = \frac{1}{2}\sum_i m\dot{u}_i^2$$

$$\mathcal{H}_{interaction}(u) = \frac{1}{2}\sum_{i \neq j} J(u_i - u_j)^2$$

$$V(u) = \sum_{i \neq j}(-\frac{1}{2}\alpha u_i^2 + \frac{1}{4}\beta u_i^4)$$

Depending on which terms dominate in Eq. (I.8), two limit cases will define the two models of ferroic phase transition:

- Displacive phase transition ($H_{interaction}(u) \gg V(u)$): interactions between the atoms driving the phase transition are much stronger in magnitude than the forces due to the crystal potential. Above T_c, atoms vibrate around the origin of the potential, leading to an order parameter value $\eta = 0$. The closer to the transition, the lower the frequency ω of that vibration will be: this vibration, i.e. the phonon mode softens. It can be shown that ω^2 is directly proportional to the second-derivative of the Landau free energy $\frac{\partial^2 F}{\partial \eta^2}$, as treated previously. Below T_c the potential will stop being negligible and will shift the average position of the atomic vibrations until every atom falls into the same potential well. See Fig. I.10.

Figure I.10: Schematic model of a displacive phase transition throughout a temperature decrease. Adapted from [10].

- Order-disorder phase transition ($V(u) \gg H_{interaction}(u)$): interactions between atoms are negligible compared to the forces created by the potential. Then, above T_c the atoms randomly fall in either potential wells, creating an average zero order parameter. At every temperature the atoms are localised in one of the potential wells, so it is possible to model these as spins in an Ising model. As temperature lowers below T_c, the strength of short-range spin-spin interactions increases and some spins will spend creating clusters of atoms with homogeneous order parameter direction until the whole crystal shows a single direction of order parameter. In that case, there is no softening of a phonon mode but the flipping of the spins slows down: there is a softening of a relaxation mode. See Fig. I.11.

Figure I.11: Schematic model of an order-disorder phase transition throughout a temperature decrease. Adapted from [10].

Ferromagnetic and antiferromagnetic phase transitions are order-disorder phase transitions as spins organise themselves through nearest-neighbour interactions. Moreover, spins are intrinsic to electrons so cannot become equal to zero: this is why there is no displacive phase transition in ferromagnets. The Ising model that is often used to describe some ferromagnets is a typical order-disorder model.

Ferroelectric phase transitions can be either displacive, order-disorder (or an intermediate case) as shown in the following section.

PbTiO$_3$: a model displacive ferroelectric perovskite

Above $T_c \approx 765\,\mathrm{K}$, PbTiO$_3$ has a cubic perovskite ABO$_3$ structure where A and B are cations respectively placed in the corners and center of the cubic cell. Oxygen atoms form an octahedral cage around the B cation site, as shown in Fig. I.12a. Below T_c, the unit cell extends in the $[001]_{\mathrm{cubic}}$ direction, becoming tetragonal (ratio $c/a = 1.06$) and developing a ferroelectric polarisation of up to around $85\,\mu\mathrm{C\,cm^{-1}}$ [11] due to off-center displacements of titanium, as shown on Fig. I.12b.

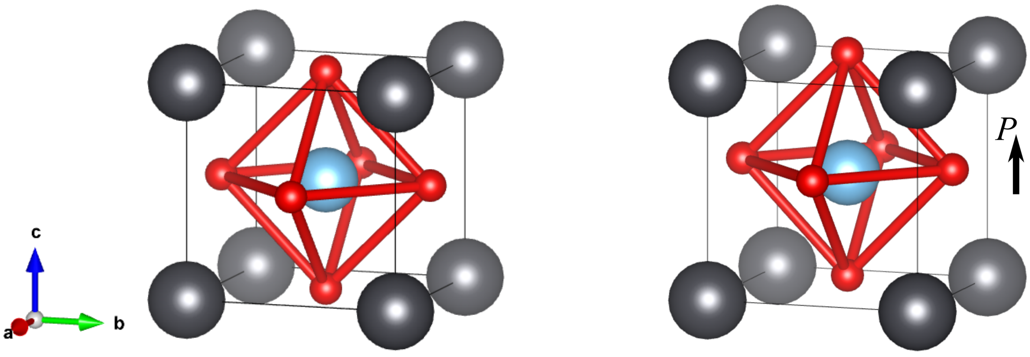

(a) (b)

Figure I.12: Perovskite structure of PbTiO$_3$ in the (a) cubic paralectric phase and in the (b) tetragonal ferroelectric phase. Grey spheres represent lead atoms, cyan are titanium and red are oxygen.

The paraelectric to ferroelectric phase transition is driven by the polar soft-mode linked to these Ti displacements [12, 13]. Indeed, the linear relationship between phonon frequency squared ω^2 ($\propto \frac{\partial^2 F}{\partial \eta^2} \propto \frac{1}{\chi}$) and temperature T, visible on Fig. I.13b, is the expected signature of a displacive phase transition.

KH$_2$PO$_4$: a model order-disorder ferroelectric

Potassium dihydrogen phosphate KH$_2$PO$_4$ (KDP) has a ferroelectric phase transition below $T_c \approx 123\,\mathrm{K}$. On Fig. I.14a are displayed both the structure above and below T_c. At the transition, it can be seen that P(OH)$_4$ groups rotate along the c-axis in antiphase, breaking the H-H bonds

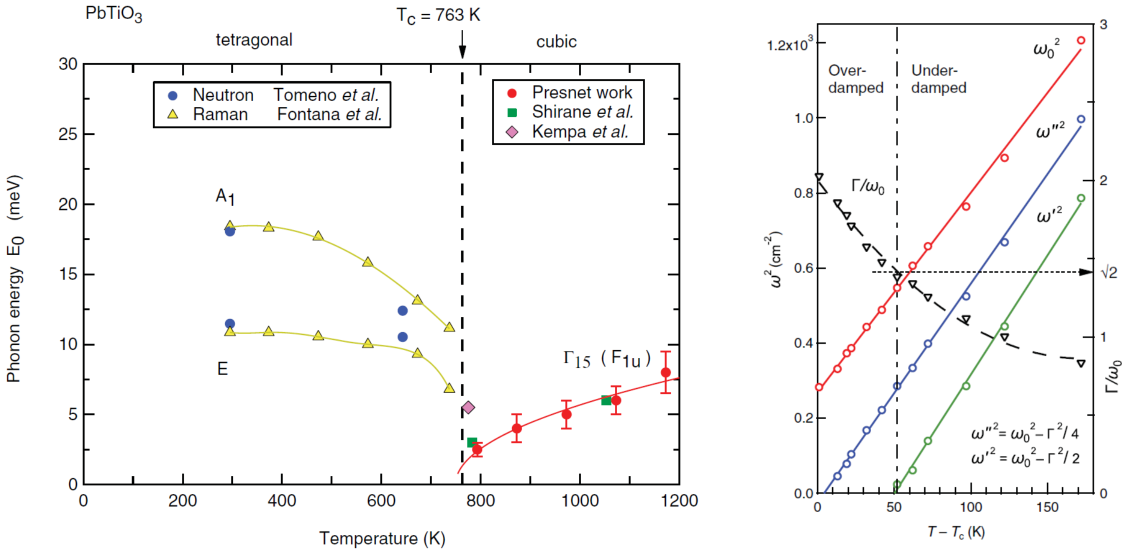

(a) (b)

Figure I.13: (a) Characterisation of the polar soft-mode energy driving the displacive ferroelectric phase transition in $PbTiO_3$. Adapted from [12]. (b) Temperature-dependency of ω^2 of the polar soft-mode above T_c. Adapted from [13].

from the paraelectric phase to create OH-O bonds along the [110] directions. In that structure, the proton H is trapped into the double potential-well inherent to the OH-H hydrogen bond and is barely influenced by the rest of the crystal: following the previous definition of a purely order-disorder phase transition. These protons H then act as the electric dipoles of the ferroelectric phase and develop the spontaneous polarisation seen in KDP (Fig. I.14c) and can also be switched by application of an electric field.

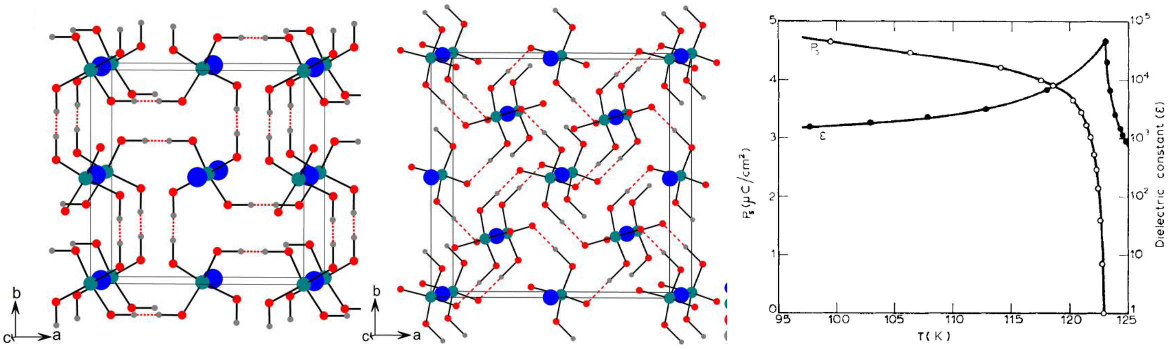

(a) (b) (c)

Figure I.14: Structure of KH_2PO_4 in the (a) prototypical paraelectric phase and in the (b) ferroelectric phase. Adapted from the supporting information of reference [14]. (c) Dielectric constant and polarisation of KH_2PO_4 with respect to temperature. Adapted from [15].

Mixed phase transition

Order-disorder and displacive phase transitions are only the two extreme limits of the harmonic crystal model presented in that section. Indeed, in most ferroics, phase transitions have neither a fully order-disorder nor a fully displacive behaviour.

Barium titanate BaTiO$_3$ is one of the most-studied ferroelectrics and is an example of a material that has a mixed order-disorder and displacive character, as shown by first-principles calculations performed in Ref. [16]. To come to that conclusion, the authors calculate the temperature-dependency of phonon modes at different reciprocal space coordinates $\vec{k}$. For an order-disorder system, a variation of the whole phonon branch is expected with temperature while for a ferroelectric displacive phase transition, only a small portion of the Brillouin zone around the soft-mode located at the Γ point will have high thermal fluctuations. The authors find a behaviour that is clearly an intermediate case, with some phonon branches that soften up to the Brillouin zone boundary in the $\Gamma - R$ direction, for instance. Nuclear magnetic resonance (NMR) experiments also confirmed this coexistence of displacive and order-disorder character in BaTiO$_3$, see Ref. [17].

I.2 Definition of antiferroelectricity

In this section, antiferroelectric phase transitions will be presented through their first model developped by Kittel and some of its limits. The typical experimental signatures of antiferroelectricity will be summarised.

I.2.a Kittel's model of oppositely polarised sub-lattices

In 1951, Charles Kittel formulated the first model for antiferroelectricity [18]. He defines an "antiferroelectric state as one in which lines of ions in the crystal are spontaneously polarised, but with neighboring lines polarised in antiparallel directions, so that the spontaneous macroscopic polarisation of the crystal as a whole is zero" (direct quote from [18]). This definition can be understood as a separation of the crystal lattice in two sub-lattices a and b with polarisations P_a and P_b, respectively, see Fig. I.15.

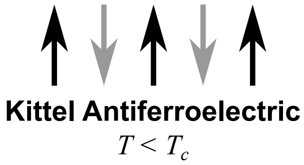

Figure I.15: Schematic Kittel model of a unidimensional antiferroelectric.

Kittel proposed a development of the free energy (for second-order transition) describing this antiferroelectric system using the polarisation of sub-lattices P_a and P_b as order parameters (terminology has been modified for coherence with I.1.b):

$$\mathcal{F} = \alpha(P_a + P_b)^2 + \beta P_a P_b + \gamma(P_a + P_b)^4 - (P_a + P_b)E \tag{I.9}$$

From the study of this potential, Kittel extracts that the dielectric susceptibility χ, for second-order phase transitions (see also Fig. I.17a), displays an anomaly at T_c following:

$$\chi = \begin{cases} \frac{1}{\beta - 2\lambda(T - T_c)} \text{ when } T < T_c \\ \frac{1}{\beta + \lambda(T - T_c)} \text{ when } T > T_c \end{cases} \tag{I.10}$$

Kittel also formulates a Landau potential for first-order phase transitions and derives an expression of χ on both sides of the transition.

In his reference book [19], Kittel notes the important difference between an antipolar structure and an antiferroelectric material. Per se, an antipolar space group does not exist on its own [20] but the term "antipolar space group" or "antipolar structure" is sometimes used for non-polar space groups that are related to polar space groups by simple antiparallel ion displacements.

I.2.b Phenomenological signatures of antiferroelectricity

In that section, we will highlight the experimental signatures that are commonly accepted to prove that a material is antiferroelectric..

Antiparallel displacement of ions in the AFE phase

In the paraelectric phase, the material has a non-polar symmetry. Below T_c, antiparallel ion displacements will put these ions in polar sites and the unit cell will be expanded to compensate the polarisation.

Dielectric anomaly between two non-polar phases

Both paraelectric and antiferroelectric phases are non-polar but have different dielectric behaviour. This translates to an anomaly in the dielectric constant at the transition temperature T_c.

If the dielectric constant is continuous, it is the signature of a second-order phase phase transition, as shown on Fig. I.17a, while a discontinuity indicates a first-order phase transition.

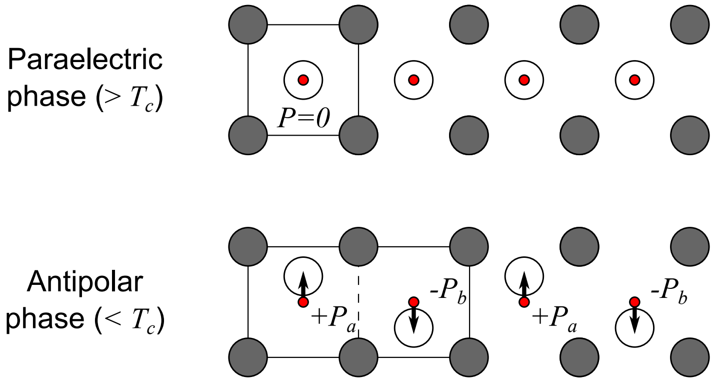

Figure I.16: Schematic antiparallel displacements of ions. Red dots represent the centre of each square cell and arrows the polarisation created by the ion displacements. Full black lines highlight the doubling of the unit cell below T_c.

It is of interest to note that an antiferroelectric phase transition should not have a dielectric constant tending to infinity at T_c, in contrast with ferroelectrics. Indeed, according to section I.1.e, the susceptibility of a ferroelectric follows a Curie-Weiss law and hence diverges at T_c. In his model [18], Kittel proposes a susceptibility with a finite value at T_c, as shown in Fig. I.17a. It is important to note that Kittel's model does not perfectly model the experimental shape of dielectric response. In [21], a model of antiferroelectric phase transitions describing more accurately the experimental dielectric anomaly is proposed and shown in Fig. I.17b.

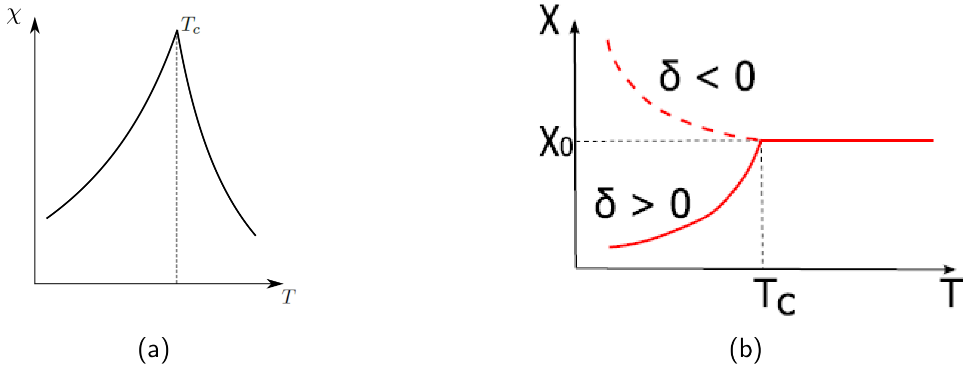

(a) (b)

Figure I.17: Schematic susceptibility for a second-order antiferroelectric to paraelectric phase transition according to (a) Kittel's model and (b) model from Ref. [21].

Antiferroelectric switching – the "double hysteresis loop"

This is by far the most famous antiferroelectric signature. Without any field, the measured polarisation is zero. At small values of the electric field, polarisation will rise following a linear dielectric behaviour. However, above a certain critical field $E_{AFE \to FE}$, the material switches to its polar phase, i.e. all Kittel's "electric dipoles" start flipping in the direction of the electric field until all are switched: polarisation saturates. If we then decrease the electric field, the polar phase will stay stable even below $E_{\mathrm{AFE} \to \mathrm{FE}}$ and the material will switch back to the antiferroelectric phase only below a critical field name $E_{\mathrm{FE} \to \mathrm{AFE}}$. This stability of the polar phase creates the hysteretic behaviour, i.e. the "double hysteresis loop".

However, the real signature of antiferroelectric switching is the field-induced phase transition from a non-polar to a polar phase and not the often-visible hysteretic behaviour of this switching. For instance, in squaric acid $C_4H_2O_4$, the polarisation curve does not display any kind of hysteresis [22], but does display a change of polarisation characteristic of a field-induced non-polar to polar phase transition. This confusion is sometimes found in the literature.

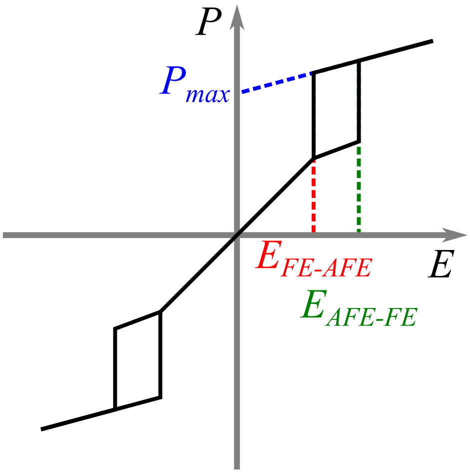

Figure I.18: Schematic antiferroelectric hysteresis polarisation curve.

I.3 Example of the canonical antiferroelectric: lead zirconate PbZrO_3

I.3.a Crystallographic structure

Lead zirconate PbZrO_3 was first said to be antiferroelectric in a paper of Shirane from 1951 [23]. In its paraelectric high-temperature phase ($T_c \approx 505\,\mathrm{K}$), PbZr$O_3$ has a typical cubic $Pm\bar{3}m$ perovskite structure with a lattice parameter $a_{cubic} = 4.16\,\text{Å}$.

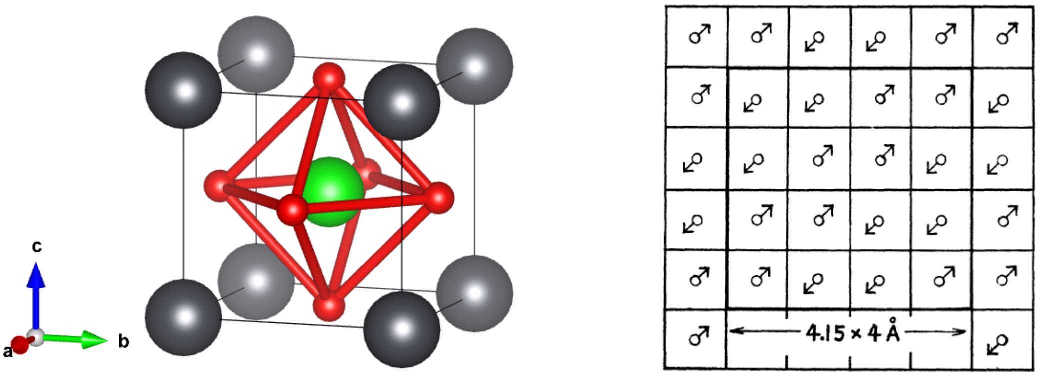

(a) (b)

Figure I.19: (a) Perovskite structure of PbZrO_3 in the cubic paraelectric phase. Grey spheres represent lead atoms, green zirconium and red oxygen. (b) Antiparallel atomic arrangement of PbZrO_3 along the ab-plane in the antiferroelectric phase. Arrows represent the displacements of lead compared to the paraelectric structure. Adapted from [23].

Historically, orthorhombic non-polar $Pbam$ and orthorhombic polar $Pba2$ space groups were the two proposed structures for the room temperature phase of PbZrO_3. Indeed, extra oxygen displacements were seen at the transition [24] or a weak ferroelectric character was measured [25], leading to the hypothesis of a $Pba2$ polar orthorhombic structure. However, the non-polar $Pbam$ phase is now considered to be the ground state for PbZrO_3, confirmed notably by first-principles calculations [26]. With respect to the paraelectric phase, the antiferroelectric phase has a unit cell of 8 formula units with parameters $a = \sqrt{2}a_{cubic}, b = 2\sqrt{2}a_{cubic}, c = 2a_{cubic}$.

Antiparallel displacements of lead atoms

The paraelectric to antiferroelectric phase transition is partly driven by lead displacements along the [110] pseudo-cubic directions, leading to an antiparallel arrangement of lead displacements as shown in Fig. I.19b. Along the ab-direction, there is an "up-down" alternance of electric dipoles of opposite directions, compared to an "up-up-down-down" alternance along the a- or the b-axis.

Anomaly in the dielectric constant

At T_c, the dielectric constant shows a clear anomaly. Contrasting with what was mentioned in the previous section I.2.b, $PbZrO_3$ does display a dielectric constant that peaks at T_c without diverging.

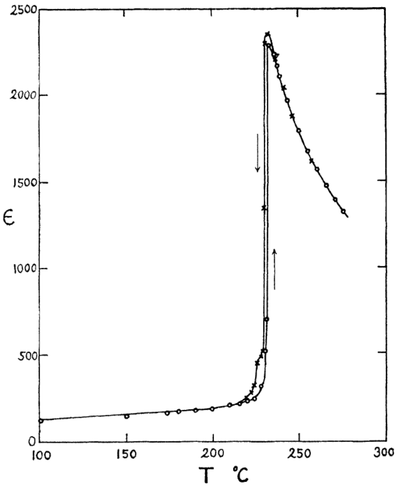

Figure I.20: Dielectric anomaly of $PbZrO_3$. Adapted from [23].

Field-induced phase transition to a polar phase

In pure $PbZrO_3$ ceramics, the breakdown field is too high compared to the critical field to be switched at room temperature. This is why the first realisation of an antiferroelectric switching in Ref. [23] was made at 228 °C, i.e. $\approx$ 5 °C below T_c.

Following this realization, doping has been the favourite way to process $PbZrO_3$-based ceramics that could be switched at ambient conditions. Simultaneously doping with lanthanum and titanium is an efficient way of lowering the energy difference between antiferroelectric and ferroelectric phases, hence lowering the critical field required to induce the polar phase [27]. Other dopants such as tin or niobium are also commonly used to tune the properties of $PbZrO_3$-based ceramics or films.

Thin films have proven to facilitate the antiferroelectric switching of pure $PbZrO_3$, by increasing geometrically the applied field possible while decreasing breakdown fields [28].

Symmetry of the polar phase?

This particular point is of great importance for the complex switching behaviour of $PbZrO_3$ and hence will be discussed in detail in chapter III.

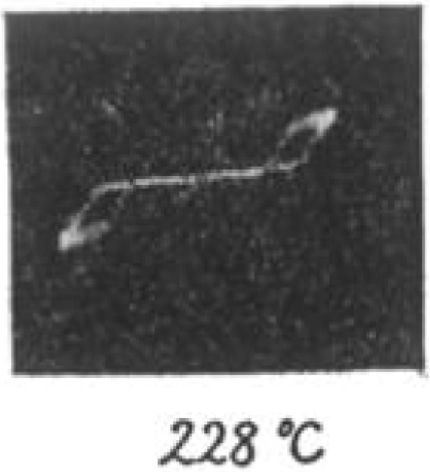

Figure I.21: Field-induced phase transition of $PbZrO_3$ at 228 °C and up to 30 kV cm^{-1}. Adapted from [23].

An intermediate ferroelectric phase?

Several studies [29–32] have reported that $PbZrO_3$ could undergo an antiferroelectric to ferroelectric phase transition on a small range of temperatures below T_c. On Fig. I.22 is represented the thermal expansion coefficient of $PbZrO_3$ with respect to the temperature. The sharp peak corresponds to this intermediate ferroelectric phase. This behaviour is however not reproducible, as it is not seen in the majority of studies on $PbZrO_3$ ceramics, thin films or single crystals.

In reference [33], Liu proposes an explanation for that intermediate ferroelectric phase based on crystallographic orientation. Based on x-ray diffraction and dielectric experiments, it is inferred that this ferroelectric intermediate phase occurs only in $PbZrO_3$ samples with a low number of $[001]_{\mathrm{pseudo-cubic}}$ domains. These domains would normally hinder the $a^-a^-c^0$ octahedra rotations, leading to a very stable antiferroelectric phase. The low amount or the absence of those domains would then explain how a ferroelectric phase could stabilize in a small range below T_c instead of the antferroelectric phase.

I.3.b Other antiferroelectrics

Reviewing antiferrolectric materials is a complicated task, as few materials actually display the three experimental signatures previously mentioned, but also because the term "antiferroelectric" is often used in literature to describe materials that do not display all of these three signatures. We will then list candidate antiferroelectric materials displaying at least one of these experimental signatures.

Lead hafnate $PbHfO_3$ is often considered as the "second model" of antiferroeletric perovskites.

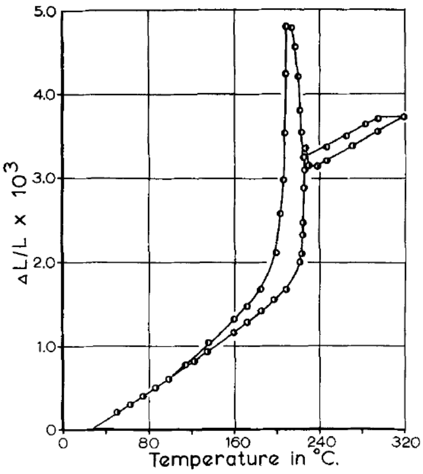

Figure I.22: Temperature-dependency of $PbZrO_3$ thermal expansion coefficient. The peak is linked to the intermediate ferroelectric phase. Adapted from [29]

Indeed, $PbHfO_3$ and $PbZrO_3$ room temperature antiferroelectric and paraelectric phase are of the same symmetry, but $PbHfO_3$ has an even more complex phase diagram as an antiferroelectric to antiferroelectric phase transition happens at 436 K, explaining the two T_c and $E_{\mathrm{AFE}\to\mathrm{FE}}$ in Tab. I.2. For these perovskites, the antiferroelectricity is mostly due to lead ion antiparallel displacements.

Due to the growing interest of lead-free ferroics, niobates, such as $AgNbO_3$ or $NaNbO_3$, have generated a growing interest in the latest years. They display the three characteristic signatures of antiferroelectricity with reasonably low switching fields $E_{\mathrm{AFE}\to\mathrm{FE}}$ but display a complex series of phase transitions, making them difficult to use for certain applications.

Other perovskites or perovskite-like systems also display some signatures of antiferroelectricity. Notably, rare-earth substitution of $BiFeO_3$ has been predicted to force the material in a non-polar orthorhombic structure with Bi antiparallel displacements, similarly to $PbZrO_3$. The only antiferroelectric switching which has been demonstrated is from Ref. [34]. It is however quite incomplete and could still be due to other physical phenomena. One of the original objectives of this PhD was actually to try to engineer a antiferroelectric switching in rare-earth substituted sol-gel $BiFeO_3$, but this was met with no success. Hybrid organic-inorganic perovskites are promising in solar cell applications and some of them also display signatures of antiferroelectricity, notably methylammonium lead halides of formula $CH_3NH_3PbX_3$, X being an halide. A recent theoretical study from Ref. [35] presents clearly defined (and theoretically switchable) electric dipoles formed by tetrahedra in pyroxene-like ABO_3 oxides.

For ultra thin films and due to the recent discovery of ferroelectric phases, ZrO_2-based and

HfO_2-based materials are also extremely promising, even if gew groups have taken a direct interest in their potential antiferroelecric properties. It is also interesting to note that they are CMOS compatible and already broadly used in the semi-conductor industry.

Vanadates such as $DyVO_4$ or $TbVO_4$ display an antiparallel array of dipoles formed by VO_4 tetrahedra. The potential antiferroelctric phase transition in these materials is driven by the Jahn-Teller effect creating these dipoles.

Hydrogen-bonded materials are an important family of ferroelectrics which also has a large amount of good antiferroelectric candidates. For instance, squaric acid $C_4O_4H_2$ displays a remarkable array of oppositely polarised sublattices. In ref. [22], the authors have also seen the dielectric anomaly at the antiferroelectric to paraelectric phase transition temperature and observed a antiferroelectric switching under field with very little hysteresis.

This summarises the main categories of antiferroelectric materials.

Formula	DA	APD	AS	T_c	$E_{\mathrm{AFE}\rightarrow\mathrm{FE}}$	Ref.
Lead-based perovskites						
$PbZrO_3$	✓	✓	✓	505 K	300-550 kV cm^{-1}	[23, 36]
$PbHfO_3$ (2 AFE phases?)	✓	✓	✓	436/488 K	300/175 kV cm^{-1}	[37–39]
Niobates						
$AgNbO_3$	✓	✓	✓	613 K	110-150 kV cm^{-1}	[40, 41]
$NaNbO_3$	✓	✓	(✓)	848 K	90 kV cm^{-1}	[42–44]
Other perovskites and ABX_3 structures						
$BiFeO_3$-based	-	✓	(✓)	-	≈500 kV cm^{-1}	[34, 45]
Hybrid organic–inorganic perovskites	✓	✓	-	120-180 K	-	[46, 47]
WO_3	✓	✓	-	-	-	[48, 49]
$(K/Cs/Rb)VO_3$	-	✓	(✓)	-	Theory: 40 MV cm^{-1}	[35]
$Pb(Lu_{0.5}Nb_{0.5})O_3$	✓	✓	✓	513 K	170 MV cm^{-1}	[50]
High-k dielectrics						
ZrO_2 & HfO_2	-	-	✓	-	≈ 2 MV cm^{-1}	[51, 52]
Vanadates						
$DyVO_4$	✓	✓	-	15 K	-	[53]
$TbVO_4$	✓	✓	-	33 K	-	[53]
Hydrogen-bonded materials						
$C_4O_4H_2$	✓	✓	✓	373 K	125 kV cm^{-1}	[22, 54]
$NH_4H_2PO_4$	✓	✓		148 K		[54]
$NH_4H_2AsO_4/NH_4D_2AsO_4$	-	(✓)	-	216/304 K		[55, 56]
$CsH_3(SeO_3)_2$	✓	-	(✓)	145 K	40-60 kV cm^{-1}	[57]
$Ag_2H_3IO_6$	✓	✓	-	240 K		[58, 59]
$(NH_4)_2H_3IO_6$	✓	✓	-	254 K		[59]
$Cu(HCOO)_2{\cdot}4H_2O$	✓	✓	✓	234 K	15-20 kV cm^{-1}	[60, 61]
2-trifluoromethylnaphthimidazole	-	✓	✓	410 K	30-40 kV cm^{-1}	[62]
Others crystals						
KCN	-	✓	-	83 K		[63–65]
NaCN	✓	-	-	172 K		[64]
$Cs_2Nb_4O_{11}$	(✓)	✓	-	438 K		[66]
$GaNb_4S_8$	✓	✓	(✓)	31 K		[67]
$K_3Nb_3B_2O_{12}$	✓	✓	✓	376/676 K	20 kV cm^{-1}	[68]
$Cu_3Bi_2(SeO_3)_2OCl$	✓	✓	-	115 K	-	[69, 70]
Liquid crystals						

Table I.2: Antiferroelectric candidates. DA stands for dielectric anomaly, APD stands for antiparallel ion displacements, AS stands for antiferroelectric switching.

I.4 Applications of interest for antiferroelectrics

Current interest on antiferroelectrics is driven by both fundamental interests and application potential. In that part, some of the most-discussed applications of antiferroelectrics are highlighted.

I.4.a Energy storage

Energy storage is probably the most promising application possible for antiferroelectrics and is often the goal of many of the most applicative projects around antiferroelectricity. Indeed the need for supercapacitors is only increasing with the number of devices with integrated battery each individual possesses.

It is possible to store electrical energy in any dielectric material, as the energy spent into changing the polarisation of the material by applying an electric field can then be recovered via a discharge of the material.

The stored W_{stored} and recoverable energy density $W_{\text{recoverable}}$ are directly linked to the shape of the polarisation curve $P(E)$ of the material: the higher the polarisation, the more you can store energy, as formalised in Eq. (I.11). This need of a large polarisation explains why most of the research on energy storage in dielectrics revolves around ferro- and antiferroelectrics rather than linear dielectrics.

$$\left.\begin{array}{rl} W_{\text{stored}} = & \int_0^{P_{max}} EdP \\ W_{\text{recoverable}} = - & \int_{P_{max}}^{P_0} EdP \end{array}\right\} \Longrightarrow \text{Efficiency } \eta = \frac{W_{\text{recoverable}}}{W_{\text{stored}}} \tag{I.11}$$

However, due to the low coercive fields, ferroelectrics can usually store a low energy density. Also, the hysteresis in the polarisation curves induces an even lower recoverable energy density hence a low storage efficiency η.

In antiferroelectrics, because of the shape of the double hysteresis loop and of the high critical field, the stored energy density is theoretically much higher than in ferroelectrics. Though, the hysteresis also leads to losses and decreases the storage efficiency. Applied research focused on antiferroelectric energy storage then focuses largely on increasing the critical field and polarisation, decreasing the hysteresis and studying the fatigue and reliability of antiferroelectrics.

The ideal shape of $P(E)$ loops for energy storage is then a slanted loop with a high coercive field which are can be reliably obtained from antiferroelectrics.

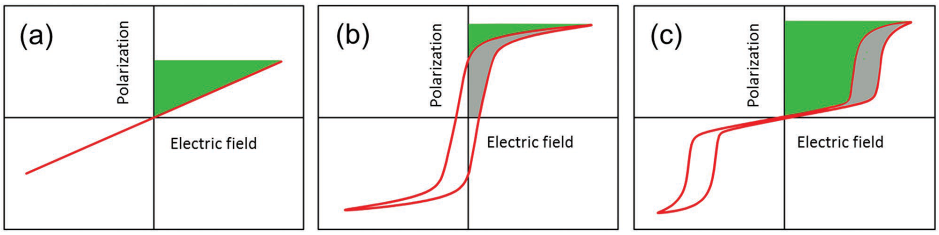

Figure I.23: Principle of energy storage in (a) linear dielectrics, (b) ferroelectrics and (c) antiferroelectrics. The recoverable energy density $W_{\mathrm{recoverable}}$ is indicated in green while losses (i.e. $W_{\mathrm{stored}} - W_{\mathrm{recoverable}}$) are in grey. Adapted from [71].

I.4.b Electrocaloric effect

A massive amount of energy is now dedicated to refrigeration around the world, and should only increase with global warming. Research on efficient and effective new ways of cooling is hence booming.

Antiferroelectric to ferroelectric phase transitions have a particular place in electrocaloric cooling as they lead to cooling instead of heating for a ferroelectric to paraelectric phase transition. Indeed, in dielectrics near a phase transition, the application of an electric field changes drastically the entropy of the system, as formalised in Eq. I.12, which then releases or absorbs heat after field removal, Eq. I.13. The higher the polarisation change and the sharper the transition, the higher the temperature change ΔT will be. In seminal reference [72], a ΔT of up to 12 K can be reached with a thin film of antiferroelectric PZT, see Fig. I.24. Recently, a prototype has been engineered to harvest this effect and cool down a fluid up to 20 K [73].

$$\text{Isothermal entropy change: } \Delta S = + \int_{E_1}^{E_2} \left(\frac{\partial P}{\partial T}\right)_E dE \tag{I.12}$$

$$\text{Adiabatic temperature change: } \Delta T = - \frac{T}{m\ C_p} \int_{E_1}^{E_2} \left(\frac{\partial P}{\partial T}\right)_E dE \tag{I.13}$$

I.4.c Antiferroelectric tunnel junctions for nanoelectronics

In nanoelectronics, tunnel junctions are used as part of LEDs or memristors in artificial synapses. The concept of antiferroelectric tunnel junction has been proposed [74] and realised in a few studies [75].

A very thin layer dielectric between two magnetic electrodes will let electrons pass through tunneling depending on the energy barrier at the interfaces. Ferroelectric layers can be used as the dielectric layer. Indeed, flipping the polarisation inside the dielectric layer will have a strong

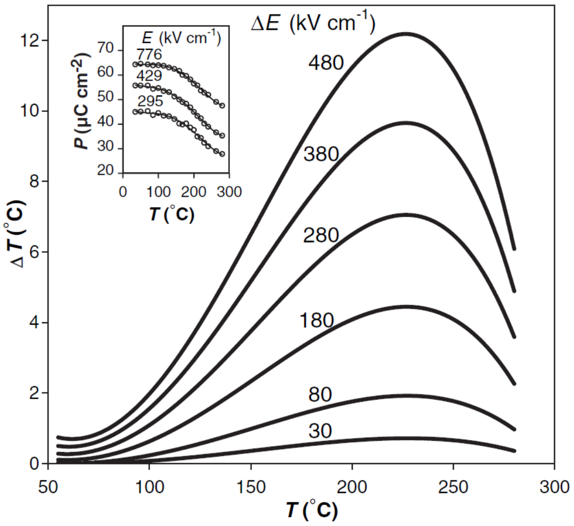

Figure I.24: Temperature span $\varDelta T$ of up to 12 K reached in an antiferroelectric PZT thin film. Adapted from [72].

impact on the height of the dielectric barrier between the two electrodes. However, the remanent polarisation will always let electrons tunnel through the layer even when the polarisation is such that the electronic barrier is the highest.

Using an antiferroelectric can solve that issue: inducing the polar phase will drastically lower the energy barrier while without any applied electric field, the absence of polarisation will lead to an extremely high energy barrier. The antiferroelectric to ferroelectric phase transition is then analogous to a switch. In reference [75], the ratio of resistance between the ON and OFF states reached up to 10^7.

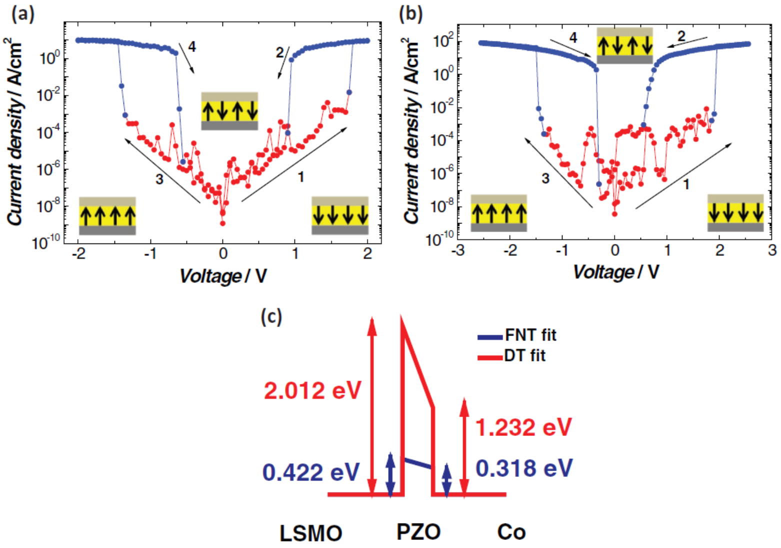

Figure I.25: Current density passing through the junction for (a) an 11 unit-cell and (b) a 16 unit-cell thick $PbZrO_3$ layer. (c) Energy barrier difference between the antiferroelectric phase (in red) and the polar phase (in blue). Adapted from [75].

I.5 Open questions and objectives

Issues around the definition of antiferroelectricity

Ferroelectric phase transitions break the inversion symmetry of the crystal but antiferroelectric phase transitions do not have such a criterion. This lack of symmetry-based definition is one of the core of the issues around the definition of antiferroelectricity. Several authors have then tried to define symmetry-based criteria for antiferroelectricity [21, 59, 76] but none of these propositions are widely accepted in the antiferroelectric community.

Furthermore, Kittel's model of antiferroelectricity has been useful to start the discussion around antiferroelectricity but, to the best of our knowledge, no material has ever been considered to be a Kittel-like antiferroelectric. For instance, current model perovskite lead zirconate $PbZrO_3$ is not a perfect Kittel antiferroelectric. Indeed, on top of the antiparallel lead displacements, another distortion leading to the $Pbam$ structure of $PbZrO_3$ is a rotation of the oxygen octahedron around the [110] pseudo-cubic direction. The potential intermediate ferroelectric phase, the fact that the field-induced phase transition also has a ferroelastic character and the debates around the symmetry of the polar phase only accentuate the complexity of this phase transition.

On a side note, all of the known antiferroelectrics display an order-disorder or mixed character of their phase transition. Indeed, to the best of our knowledge, no purely displacive antiferroelectric material has been discovered and characterised.

It is then of high-interest to find model antiferroelectric materials. For instance, materials that display a displacive character or are a realisation of a model Kittel-antiferroelectric. Another relevant point would also be to complete the list of materials with different mechanisms leading to antiferroelectricity, such as Jahn-Teller effect, geometrical effects or hydrogen-bond reorganisation.

Issues around the antiferroelectric switching

The electrical field-induced antiferroelectric switching of antiferroelectrics is the main characteristic used in the typical applications proposed, such as energy storage. However, "double hysteresis loops" is not the only criterion for antiferroelectricity.

For instance, "double hysteresis loops" can be measured in materials that are not antiferroelectrics, such as ferroelectric $BaTiO_3$ [77]. This can be the result of different physical mechanisms. For instance, in $HoMnO_3$ [78], charged defects pin neighbouring domains in opposite direction, leading to polarisation curves with double hysteresis. A similar effect could be seen in ferroelectrics thin films that are clamped to a substrate. For instance, $PbTiO_3$ can split in polar domains of opposite polarisation, see Ref. [79–81]. For a ferroelectric above but very close to T_c, applying an electric field can induce a paraelectric to ferroelectric phase transition [82] which also leads to "antiferroelectric-like" polarisation curves. This behaviour can quite simply be explained by Landau theory. Acceptor-doped oxide ferroelectrics contain more oxygen vacancies which, along with the dopant, can create randomly oriented electric dipoles and cause backswitching of domains during field application [83]. Also, this "double loop" might not be seen in materials that are considered as antiferroelectrics. For instance, this can be simply due a breakdown field lower than the critical field $E_{\mathrm{AFE}\to\mathrm{FE}}$.

Objectives of this thesis

This thesis project was organised around two major axes.

Firstly, we studied well-established antiferroelectric materials to evaluate their applicative potential. To do so, we synthesised antiferroelectric materials and studied the mechanism and properties of their antiferroelectric switching. Thin films of $PbZrO_3$ were chosen. Indeed, $PbZrO_3$ is a well-established antiferroelectric material which, as a thin film, still offers a large potential for exploration of different substrates, different switching geometries and physical properties to be monitored during switching.

Secondly, we looked for novel antiferroelectrics, in hope of finding model materials. To that end, several compounds have been considered and their phase transitions investigated during the course of this thesis, but the work was finally focused on francisite $Cu_3Bi(SeO_3)_2O_2Cl$ for its original soft-mode dynamics.

Chapter II

Experimental methods

In that chapter, we will present the main experimental methods relevant to the characterisation of antiferroelectric materials and phase transitions that will be used in the two chapters of results, later on.

The first chapter of results will cover synthesis of sol-gel $PbZrO_3$ thin films as well as their structural and electrical characterisation. We will hence introduce our synthesis method of choice, chemical solution deposition, before discussing characterisation of thin films structure, orientation and strain thanks to x-ray diffraction-based methods. The third section will be about electrical characterisation of antiferroelectric films.

The second chapter of results will deal with the fundamental spectroscopic study of an antiferroelectric phase transition in Francisite $Cu_3Bi(SeO_3)_2O_2Cl$. Raman spectroscopy will therefore be discussed, before introducing the study of phonon through synchrotron-based inelastic x-ray scattering and thermal diffuse scattering.

II.1 Synthesis of thin films by Chemical Solution Deposition (CSD)

In that section, we will present a chemical sol-gel synthesis method: chemical solution deposition (CSD). Many common ferroelectric oxides such as lead zirconate $PbZrO_3$ [84], lead titanate $PbTiO_3$ [85] and PZT solid solutions in between or more recently bismuth ferrite $BiFeO_3$ [86], hafnia HfO_2 [87] or zirconia ZrO_2 have been successfully synthesised through CSD.

II.1.a Overview of the deposition process

Before starting the actual deposition, we first need to prepare the solution used during processing. Metallic precursors (noted MX), such as metal acetates or nitrates, are dissolved into an organic solvent (noted R), such as 2-methoxyethanol, and then form metal-organic complexes (noted $M(OR'_n)$), for instance alcoxides.

This solution is then deposited on the substrate through dip-coating, spraying, inkjet printing or spin-coating, the chosen method in that work.

A first drying step ensures the evaporation of the organic solvent, i.e the chosen temperature must then be higher than the solvent boiling point. At that step, the film is a gel. A second step at higher temperatures breaks down the metal-organic compounds to pyrolyse the film. The last step is the annealing at even higher temperatures to crystallise the film in the wanted phase.

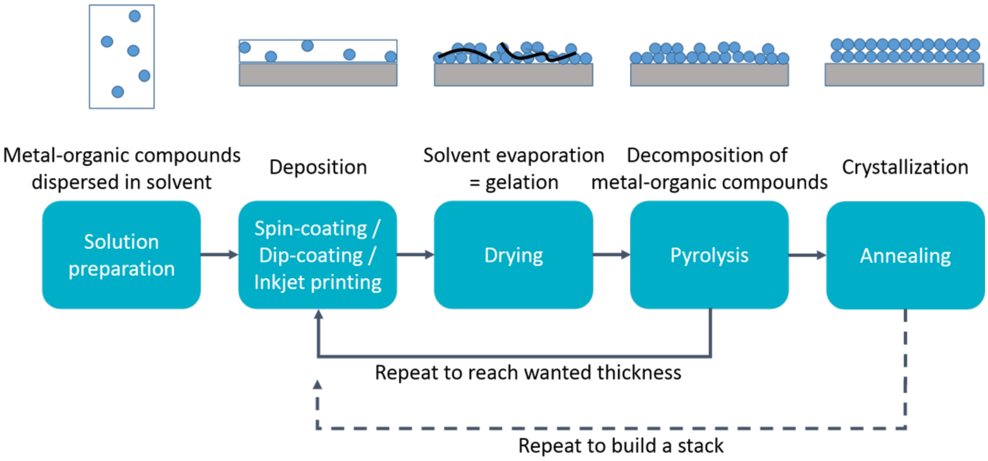

Figure II.1: Schematic principle of Chemical Solution Deposition.

Repeated coating, drying and pyrolysis before annealing allow the stacking of layers to increase film thickness. The minimum order of magnitude for CSD films is around 10 nm for a single layer while the maximum film thickness is usually a few micrometers by repeated stacking and annealing.

Solution stoichiometry and the choice of the annealing temperature and its duration have proven to be key in crystallising the material in the right phase. Indeed, other phases than the desired one can be more stable at different annealing temperatures or composition, as shown in Fig. II.2 for the PbO-TiO$_2$ system. The atmosphere (oxidising or reducing) during annealing or reannealing has also shown to have an effect on film quality, such as the quantity of oxygen vacancies [88].

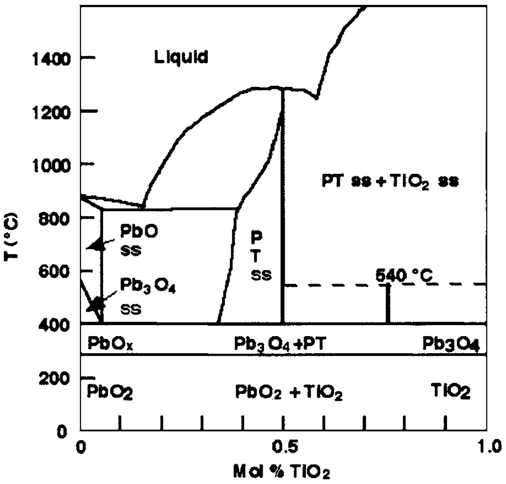

Figure II.2: Stability of the different phases of the PbO-TiO$_2$ system with respect to molar portion of TiO$_2$ and temperature. Adapted from [89]. The label "PT" indicates the stability of the perovskite PbTiO$_3$ phase.

II.1.b Solution processing

Solution precursors are usually chosen due to their chemical and physical properties: purity, water content, ease of use, etc. The solvent should have a high purity, a good solubility for the chosen precursors and a boiling point higher than water.

Moisture level is an important factor in the preparation of solutions, as it decreases drastically the shelf life of the prepared solutions due to a quicker precipitation, altering the stoichiometry of the films. To remove a maximum of water, anhydride precursors are often used, if possible, or standard precursors are freeze-dried prior to use. The solution can also be chemically dried through hydrolysis by adding acid anhydride, such as acetic anhydride, to the solution in a stoichiometric ratio with respect to the water.

The higher the concentration of metal-organic compounds in the solution, the thicker the crystallised layer will be. For instance, with our standard in-house $0.3\,\mathrm{mol\,L^{-1}}$ PZT solution, each crystallised layer will be around 50 nm.

For certain elements such as lead Pb or bismuth Bi, it is important to add a stoichiometric excess of these precursors to compensate the non-negligible loss during crystallisation. A typical lead excess in PZT solutions is around 30 % and around 20 & for $PbZrO_3$ solutions.

Ref. [85] shows an example of solution processing for lead lanthanum zirconate titanate PLZT. The chosen precursors are lead and lanthanum acetates dissolved into 2-methoxyethanol then boiled to remove water. Solutions of zirconium and titanium alkoxides are then directly mixed into the resulting solution, before further boiling to purify the solution, increase the concentration of alkoxides and remove excess water. Dilution is then realized to reach the exact concentration wanted. The whole process is represented on Fig. II.3.

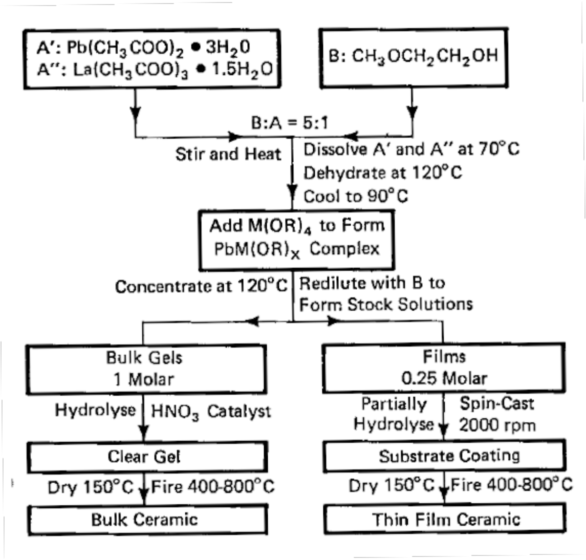

Figure II.3: Example of solution preparation (and deposition) for $PbLa_{1-x}(Zr_yTi_{1-y})_xO_3$ (PLZT) sol-gel ceramics and thin films. Adapted from [85].

II.1.c Properties of CSD and CSD-processed thin films

First, going through a gel state can drastically lower the energy needed to crystallise the oxide in its ferroelectric phase.For instance, PZT ceramics are often sintered at temperatures above 1000 °C while a standard CSD process has a typical annealing temperature of 700 °C or lower.

The ability to cover large areas and the lower costs of precursors, in-house PZT solutions are around 300 € by liter, compared to physical methods of deposition make of CSD a good thin-film synthesis technique for application purposes.

CSD allows to synthesise films on a wide range of substrates. For oxides, silicon-based substrates are usually used, often coated with a metal to be used as a bottom electrode. Glass substrates are also often used to synthesis films for electro-optical or photovoltaic applications. Different oxides such as lanthanum nickelate $LaNiO_3$ [90] or strontium titanate $SrTiO_3$ [91] amongst others can also be used as well to take advantage of the orientation. Nickel or aluminium foils have also been used, mostly for piezoelectric applications because of substrate flexibility. However, due to the relative high temperatures, usually around 600 to 700 °C, required for the annealing of most ferroelectric oxides processed by CSD, the choice of substrates is limited to materials able to sustain these temperatures. The use of polymer or plastic-based substrates is then often impossible for standard CSD processes. It is however possible to grow materials on polymers by using photoannealing or by doing wafer-bonding, for instance.

In CSD, it is possible to obtain oriented samples. Film orientation is due to the influence of the substrate or seed layer on which the films are grown.

Experimental setup

A glove-box is used to prepare the solution in a controlled moisture-free and neutral atomosphere. The processing of the films themselves happen under a fumehood in an ISO5 clean room. Spin-coating is performed with a SPS Spin 150. Hot plates are used to dry and pyrolise the films. Our rapid thermal annealing furnace is the Annealsys AS-Master, normally used for RTCVD processes.

Properties of CSD films

- Chemical synthesis method
- Polycrystalline samples
- Engineering possible of film orientation
- Thickness from $\approx 10\,\mathrm{nm}$ to $\approx 1\,\mu\mathrm{m}$
- Large deposition area
- Low-cost

II.2 X-ray diffraction

II.2.a Basics of X-ray diffraction

Crystals can be considered as planes of ions separated by a few angströms. As such, when x-rays of a wavelength λ of the same order of magnitude are sent to the crystal with an angle θ, these rays will be diffracted with the same angle θ (see Fig. II.4) and interfere constructively.

The atomic planes forming the crystal can be labelled with the integer indices (hkl), called Miller indices. (hkl) planes are orthogonal to the vector defined by $\vec{G}_{hkl} = h\vec{a}_1^* + k\vec{a}_2^* + l\vec{a}_3^*$, where vectors $\vec{a}_i^*$ are the basis in the reciprocal space.

From there, the distance d_{hkl} between two adjacent (hkl) planes is:

$$d_{hkl} = \frac{2\pi}{||\vec{G}_{hkl}||}$$

The matching angle is then written θ_{hkl} and Bragg's condition can then be expressed as:

$$2d_{hkl}\sin\theta_{hkl} = \lambda \Longleftrightarrow 2\sin\theta_{hkl} = \frac{\lambda}{2\pi}||\vec{G}_{hkl}||$$

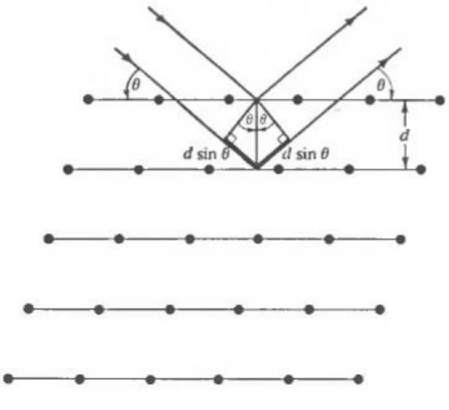

Figure II.4: Principle of Bragg reflection. Adapted from [92].

When simultaneously-moving x-ray tube and detector are placed at angle θ with respect to the tested sample, a peak will appear in the recorded pattern each time θ matches λ according to Bragg's law.

Experimentally, finding the Miller indices (hkl) associated to each diffraction peak and calculating their associated distance d_{hkl} will allow us to find the geometry and lattice parameters of the studied unit cell.

II.2.b Estimation of film orientation: the Lotgering factor

The Lotgering factor [93] is a way of estimating the preferential orientation of the tested samples with respect to a reference plane (mnp). A randomly oriented reference sample is needed to compare the ratio of intensities coming from the selected plane with the intensity coming from all planes, in both reference and tested sample. The Lotgering factor f_{mnp} can take any value between 0, meaning that the tested sample is ramdomly oriented along (mnp), and 1, meaning that the tested sample is fully oriented along (mnp). Hence the factor is written as follows:

$$f_{mnp} = \frac{P_{mnp} - P_0}{1 - P_0} \quad \text{with} \quad P_{mnp} = \frac{\sum I_{mnp}}{\sum I_{hkl}} \quad \text{and} \quad P_0 = \frac{\sum I^0_{mnp}}{\sum I^0_{hkl}}$$

$\sum I_{mnp}$ is the sum of the intensity of the (mnp) reflections of the textured sample while $\sum I_{hkl}$ is the sum of all the (hkl) reflections of the textured sample.

Similarly, $\sum I^0_{mnp}$ is the sum of the intensity of the (mnp) reflections of a randomly oriented reference sample while $\sum I^0_{hkl}$ is the sum of all the (hkl) reflections of this reference powder.

II.2.c Pole figures

Pole figures can be used to study the texture of a sample. We will here only discuss the case of pole figures applied to measure film orientation.

The sample is placed in a diffractometer as for a standard $\theta - 2\theta$ scan. Source and detector are placed at a fixed diffraction angle 2θ, with respect to the normal to the sample surface, so that the maximum of intensity of the chosen reflection is visible. This reflection is called the pole.

The measurement consist on seeing the variation of intensity of the pole while tilting the sample to an angle Ψ and rotating it around the normal with an angle Φ, these angles are shown on Fig. II.5.

If the film is oriented along the measured pole, the intensity will be maximal at Ψ=0. However, if it is not oriented along the pole, the intensity will only be maximal at a certain Ψ_0 angle. The intensity variation of this peak while rotating of Φ around the normal will then depend on the in-plane film texture. If no intensity variation is seen, then the film is isotropically oriented in-plane, otherwise there is a preferential in-plane orientation.

II.2.d Estimation of film strain: sin$^2\Psi$ method

Thermal expansion coefficient (TEC) mismatch between the substrate and the material induces stress and strain in polycrystalline films. In sol-gel films, layers of amorphous matter are deposited

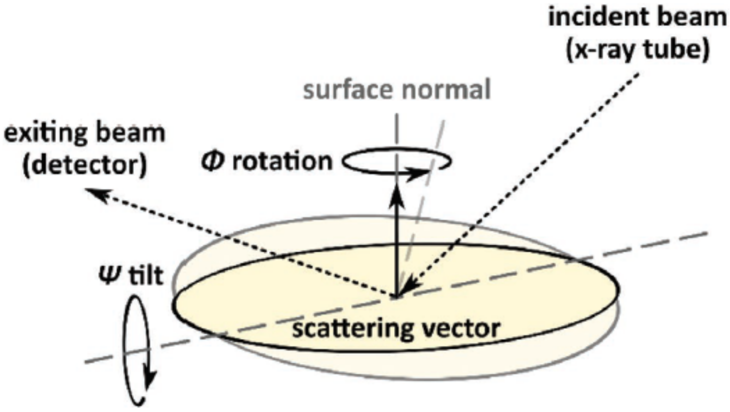

Figure II.5: Sketch of the diffraction geometry used to measure pole figures and estimate the strain state of our films. Adapted from [87].

on the substrate before annealing then, during crystallisation, the film nucleates and densifies before contracting during cooling, creating a strained system. We note the strain ϵ_{ij} with respect to the axes i and j of the sample $(1, 2, 3 = x, y, z)$. For instance, ϵ_{33} is the out-of-plane strain while ϵ_{11} or ϵ_{22} are in-plane.

In reference [87], a way of estimating the strain state of films from x-ray diffraction patterns is proposed by the authors. The inter-distance between two (hkl) planes was previously written d_{hkl}. In that section, a specific d_{hkl} is chosen and the inter-distance will then be rewritten as: $d_{\Phi,\Psi}$ to highlight the dependency of this value with respect to the in-plane rotation angle Φ around the surface normal and the tilt angle Ψ between the sample surface and the scattering vector, see Fig. II.5. The inter-distance d_0 for an unstrained reference sample will also be used. From these two quantities, the strain of the film can be written as:

$$\epsilon_{\Phi,\Psi} = \frac{d_{\Phi,\Psi} - d_0}{d_0}$$

In the case of sol-gel polycrystalline films, there is an isotropy of the material in-plane so the in-plane stains are equal $\epsilon_{11} = \epsilon_{22}$. Assuming that the shear strain is negligible in those films, we can rewrite it as a function of in-plane ϵ_{11} and out-of-plane strains ϵ_{33}:

$$\epsilon_{\Phi,\Psi} = \frac{d_{\Phi,\Psi} - d_0}{d_0} = (\epsilon_{11} - \epsilon_{33}) \sin^2 \Psi + \epsilon_{33}$$

Let us assume that the out-of-plane strain is proportional to the in-plane strain, i.e. $\epsilon_{33} = \alpha \epsilon_{11}$. Then, this coefficient α is given by [87] as being a function of Poisson coefficient ν: $\alpha = \frac{-2\nu}{1-\nu}$.

That allows us to simplify the expression of $d_{\Phi,\Psi}$ to:

$$d_{\Phi,\Psi} = (1-\alpha)d_0\epsilon_{11}\sin^2\Psi + (1+\alpha\epsilon_{11})d_0$$

To summarise: measuring the peak position of a chosen (hkl) reflection at different Ψ angles will allow us to plot $d_{\Phi,\Psi}$ as a function of $\sin^2\Psi$. Fitting $d_{\Phi,\Psi}$ with a linear function will allow us to extract the slope a and intersect b to estimate both d_0 and in-plane strain ϵ_{11} of the films. On top of that, knowing the Poisson coefficient of the material will give us the out-of-plane strain ϵ_{33} from ϵ_{11}.

Experimental setup

All of the XRD measurements in this thesis using the methods presented previously used a Bruker D8 Discover diffractometer with a 5-axis cradle and a copper anode ($\lambda_{\mathrm{Cu}(K_\alpha)} = 1.541\,84$ Å). In every method, $\theta - 2\theta$ scans were preferred above grazing incidence to keep quantitative intensity ratios between reflections, in order to easily access the film texture.

II.3 Dielectric characterization of thin films

II.3.a Measurement of relative permittivity ε

With increasing temperature, antiferroelectrics undergo a phase transition to a paraelectric phase at the Curie temperature T_c. This transition is accompanied by an anomaly at T_c in the relative permittivity ε. Measuring ε can then help us estimating T_c and to do so, it is usual to measure the capacitance C of the tested material.

Let us consider an insulator between two metallic plates. The capacitance of the tested material is $C = \frac{\partial Q}{\partial V}$ where V is the voltage applied on material and Q is the charge at the surface of the capacitor. $Q = SD$, where S is the area of the material surface and D the displacement. For dielectric materials, we also have $D = \varepsilon_0 E + P = \varepsilon_0 \varepsilon E$. Let us now apply an ac electric field $E = (V + V_0 \sin(\omega t))/a$, where a is the distance between the two electrodes and ω the frequency of the electric field. For high-frequencies, the electric field is in average $E = V/a$. The capacitance can be hence rewritten as:

$$C = \frac{S}{a}\frac{\partial D}{\partial E} = \frac{S}{a}\varepsilon_0\varepsilon \Longleftrightarrow \varepsilon = \frac{a}{S\varepsilon_0}C$$

The permittivity ε in the frequency space can be divided between a real ε' and an imaginary part ε'', which represents the dielectric losses. The usual physical quantity measuring these losses is then the loss tangent: $\tan\delta = \frac{\varepsilon''}{\varepsilon'}$.

II.3.b Measurement of polarisation curves $P(E)$ of (anti)ferroelectrics

Polar switching is one of the signature of antiferroelectricity, we then need to be able to measure the material polarisation P as a function of the applied electric field E.

Ideal case of an (anti)ferroelectric without leakage

In the limit of negligible leakage currents, the measured polarisation P is linked to the current i and to the electrode surface S by the relation

$$\frac{dP(t)}{dt} = S\ i(t)$$

Then with an oscillating electric field, we can then measure the induced polarisation ΔP through the following

$$\Delta P = P(\Delta t) - P(0) = S \int_0^{\Delta t} i(t)\ dt$$

From that relation, we can see that only changes in the polarisation ΔP can be measured by applying an oscillating electric field, and never the absolute polarisation of the material P [9, 94].

Sawyer-Tower setup

Historically, polarisation curves $P(E)$ were measured via a Sawyer-Tower setup. A material of known capacitance C_0 is placed in series with the studied dielectric material and an oscillating voltage V_{tot} is applied to the whole capacitor chain. Measuring the voltage V_0 applied to the reference capacitance C_0 will give the charge Q_0 accumulated on this reference capacitor. Q_0 is equal to the charge Q accumulated on the tested material, as they are connected in series and considered ideal capacitors, see Ref. [95].

It is important to note that the chosen capacitance C_0 is much greater than the capacitance C of the dielectric, so that the global voltage V_{tot} is approximately equal to the voltage applied on dielectric V.

Now to obtain the polarisation P of the dielectric: as previously stated, the displacement D is linked to the charge Q and the electrodes surface S by $D = \frac{Q}{S}$. In particular for dielectrics, $D = \varepsilon_0 E + P$. For ferroelectrics and antiferroelectrics, the polarisation P induced by the application of an electric field is much larger that $\varepsilon_0 E$, so that:

$$P \approx D \approx \frac{Q}{S} \approx \frac{C_0 V_0}{S}$$

Polarisation curves $P(E)$ can then be plotted by measuring the voltage on the reference capacitance V_0 as a function of the applied global voltage V.

The Sawyer-Tower method is however not suitable for very small capacitors as the capacitance coming from the cables (or other parasitic capacitances) is in parallel to the reference capacitor and then can have a non-negligible contribution in the measured total capacitance, see Ref. [**aixacct manual**]. Moreover, the condition $C_0 \gg C$ necessary to minimise the voltage V_0 (so that $V_{tot} \approx V$) also decreases the measurement accuracy of V_0 (low-voltage measurement), and hence the accuracy of the measured polarisation P. Measuring a $P(E)$ curves with a Sawyer-Tower setup can also fatigue quickly the tested samples due to a relatively long measurement time (a few seconds), see Ref. [95].

Virtual-ground feedback method

This method is the one used in our aixACCT Thin Film analyzer 2000 and has been designed to circumvent the cons of the Sawyer-Tower setup.

An operational amplifier is used with one input coming from the ground level and another one coming from a current to voltage converter connected to the sample. On the latter is connected a feedback loop from the output with a resistance. The voltage is measured as the difference between the output channel and the ground.

In that geometry, the voltage difference between both inputs of the amplifier is quasi-null, order of magnitude of a few micronvolts, meaning that the sample is on a "virtual ground", i.e. insulated from the back voltage. This null input potential also means that any parasitic capacitance, coming from cables or others, has a pretty much negligible contribution on the measured capacitance. Finally, our aixACCT setup uses a train of triangular voltage pulses to probe the sample for a much shorter amount of time than on a Sawyer-Tower setup.

II.3.c Relevant physical quantities for antiferroelectrics

In that section, we will discuss the physical quantities relevant for the electric study of antiferroelectrics. To illustrate this discussion, Fig. II.6 can be used as reference.

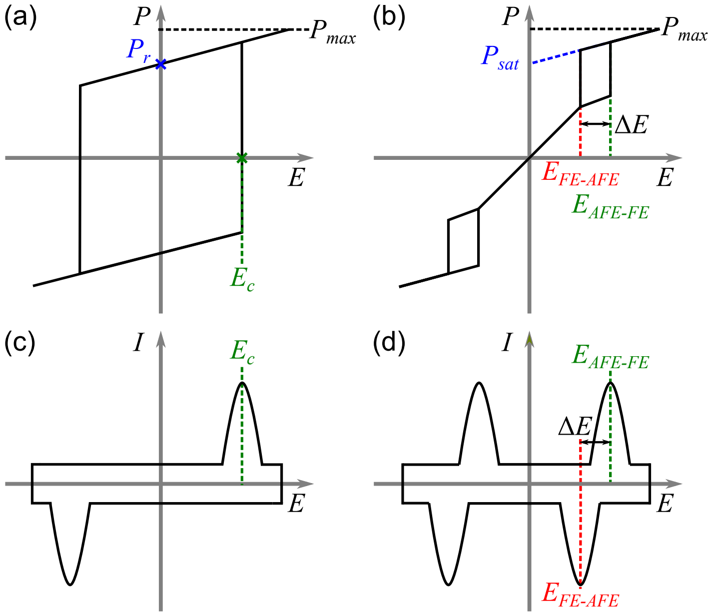

Figure II.6: Schematic polarisation $P(E)$ curves of a (a) ferroelectric and an (b) antiferroelectric material. Their associated characteristic current $I(E)$ curves are respectively drawn on (c) and (d).

Definition of the critical fields $E_{\mathrm{AFE}\to\mathrm{FE}}$ and $E_{\mathrm{FE}\to\mathrm{AFE}}$:

In ferroelectrics, defining the coercive field E_c is quite an easy task. Indeed, when measuring a $P(E)$ curve, E_c is the field value for which the polarisation is zero. This also matches with the position of the two current peaks visible at positive and negative bias in the current curves $I(E)$ (or $I(E)$).

However, in antiferroelectrics, the polarisation is zero when the field is also zero so this definition cannot be applied to AFE. Also, four switching peaks are present: switching between AFE and FE phase and between FE and AFE phase for both positive and negative applied fields.

In this work we chose to note $E_{\mathrm{AFE}\to\mathrm{FE}}$ (E_f in IEEE standards) as the critical field necessary to switch the material from its AFE phase to its polar FE phase. Then, $E_{\mathrm{FE}\to\mathrm{AFE}}$ (E_a in IEEE standards) is the critical field under which the material in its FE phase goes back to the AFE phase. Measuring these quantities is then fitting the position of the positive current switching peak (at positive or negative bias) for $E_{\mathrm{AFE}\to\mathrm{FE}}$ or the position of the positive current switching peak (at positive or negative bias) for $E_{\mathrm{FE}\to\mathrm{AFE}}$.

Other authors use a notation similar to ferroelectrics E_c that is then the averaged value of our $E_{\mathrm{AFE}\to\mathrm{FE}}$ and $E_{\mathrm{FE}\to\mathrm{AFE}}$ quantities. However, reporting only this value in literature is a problem as many doublets ($E_{\mathrm{AFE}\to\mathrm{FE}}$, $E_{\mathrm{FE}\to\mathrm{AFE}}$) could have the same average E_c without being identical. This is also the reason why some authors report also a value ΔE which is the difference of $E_{\mathrm{FE}\to\mathrm{AFE}}$ and $E_{\mathrm{AFE}\to\mathrm{FE}}$. This value has the advantage of directly indicating the width of the hysteresis, which is a particularly important parameter in some applications such as energy storage where ΔT is directly linked to the energy that will not be recovered when stocked into an antiferroelectric capacitor.

Definition of the saturation polarisation P_s:

In ferroelectrics, the remnant polarisation P_r is a key parameter. It is defined as the polarisation measured at zero applied electric field.

However, in an AFE, this value is zero and then the remnant polarisation concept does not make sense.

We however can define a maximum polarisation $P_{\max}$ or a saturation polarisation P_s. $P_{\max}$ is usually simply the maximum polarisation reached by the AFE under an electric field. However, for thin films or ceramics, this value can always be increased by applying stronger electric fields, until the material breaks down or the electrodes short.

For this reason, we prefer to report P_s , which is the linear interpolation of $P_{\max}$ at zero electric field. This definition is however quite arbitrary as the actual polarisation of the material will always overshoot P_s, but this value is however less dependent of the applied electric field than $P_{\max}$.

II.3.d Electric field correction in the case of interdigitated electrodes on films

For interdigitated electrodes (IDE) deposited on a thin film, the electric field E cannot be simply calculated from the voltage V and the gap a between electrodes. Indeed, contrary to when the material is sandwiched between two electrodes, field lines have to curve and penetrate into the thickness of the film, see II.7. The effective distance between the electrodes is then different from a.

In Ref. [96], the authors proposed corrections to the capacitance and polarisation measurements with IDE based on mathematically transforming the IDE geometry into a standard parallel plates configuration. They also verified their model with finite elements modelling and experimental data.

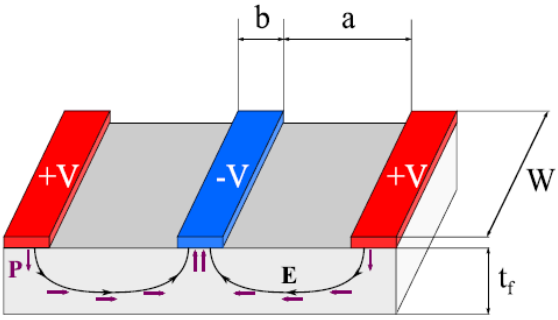

Figure II.7: Schematic representation of a film in an interdigitated electrodes geometry, highlighting the curvature of the electric field close to the electrodes. Adapted from [96].

For the electric field E, this model can be summarised as adding a correction term $\varDelta a$ to the distance a in between the electrodes. This correction term $\varDelta a$ is directly due to the curvature of the electric field lines. The electric field value, previously $E = V/a$ becomes $E = \frac{V}{a+\varDelta a}$, where $\varDelta a \approx 1.324 t_f$ with t_f film thickness.

For capacitance C, $C = \frac{S}{a}\varepsilon_0\varepsilon$ becomes $C = \varepsilon_0\varepsilon\frac{(2N+1)Wt_f}{a+\varDelta a}$, with N the number of interdigitated fingers and W their width.

This model has however some limitation: the gap between electrodes a and the finger width b should be greater than the thickness of the films t_f, to ensure no deviation from the corrected physical values. The finger length W should also be much greater than the gap a or finger width b, to ensure that no stray field from the tip of the fingers influence the field in between the fingers.

Experimental setup

An aixACCT Thin Film analyzer 2000 was used for the dielectric characterisation. Tips are used to contact electrodes on the surface on the films. The bottom electrode is accessed by contacting with silver pain the cross-section of the film with the surface or by short-circuiting two top electrodes through the film thickness. Voltages up to 400 V can be applied thanks to an amplifier. The frequency of measurement can range from 10 Hz to 5 kHz and the achievable temperature range is from -100 to 500 °C.

II.4 Raman spectroscopy

In that section we will focus only on first-order Raman spectroscopy in a classical macroscopic approach, without rederiving fully the quantum description of Raman spectroscopy. Most of that secion is adapted from the reference book by Hayes and Loudon [97], Cardona's reference books [98, 99] as well Mads' Weber PhD thesis [100].

II.4.a An inelastic scattering process: Stokes and anti-Stokes scattering

When visible light is shone on a material, it can be reflected, absorbed or scattered. This scattering can either be elastic or inelastic, which is the phenomenon allowing Raman spectroscopy.

Let's call $\hbar\omega_i$ and $\vec{k_i}$ (respectively $\hbar\omega_f$ and $\vec{k_f}$) incident (respectively scattered) photon energy and photon linear momentum.

In elastic scattering, scattered photons will have the same energy and momentum as incident photons, i.e: $(\hbar\omega_f - \hbar\omega_i,\ \vec{k_f} - \vec{k_i}) = (0, \vec{0})$.

However, for inelastic scattering, energy and momentum of scattered and incident photons will be different: $(\hbar\omega_f - \hbar\omega_i,\ \vec{k_f} - \vec{k_i}) \neq (0, \vec{0})$. However, it is important to note that these quantities are conserved during scattering: $\hbar\Delta\omega$ is the difference in energy and $\Delta\vec{k}$ the momentum difference.

Predominantly, light scattering by solids is elastic scattering. This elastic scattering is called Rayleigh scattering, as it is due to the very high wavelength (order of magnitude: 0.5 µm) compared to the distance between atoms in the material (order of magnitude: 1 Å). The intensity of Rayleigh scattering scales with the wavelength as λ^{-4}.

Inelastic light scattering is usually divided in two categories: Stokes and anti-Stokes scattering. In Stokes scattering (respectively anti-Stokes), scattered phonons have a lower energy (respectively higher) than incident phonons.

This process is represented on Fig. II.8 in the case of a system with two different vibrational levels $|n\rangle$ and $|n+1\rangle$ under illumination by a laser source of photon energy $\hbar\omega_i$. The difference of energy between levels $|n+1\rangle$ and $|n\rangle$ is $\Delta\hbar\omega$.

For Rayleigh scattering, the system in state $|n\rangle$ will populate a virtual state of to then release a photon of same energy $\hbar\omega_i$ and go back to the initial state $|n\rangle$. For Stokes scattering, the system will be "excited" from the level $|n\rangle$ to the level $|n+1\rangle$ through the scattering of a photon of energy $\hbar(\omega_i - \Delta\omega)$, lower than the incident photon energy $\hbar\omega_i$. Anti-Stokes scattering is then the opposite process of a "deexcitation" of the system from the state $|n+1\rangle$ to $|n\rangle$ through photon scattering of energy $h(\omega_i + \Delta\omega)$.

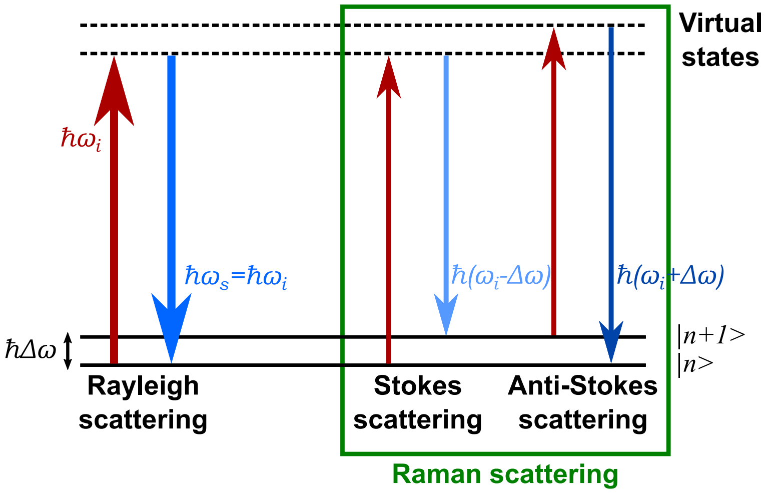

Figure II.8: Schematic principle of Stokes and anti-Stokes inelastic scattering measured in Raman spectroscopy.

II.4.b Macroscopic principle of first-order Raman spectroscopy

In that subsection we will highlight the formalism of classical Raman spectroscopy and its link to the dielectric permittivity of the probed material.

The incident monochromatic light is modelled as an electromagnetic wave of electric field:

$$\vec{E}(\vec{r},\omega_i) = \vec{E_0}e^{i\vec{k_i}\cdot\vec{r}-i\omega_i t} + \vec{E_0}^{*}e^{-i\vec{k_i}\cdot\vec{r}+i\omega_i t}$$

To simplify, we will write the field as $\vec{E}(\vec{r},\omega_i) = \vec{E_0}e^{i\vec{k_i}\cdot\vec{r}-i\omega_i t} + c.c.$, where $c.c.$ stands for complex conjugate.

The polarisation induced by this electric field:

$$\vec{P}(\vec{r},\omega_i) = \vec{P_0}e^{i\vec{k_i}\cdot\vec{r}-i\omega_i t} + c.c.$$

At equilibrium, i.e. without any excitation of the material, polarisation and field are linked by the dielectric permittivity χ: $\vec{P} = \varepsilon_0\chi\vec{E}$.

However, under a small perturbation due to an excitation $\widetilde{V}$, written as $\widetilde{V} = \widetilde{V_0}e^{i\vec{k_0}\cdot\vec{r}-i\omega_0 t} + c.c.$, of frequency ω_0 much lower than the incident light ω_i and momentum k_0, we can rewrite the permittivity of the system as a Taylor expansion with respect to the excitation $\widetilde{V}$:

$$\chi = \chi^{(0)} + \chi^{(1)}\widetilde{V} + ...$$

To simplify, we will write only the following equations for the coordinate i (that can be x,

y or z). For any tensor T and scalar A, the notation $T_{ij}A_j$ is a shortcut to the implied sum $\sum_{j\in\{x,y,z\}} T_{ij}\ A_j$.

$$P_i = \varepsilon_0 \chi_{ij}^{(0)} E_j + \varepsilon_0 \widetilde{V}\ \chi_{ij}^{(1)}\ E_j + ... \tag{II.1}$$

$$P_i = P_i^{(0)} + P_i^{(0)} + ... \tag{II.2}$$

It is important to note that the order zero polarisation $P_i^{(0)}$ can then be rewritten as:

$$P_i^{(0)} \propto E_j \tag{II.3}$$

$$\propto e^{\vec{k_i}\cdot\vec{r}-i\omega_i t} + c.c. \tag{II.4}$$

The equation II.4 represents an electromagnetic plane wave of frequency ω_i and momentum $\vec{k_i}$, i.e this is elastically scattered light: the origin of Rayleigh scattering.

For the first-order polarisation $P_i^{(1)}$, we have:

$$P_i^{(1)} \propto \widetilde{V} E_j \tag{II.5}$$

$$\propto (e^{\vec{k_i}\cdot\vec{r}-i\omega_i t} + c.c.)(e^{\vec{k_0}\cdot\vec{r}-i\omega_0 t} + c.c.) \tag{II.6}$$

$$\propto e^{i(\vec{k_i}+\vec{k_0})\cdot\vec{r}-i(\omega_i+\omega_0)t} + e^{i(\vec{k_i}-\vec{k_0})\cdot\vec{r}-i(\omega_i-\omega_0)t} + ... \tag{II.7}$$

$$P_i^{(1)} \propto (e^{i(\vec{k_i}+\vec{k_0})\cdot\vec{r}-i(\omega_i+\omega_0)t} + c.c.) + (e^{-i(\vec{k_i}-\vec{k_0})\cdot\vec{r}-i(\omega_i-\omega_0)t} + c.c.) \tag{II.8}$$

Equation II.8 is the superposition of a wave of frequency $\omega_i + \omega_0$ and momentum $\vec{k_i} + \vec{k_0}$, i.e Stokes scattering, and a wave of frequency $\omega_i - \omega_0$ and momentum $\vec{k_i} - \vec{k_0}$, i.e the anti-Stokes. These three contributions to the polarisation are directly visible in a Raman spectrum, as shown in Fig. II.9.

Stokes and anti-Stokes are however not symmetrical processes. Stokes scattering happens much more often at lower temperatures, indeed, to have Stokes scattering, you require the system can be either in a ground vibrational state or an excited state, while anti-Stokes require the system to be in an excited vibrational state only. Experimentally, Stokes is usually the only measured part of the spectrum as it is the strongest inelastic process. Taking into account the Bose-Einstein factor, $n(\omega) = \frac{1}{\exp{(\hbar\omega/k_B T)}-1}$, the ratio between intensities can be formulated as:

$$\frac{I_{\text{Stokes}}}{I_{\text{Anti-Stokes}}} = \frac{[n(\omega)+1]}{n(\omega)}$$

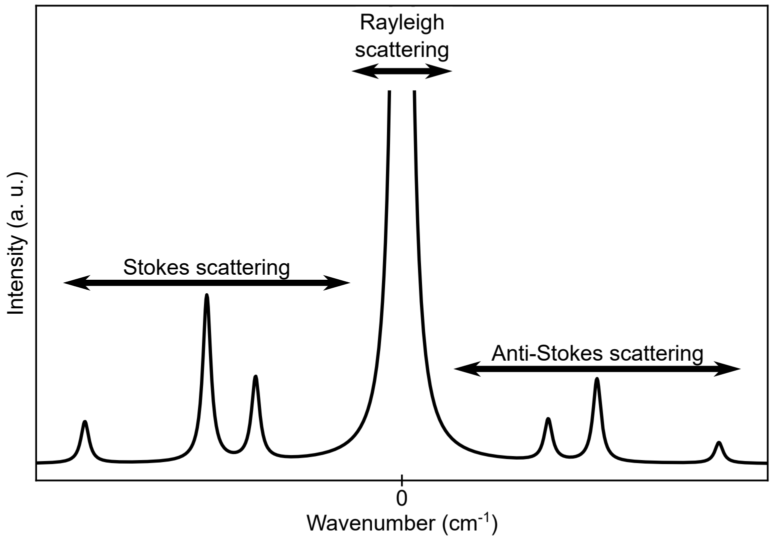

Figure II.9: Schematic of a Raman spectrum with three excitations centered on 0 cm^{-1} to display peaks due to both Stokes and anti-Stokes scattering.

From that ratio, fitting Stokes and anti-Stokes peaks linked to the same excitation can allow us to estimate the temperature of the system under specific conditions extensively described in Ref. [101]. This can be useful in low temperature measurements where thermal inertia due to a holder or the size of a sample can link to a high difference of temperature between what is displayed by the cryostat thermocouple and the actual sample temperature.

II.4.c Raman tensor

The second-rank Raman tensor is the first-order $\chi^{(1)}$ of permittivity χ in its Taylor expansion with respect to a small excitation $\widetilde{V}$. As such, $\chi^{(1)}$ can be expressed as:

$$\chi_{ij}^{(1)} = \sum_{k\in\{x,y,z\}} \left(\frac{\partial \chi_{ij}}{\partial \widetilde{V}}\right)_0$$

The elements of the Raman tensor depend entirely on the point group symmetry of the studied crystal. Any excitation $\widetilde{V}$ for which $\chi^{(1)}$ is non-zero leads to inelastic scattering: this excitation $\widetilde{V}$ is then said to be Raman-active. However, this condition is not enough to make sure that a peak due to that excitation will be visible in the Raman spectrum (see below).

It is important to note that $\chi^{(1)}$ is the first-order of the *electric susceptibility*, which means that any excitation changing the polarisability of the crystal is Raman-active.

II.4.d Raman cross-section

The Raman cross-section σ is the physical quantity representing the intensity decrease of the beam due to either Stokes or anti-Stokes scattering. This quantity σ is usually better represented as a spectral differential cross-section $\frac{d^2\sigma}{d\varOmega d\omega_s}$ that will not be derived here. It represents the loss of light intensity in the scattered beam of frequency ω_s in a volume V with a solid angle $d\varOmega$. For Stokes scattering, it is proportional to:

$$\frac{d^2\sigma}{d\varOmega d\omega_s} \propto V\ \omega_i \omega_s^3\ \frac{n_s}{n_i}\ \{n(\omega_\sigma + 1)\}\ L(\omega)\ |\langle\chi^{(1)}\rangle|^2$$

V is the scattering volume, ω_i (respectively ω_s) frequency of incident (respectively scattered) light, n_i (respectively n_s) the refractive indices of incident (respectively scattered) light, $n(\omega)$ is the Bose-Einstein occupation factor $n(\omega) = \frac{1}{\exp{(\hbar\omega/k_B T)} - 1}$ and $L(\omega)$ is the line-width of the Raman peak. This line-width L can be written as the imaginary part of the damped harmonic oscillator function, i.e. $L(\omega) = \frac{\omega\varGamma_0}{(\omega_0^2-\omega^2)^2+\omega^2\varGamma_0^2}$, where ω_0 and $\varGamma_0$ are respectively frequency and damping of the oscillator's mode. In case of a small damping, i.e at high values of wavenumbers/Raman shift, L can be approached by a Lorentzian linewidth: $L(\omega) \approx \frac{\varGamma_0/4\omega_0}{(\omega_0-\omega)^2+(\varGamma_0/2)^2}$. For soft-mode phase transitions, the damping factor increases near the transition and so Raman peaks cannot be fitted by Lorentzian lineshapes.

The quantity $|\langle\chi^{(1)}\rangle|^2$ is the projection of the Raman tensor in the basis of the incident and scattered electric field: $|\langle\chi^{(1)}\rangle|^2 \propto |\sum_{m,n} \vec{e}_{s,m}\chi^{(1)}_{mn}\vec{e}_{i,n}|^2$. The scattering setup (in reflection or transmission) and the orientation of the crystal with respect to the polarisation of incident and scattered light will select which Raman-active excitations are visible in the spectrum. The experimental setup will hence define the Raman selection rules.

Probing of the Brillouin zone limited in first-order Raman spectroscopy

This is due to the fact that *visible light* has a negligible momentum transfer compared to the size of the Brillouin zone.

Indeed, in a solid, the size of the Brillouin is of the order of $\frac{2\pi}{a} \approx 10^{-10}$ where a is the lattice parameter of the crystal of the order of 5 Å. While the momentum transferred by light is of the order of $\frac{2\pi}{\lambda_{\text{visible}}} \approx 10^{-6}$ because λ_{visible} is of the order of 0.5 µm.

Therefore, the momentum transferred $|\varDelta k|$ in a Stokes/Anti-Stokes scattering is close to zero and then why first-order Raman scattering is only able to probe the Brillouin zone center, i.e the $\varGamma$ point.

We will not detail second (or higher)-order Raman processes as this technique has not been used in this work.

II.4.e Experimental setup

Our setup is a Renishaw InVia micro-Raman spectrometer equipped with 5 laser lines of wavelength 325, 442, 532, 633 and 725 nm. The incident light has a controllable polarisation state and is focused on a sample using microscope objectives mounted on a Leica microscope. The focused beam allow to do micrometer-scale Raman spectroscopy.

After reaching the sample, the light is scattered by the sample and the light is collected in reflection by the same objective used to focus the incident laser light. Scattered and incident light are separated from the by using a half-reflecting coating on the optics. The Rayleigh scattering is then filtered out and an analyser is used to select the polarisation of the scattered light. This scattered light is then dispersed by a grating before being collected by a CCD camera and integrated numerically. Gratings of 1200, 1800 and 2400 lines/mm are used to be able to either cover a wide range of wavenumbers or to have a high spectral resolution in a limited range. A grating of 300 lines/mm is also available to run photoluminescence measurements.

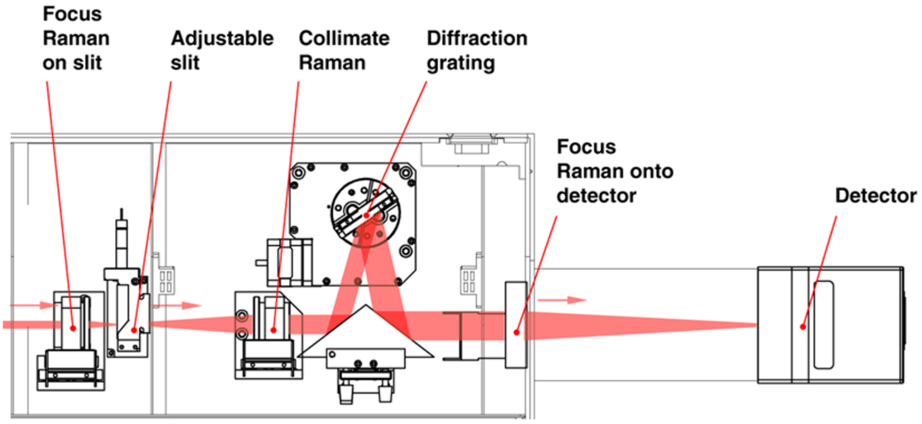

Figure II.10: Renishaw spectrometer setup. Adapted from the Renishaw InVia documentation.

A Linkam THMS600 stage and an Oxford Instruments Microstat-Hire open-cycle liquid helium cryostat can be coupled to the spectrometer to ensure a diversity of temperatures. It is also possible to electrically connect the samples inside of the temperature stage and cryostat to apply a field on the sample.

II.5 Inelastic x-ray scattering (IXS)

II.5.a Studying phonons with x-rays

Stokes and anti-Stokes scattering by phonons also happen when the incident photon wavelength is of the same order of magnitude than the lattice parameter of the crystalline structure. In that case the light is in the x-ray wavelength range ($\lambda \approx$ a few Å) and so the x-ray has a non-zero momentum compared to the size of the Brillouin zone.

The transfer of the momentum $|\Delta k|$ by the incident beam is then non-zero hence why the Brillouin zone is entirely accessible by inelastic x-ray scattering: this technique enables us to study phonons modes at zone center, zone boundary or any intermediate point in the Brillouin zone. Hence the possibility to probe phonon dispersion in IXS.

This is particularly interesting for the study of antiferroelectric phase transitions as antipolar phonon modes can be located outside of the zone center, i.e. away from the Γ point.

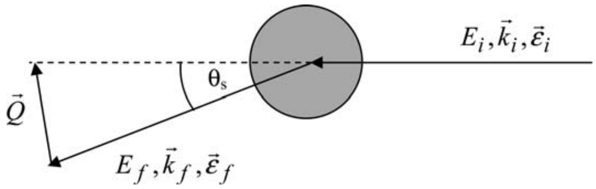

Figure II.11: Schematic principle of inelastic scattering. $(E_i, \vec{k_i}, \vec{\varepsilon_i})$ represent respectively photon energy, linear momentum and polarisation vector of the incident photon. $(E_f, \vec{k_f}, \vec{\varepsilon_f})$ the same quantities of the scattered photon. $E_f - E_i$ and $\Delta\vec{k}$ are the transferred energy and linear momentum. Adapted from [102].

II.5.b IXS cross-section

As for Raman spectroscopy, the IXS differential cross-section is the measured quantity during an IXS experiment.

$$\frac{d^2\sigma}{d\Omega d\omega_s} \propto (\varepsilon_i \cdot \varepsilon_f)^2 \, \frac{k_i}{k_f} \, |f(\Delta k)|^2 \, S(\Delta k, E_f - E_i)$$

With ε_i (respectively ε_f) polarisation and k_i (respectively k_f) momentum of the incident (respectively scattered) beam. $f(\Delta k)$ is the form factor of the scatterers and $S(\Delta k, E_f - E_i)$ the structure factor.

II.5.c Experimental setup of the ID28 beamline at ESRF

The inleastic x-ray scattering experiments in this work have been performed at the ESRF ID28 beamline [103]. It is divided in two different stations (Fig. II.12): the main inelastic x-ray scattering station and the side station dedicated to thermal diffuse scattering.

On the IXS side, the beam goes through several monochromators that will reduce progressively the energy span ΔE of incident photons and hence the energy resolution of the experiment. This however goes with a drastic reduction of the beam intensity, hence why inelastic x-ray scattering is usually only performed in synchrotrons to take advantage of the very high fluence. The incident beam hits the sample in a reflection geometry and the scattered beam then goes through silicon spherical analysers that act as a grating. Depending on the choice of silicon reflection, the energy resolution of the experiment can be as low as 1.0 meV (Si (13, 13, 13) reflection, very low IXS intensity) and the linear momentum resolution can reach as low as 1.89 nm^{-1} (Si (7, 7, 7) reflection, high IXS intensity).

An Oxford Intruments Cryostream allows to control the sample temperature.

A key figure of merit for such an experiment is the ratio $\frac{\Delta E}{E}$ representing the energy span of different photons in the beam with respect to the average photon energy E. The lower this ratio is, the higher the resolution of the measured spectrum will be.

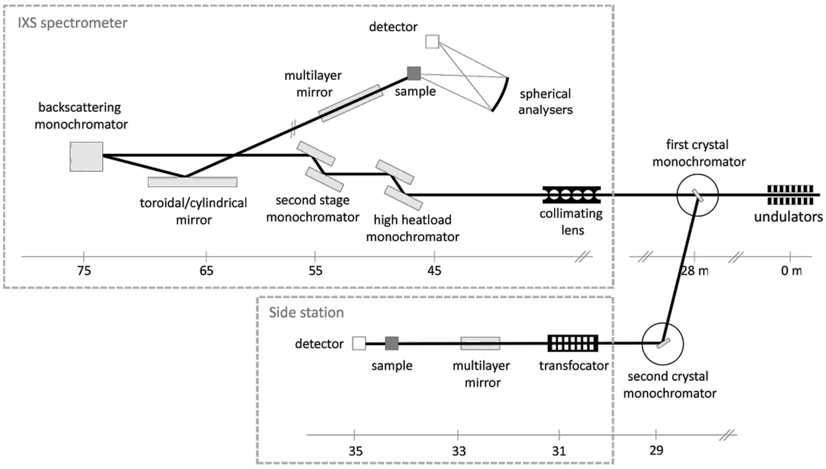

Figure II.12: Schematic view of the experimental hall of the ESRF ID28 beamline. Adapted from [103].

II.6 Thermal diffuse scattering (TDS)

In imperfect crystals, a continuous background of weak intensity is present in diffraction experiments. This background decreases the intensity of Bragg peaks and is called diffuse scattering, which can arise from many different factors. Generally, every phenomenon that induces a difference (or disorder) of the studied lattice with respect to the perfect lattice, such as defects, lattice vibrations or other disordered, can give rise to diffuse scattering [104].

Here, we will focus only on the thermal diffuse scattering (TDS) from phonons populated due to a non-zero temperature, as this scattering can give information on the phase transition dynamics [105].

In crystals displaying a phase transition due to a single mode, we can follow that mode in TDS. For the need of this work, it is enough to say that when a single phonon having a strong frequency dependency in temperature, the intensity of the thermal diffuse scattering will be such as:

$$I_{TDS}(\vec{Q}) \propto \frac{1}{\omega(\vec{q})} \coth\left(\frac{\hbar\omega(\vec{q})}{2k_BT}\right) f(\vec{Q})^2 \tag{II.9}$$

Where ω is the frequency of the mode, T the temperature of the crystal and $f(\Delta k)$ is the form factor of the scattering phonon. This form factor can be numerically fitted from inelastic x-ray data.

Experimental setup

These thermal diffuse scattering experiments have been performed at the ID28 beamline where inelastic x-ray experiments, presented before, were performed.

Chapter III

Antiferroelectric switching of $PbZrO_3$ sol-gel polycrystalline thin films

Lead zirconate $PbZrO_3$ is the antiferroelectric material which has been used as a model since the 1950s and is still currently considered to be the canonical model of antiferroelectricity in the inorganic perovskites community. $PbZrO_3$, and derived compounds, is also potentially one of the most interesting antiferroelectric for thin films and ceramics applications, due to its proximity in composition to ferroelectric PZT and despite it containing lead.

In that chapter, we will show our results on the synthesis and characterisation of lead zirconate $PbZrO_3$ thin films processed by chemical solution deposition and on multiple substrates and sample geometries.

First, we will review some of the first successful attempts at sol-gel synthesis then present and try to explain the wide distribution of critical fields $E_{\mathrm{AFE}\to\mathrm{FE}}$ and saturation polarisation P_s observed in literature. The debates around $PbZrO_3$ polar phase symmetry will be highlighted. In the next section, we will show our synthesis protocol and the characterisation without applied electric field. After that, we will study the field-induced in-plane and out-of-plane antiferroelectric switching of our thin films. A discussion on the anisotropy of the switching field will be formulated by comparing our results to literature data. Finally, we will summarise the results obtained and consider the next steps possible for this study.

III.1 Literature review on $PbZrO_3$ thin films

III.1.a Overview of sol-gel film synthesis of $PbZrO_3$

Up until the 1990s, $PbZrO_3$ was mostly studied as a ceramic or single crystal. However, with technological improvements and the sol-gel synthesis of closely-related compounds ferroelectric lead zirconate titanate PZT [106] or antiferrolectric PLZT [107], a new interest rose to synthesise pure lead zirconate $PbZrO_3$ films. However, it proved to be more difficult to deposit than other members of the PZT/PLZT oxides family, notably due to an easy cracking of the surface and a non-negligible portion of parasitic pyrochlore phase in the films. The lack of early studies was also probably linked to, at the time, few application possibilities of antiferroelectric thin films and the easier synthesis of antiferroelectric PLZT.

Hereafter, we will mostly focus on describing the synthesis of pure $PbZrO_3$ thin films by sol-gel processes to ensure an easy comparison with our films. To our knowledge, one of the oldest published paper displaying a good electrical behaviour of $PbZrO_3$ sol-gel film is Ref. [28]. In that paper, the authors only briefly summarise their dip-coating synthesis method and are mostly interested in the electro-optic properties of their films. It is however worth noting that they deposited their films on both a Ti-coated silicon substrate and fused quartz. The polarisation curves obtained in that paper are shown in Fig. III.1 and display a critical field $E_{\mathrm{AFE}\to\mathrm{FE}}$ of $250\,\mathrm{kV\,cm^{-1}}$ and saturation polarisation P_s of around $24\,\mathrm{\mu C\,cm^{-2}}$. A later work of the same group [108] give a bit more insight into the process: they dissolved powders of lead subacetate into a solution of zirconium acetate and diluted with methanol before proceeding with dip-coating. The films were then annealed at 700 °C for 2 minutes. However, scanning electron microscope micrographs reveal cracking of the surface for both substrates used.

A more systematic study of the influence of lead precursors on the properties of $PbZrO_3$ was performed in Ref. [84] and formed the basis for our process. Substrates used comprised of $Pt/TiO_2/Si$ and $TiO_2/TiO_2/SiO_2/Si$. A mixture of n-butanol and 2-methoxethanol were used to dissolve either lead oxide or lead acetate and a pre-dissolved solution of zirconium n-butoxide/n-butanol. Films using lead oxide precursors and deposited on a $TiO_2/TiO_2/SiO_2/Si$ substrate displayed a high crystallinity, good microstructure, a clear dielectric anomaly around 220 °C and antiferroelectric switching. These two last properties are displayed on Fig. III.2.

To get a clear idea on the quality of our films, we performed an extensive literature review of pure $PbZrO_3$ films. All the information is summarised in Table III.1. On Fig. III.3, we report every sample found in the literature for which a room temperature value of $E_{\mathrm{AFE}\to\mathrm{FE}}$ and of P_s

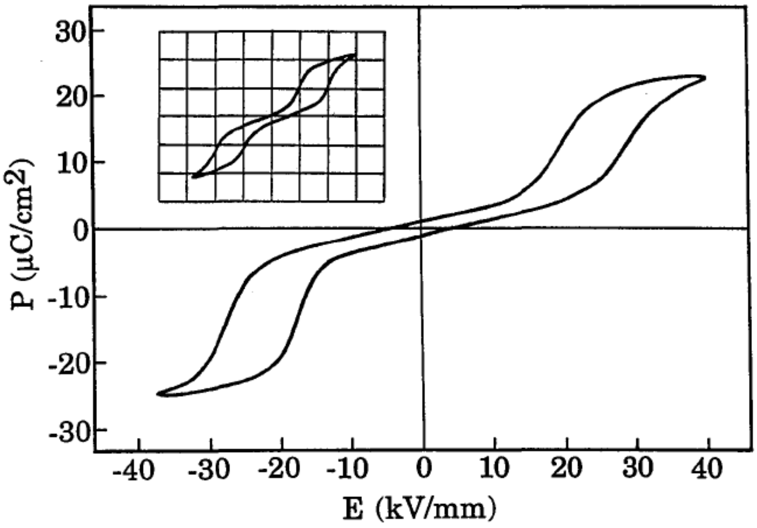

Figure III.1: Polarisation curves of a 650 nm-thick dip-coated $PbZrO_3$ film on a Ti-coated silicon substrate. The main curve was measured by applying a dc field while the inset was measure with an ac field. Adapted from [28].

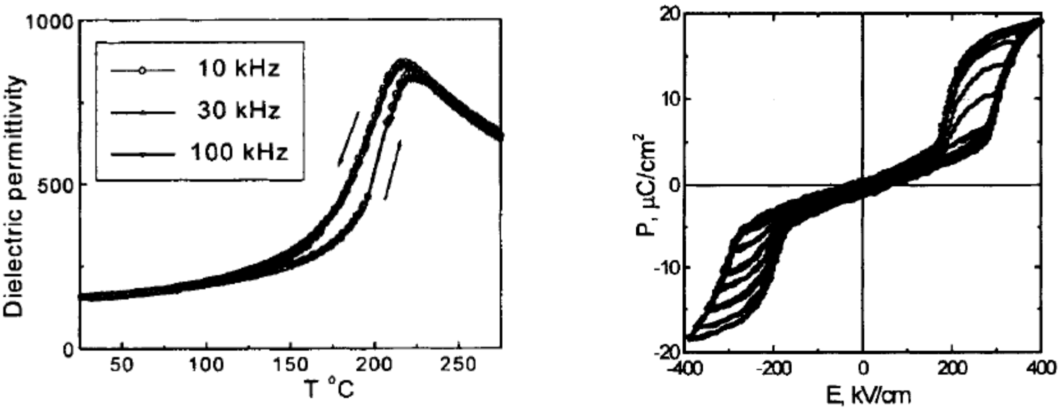

(a)

(b)

Figure III.2: (a) Temperature-dependent permittivity measurements of a $PbZrO_3$ film displaying a clear dielectric anomaly around 220 °C. (b) Polarisation curves of a 900 nm-thick $PbZrO_3$ film on a $TiO_2/TiO_2/SiO_2/Si$ substrate. Adapted from [84].

was published or could be graphically extracted from the figures, regardless of the film deposition technique used. One of the constraints we however gave ourselves was to report only pure, i.e. non-doped, $PbZrO_3$ films. Error bars of $\pm$ 10 % have been arbitrarily defined to reported values to take into account as much as possible errors due to graphical extraction of data. It is also important to note that the value of P_s reported here are following the definition we gave in chapter II and hence are often enough different from the values reported in the cited papers.

If we compare only sol-gel processed $PbZrO_3$ films together, there is a very broad distribution of both critical field $E_{\mathrm{AFE}\to\mathrm{FE}}$ and saturation polarisation P_s. Critical fields roughly range from

100 to 700 kV cm^{-1} and P_s varies from 20 to 45 µC cm^{-2}. Taking into account sputtered and PLD films, this distribution of $E_{\mathrm{AFE}\to\mathrm{FE}}$ and P_s values is only wider. It is worth noting that PLD films seem to have a higher polarisation than films processed by other methods.

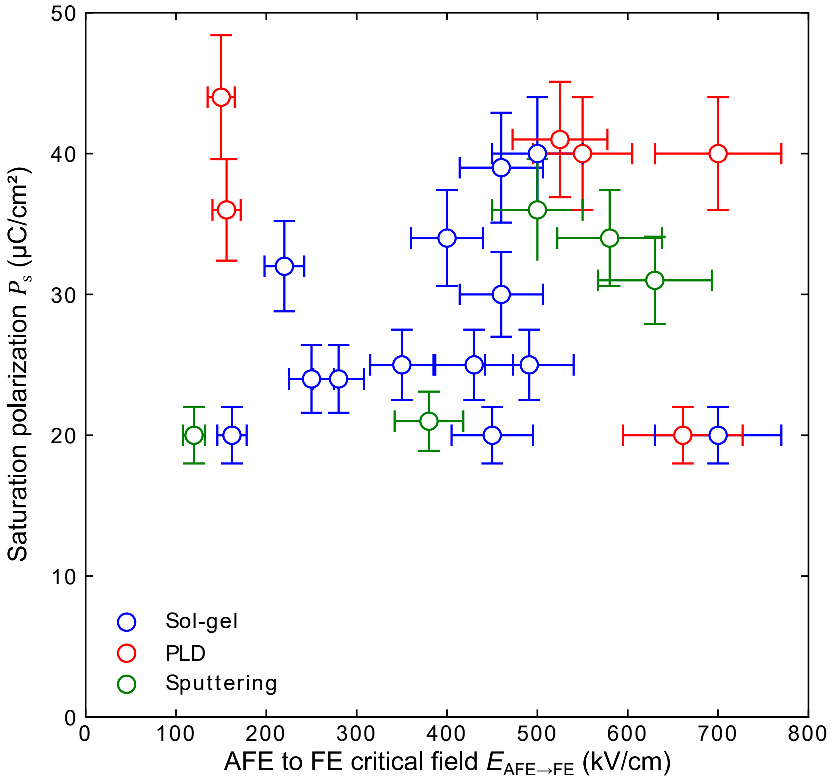

Figure III.3: Literature review of critical fields $E_{\mathrm{AFE}\to\mathrm{FE}}$ and saturation polarisation P_s of pure $PbZrO_3$ sol-gel, pulsed laser deposited and sputtered samples. All these values have been measured at room temperature. Some values were graphically extracted from literature. References can be found in Table III.1.

First, it should be noted that these processed films also have very different thicknesses, substrates, synthesis methods and others. Still, a multitude of factors could explain this wide distribution of critical field $E_{\mathrm{AFE}\to\mathrm{FE}}$ values. For instance, film strain could affect the energy difference between antiferroelectric and polar phase. In pulsed laser deposited films, epitaxial strain is one of the most usual factors to tailor phases of oxides but in polycrystalline films, residual strains are due to a mismatch of thermal expansion coefficients between substrate and film. Errors on film thickness can also influence the critical field. Potential defects for instance due to reagent impurity levels or process could also explain a variation of $E_{\mathrm{AFE}\to\mathrm{FE}}$. In polycrystalline films, there is a wide range of grain size possible and hence very different numbers of grain boundaries can affect $E_{\mathrm{AFE}\to\mathrm{FE}}$. Also, for polycrystalline films, the microstucture (columnar growth, spherical grains...) can lead to a difference in critical fields, due to field lines crossing a different amount of boundaries.

Thick. (nm)	$E_{\mathrm{AFE}\rightarrow\mathrm{FE}}$ (kV cm^{-1})	$E_{\mathrm{FE}\rightarrow\mathrm{AFE}}$ (kV cm^{-1})	P_{s} (µC cm^{-2})	Film orient.	Substrate (bottom → top)	Ref.
Sol-gel thin films						
85	501	239	25.3	(002)$_{\mathrm{o}}$	Si/SiO$_2$/TiO$_{\mathrm{x}}$/Pt	MIM
170	425	233	22.3	(002)$_{\mathrm{o}}$	Si/SiO$_2$/TiO$_{\mathrm{x}}$/Pt	MIM
255	**495**	**296**	**24.4**	(002)$_{\mathrm{o}}$	Si/SiO$_2$/TiO$_{\mathrm{x}}$/Pt	MIM
85	219	95	21.9	(002)$_{\mathrm{o}}$	SiO$_2$/HfO$_2$	IDE
170	333	170	35.8	(002)$_{\mathrm{o}}$	SiO$_2$/HfO$_2$	IDE
255	**286**	**134**	**17.7**	(002)$_{\mathrm{o}}$	SiO$_2$/HfO$_2$	IDE
120	162	-	20	(111)$_{\mathrm{pc}}$	Si/SiO$_2$/Ti/Pt	[109]
500	350	260	25	(111)$_{\mathrm{pc}}$	Si/???/Pt	[110]
496	430	300	25	(111)$_{\mathrm{pc}}$	Si/SiO$_2$/Ti/Pt	[111]
500	460	250	30	(111)$_{\mathrm{pc}}$	Si/SiO$_2$/Ti/Pt	[112]
-	250	125	-	(100)$_{\mathrm{pc}}$	Si/SiO$_2$/Ti/Pt	[113]
450	450	-	20	(100)$_{\mathrm{pc}}$	Si/SiO$_2$/Ti/Pt/LaNiO$_3$	[90]
900	700	-	20	(100)$_{\mathrm{pc}}$	Si/SiO$_2$/Ti/Pt/LaNiO$_3$	[90]
248	491	193	25	(100)$_{\mathrm{pc}}$	Si/SiO$_2$/Ti/Pt	[114]
575	460	200	39	(001)$_{\mathrm{pc}}$	Si/SiO$_2$/Ti/Pt	[115]
900	500	230	40	(001)$_{\mathrm{pc}}$	Si/SiO$_2$/Ti/Pt/LaNiO$_3$	[116]
650	250	-	24	-	Si/???/Ti/Pt	[28]
650*	180*	*	*	*	SiO$_2$*	[28]*
800	400	200	34	Mixed	Si/???/Ti/Pt + TiO$_2$	[108]
330	280	-	24	(100)$_{\mathrm{pc}}$	Si/SiO$_2$/Ti/Pt	[117]
330	220	-	32	(111)$_{\mathrm{pc}}$	Si/SiO$_2$/Ti/Pt/TiO$_2$	[117]
Pulsed laser deposition (PLD) thin films						
-	150	80	44	(122)$_{\mathrm{o}}$	Si/???/Pt	[118]
500	156	84	36	(110)$_{\mathrm{pc}}$	Si/???/Pt	[119, 120]
390	550	300	40	(120)$_{\mathrm{o}}$	SrTiO$_3$/SrRuO$_3$	[121]
100	700	300	40	(001)$_{\mathrm{o}}$	SrTiO$_3$/BaZrO$_3$/BaPbO$_3$	[121]
512	661	400	20	(100)$_{\mathrm{pc}}$	Si/SiO$_2$/Ti/Pt	[111]
1000	525	300	41	(001)$_{\mathrm{pc}}$	Si/Ca$_2$Nb$_3$O$_{10}$/SrRuO$_3$	[122]
Sputtered thin films						
360	630	365	31	(001)$_{\mathrm{pc}}$	Si/SiO$_2$/LaNiO$_3$	[123]
300	380	200	21	(001)$_{\mathrm{pc}}$, ep.	LaNiO$_3$/SrTiO$_3$	[124]
300	580	380	34	(110)$_{\mathrm{pc}}$, ep.	LaNiO$_3$/SrTiO$_3$	[124]
300	500	320	36	(111)$_{\mathrm{pc}}$, ep.	LaNiO$_3$/SrTiO$_3$	[124]
3000	80	120	20	Random	Si/SiO$_2$/Ti/Pt	[125]

Table III.1: Review of papers reporting antiferroelectric switching of undoped PbZrO$_3$. All measurements have been conducted at room temperature and with an out-of-plane field equivalent to our MIM geometry, except for the starred * sample where the field was applied in-plane. "ep." stands for epitaxial. In the Ref. column, "MIM" and "IDE" indicate our synthesised films.

Finally, film orientation can also vary drastically the value of the critical field $E_{\mathrm{AFE}\to\mathrm{FE}}$, as $PbZrO_3$ is, like many inorganic perovskites, a very anisotropic material.

To understand more accurately how all of these factors influence the critical field, it is necessary to study in detail the antiferroelectric switching mechanism of $PbZrO_3$. To that end, we need to discuss the nature of the end point of the antiferroelectric switching, i.e. the polar phase and its symmetry.

III.1.b Importance of the polar phase of $PbZrO_3$

The polar phase of lead zirconate $PbZrO_3$ has been the source of many debates until recently. It is generally considered to be rhombohedral but there is still little experimental proof confirming it.

First, it is well-documented that at Ti content above 7 %, lead zirconate titanate PZT stabilises in a ferroelectric $R3c$ rhombohedral phase [126] at room temperature. This small doping highlights the presence of a rhombohedral ferroelectric phase close to the pure $PbZrO_3$ orthorhombic $Pbam$ phase.

DFT calculations have generally confirmed the quasi-degeneracy in energy of the antiferroelectric ground state and a ferroelectric state. For instance, in Ref. [127], a difference of 0.021 eV/f.u. is found between the antiferroelectric ground state of $Pbam$ space group and the ferroelectric rhombohedral state, that is confirmed to be the same that in PZT in the low Ti region. This conclusion is also reinforced in Ref. [26], where they also estimate the needed electric field $E_{\mathrm{AFE}\to\mathrm{FE}}$ to switch from antiferroelectric to ferroelectric phase to be around $1.1\,\mathrm{MV\,cm^{-1}}$ if applied along the $(111)_{\mathrm{pseudo-cubic}}$ direction. The calculatedpolarisation in the polar phase is of $55\,\mathrm{\mu C\,cm^{-2}}$, of the same order of magnitude than for some of the PLD films found in the literature, Fig. III.3. These estimations coming from DFT usually largely overestimate critical fields, because they do not account for defects, domains and other experimental parameters that can decrease drastically these values. In [128], authors show numerically that compressive epitaxial strain in the $(001)_{\mathrm{c}}$ matching plane can stabilise the rhombohedral ferroelectric $R3c$ phase, while tensile strain for the same film tends to stabilise the orthorhombic $Pbam$ phase. More recently [129], the energy difference between $PbZrO_3$ ground $Pbam$ ground state and ferroelectric $R3c$ phase was found to be around 4 meV and the volume difference between this phase is 0.5 %. Polarisation in the $R3c$ phase is also coherent with experiments with $59\,\mathrm{\mu C\,cm^{-2}}$. They also show that adding an off-stoichiometric excess of lead can stabilise the material in a polar $R3c$ perovskite phase.

Experimentally [130, 131], authors have imaged in-situ the antiferroelectric switching of $PbZrO_3$-

based ceramics by transmission electron microscopy (TEM). This field-induced phase is coherent with the rhombohedral symmetry proposed by DFT calculations. An x-ray diffraction study of Ba-substituted and Sr-substituted $PbZrO_3$ [132] also highlights the presence of a ferroelectric rhombohedral phase, when $PbZrO_3$ has more than 20 % of Ba replacing Pb. In a series of paper [38, 133, 134], Fesenko et. al. also find numerous ferroelectric phases in the phase diagram of $PbZrO_3$ and low-Ti PZT, built combining dielectric and optical measurements.

However, other theoretical studies have found a plethora of other field-induced stable structures. In Ref. [135], authors calculate that the polar phase of lead zirconate is orthorhombic $Cm2m$ (SG #38). The polar symmetry, according to [44], could also be rhombohedral $R3m$, tetragonal $P4mm$, orthorhombic $Amm2$, monoclinic Pm, monoclinic Cm or triclinic $P1$, depending on the orientation of the electric field with respect to the cubic phase. Notably, in a multiscale approach combining effective hamiltonian and DFT [136], the stability of different polar phases has been studied with respect of the direction of the applied electric field. Along $[111]_{\mathrm{pc}}$, a Cc phase is stabilised at fields lower than 400 kV cm^{-1}, along $[110]_{\mathrm{pc}}$, $Ima2$ is stabilised around 700 kV cm^{-1}, along $[001]_{\mathrm{pc}}$, $I4cm$ is stabilised around 4 MV cm^{-1}.

In the following sections, we will present our results on the synthesis and characterisation of $PbZrO_3$ thin films in different switching geometries. We will then discuss the differences observed by the influence of synthesis parameters on the critical field, with a focus on film orientation. Notably, a "toy model" of the switching mechanism will be proposed, assuming a rhombohedral polar phase.

III.2 Processing and characterisation without field of $PbZrO_3$ CSD thin films

III.2.a Solution preparation

Solutions of both lead zirconate $PbZrO_3$ (for the film) and lead titanate $PbTiO_3$ (for the orientation seed layer) are used in the processing of our $PbZrO_3$ thin films. Both solutions are prepared at LIST.

Lead(II) acetate trihydrate (99.9%, Sigma-Aldrich, USA), zirconium(IV) propoxide (70%, Sigma-Aldrich, USA), or titananium(IV) propoxide (97%, Sigma-Aldrich, USA) for $PbTiO_3$, are dissolved into anhydrous 2-methoxyethanol or 1-methoxy 2-propanol for some of the PTO solutions, then refluxed and distilled. Beforehand, zirconium and titanium precursors are mixed with the chelating agent acetylacetone, notably to ensure a stoichiometric distribution of the metallic ions in the annealed films. A lead excess of 20 % (respectively 30 %) is used in $PbZrO_3$ (respectively $PbTiO_3$) solution. The ionic concentration for $PbZrO_3$ solutions is 0.3 M and 0.1 M for $PbTiO_3$.

III.2.b Film synthesis

Droplets of the solutions are deposited on the substrate using spin-coating then dried at 130 °C and pyrolised at 350 °C for 5 minutes each. The film stack is then annealed in an air atmosphere at 700 °C for 5 minutes for $PbZrO_3$ layers or 1 minute for $PbTiO_3$ seed layers.

Every $PbZrO_3$ film presented in this work has been grown on a pre-deposited and pre-annealed $PbTiO_3$ seed layer coming from a single spin-coated layer of 0.1 M solution.

Films of 85 nm (2 layers of $PbZrO_3$ spin-coated solution) to 850 nm (4 annealed stacks of 5 layers) have been processed.

Three different types of substrates have been used in this work: platinised silicon (from top to bottom: Si/SiO_2 (500 nm)/TiO_x (20 nm)/Pt 100 nm), fused silica coated by a pre-annealed ALD-deposited HfO_2 buffer layer of thickness around 23 nm and c-sapphire substrates.

III.2.c Two different sample geometries synthesised

In this work, two main types of electrodes are deposited to switch the oxide films. Patterning of the electrodes is realised by lift-off photolithography using a MLA150 from Heidelberg Instruments. The deposition is done through platinum sputtering and the thickness of the final Pt electrode is around 100 nm.

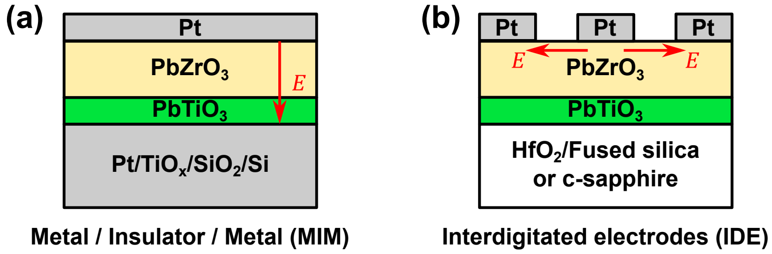

Figure III.4: Schematic view of (a) a Metal/Insulator/Metal (MIM) stack and (b) an Interdigitated electrodes (IDE) sample.

First, the Metal/Insulator/Metal (or MIM) geometry with two parallel electrodes on top and bottom of the film stack. In that case, the electric field will be applied vertically, see Fig. III.4.a. The substrate used in that geometry is only platinised silicon.

The other type of geometry is the Interdigitated electrodes (IDE) geometry, where electrodes on the surface are interlaced to apply a field in-plane, see Fig. III.4.b. Two substrates can be used in this geometry, either HfO_2-coated fused silica or c-sapphire.

III.2.d Film orientation measured by x-ray diffraction

X-ray diffraction was used to check the crystallinity of the film and their orientations. To do this, a $\theta - 2\theta$ geometry is used to compare the relative peak intensity of the films with a powder reference.

Every $PbZrO_3$ films grown on a $PbTiO_3$ seed layer with the growth conditions previously mentioned crystallised in the wanted perovskite phase. Notably, no pyrochlore phase or other parasitic phase could be seen in the x-ray diffraction patterns.

For the $PbZrO_3$ films grown on platinised silicon (MIM geometry), two different types of $PbTiO_3$ seed layers were compared, one prepared with a standard 2-methoxyethanol (2-MOE) solvent and the other with 1-methoxy-2-propanol (1M-2P).

The difference of film orientation is visible on Fig. III.5, where films using a 1M-2P-based seed layer are much more oriented along the [001] pseudo-cubic direction (Lotgering factor of 0.96) than samples grown on a 2-MOE-based seed layer (Lotgering factor of 0.50).

For IDE geometries, films on fused silica are oriented similarly and strongly along the $[001]_{\mathrm{pc}}$ with both seed layers. Only 1M-2P-based seed layers were used on c-sapphire substrates. On Fig. III.5 are represented two IDE samples: the first grown on fused silica (Lotgering factor of 0.84) and the second on sapphire (Lotgering of 0.94).

A comparison with a reference powder pattern of pure $PbZrO_3$ in the orthorhombic $Pbam$ [137] can also determine that the [001] pseudo-cubic orientation of the lattice is in the $Pbam$

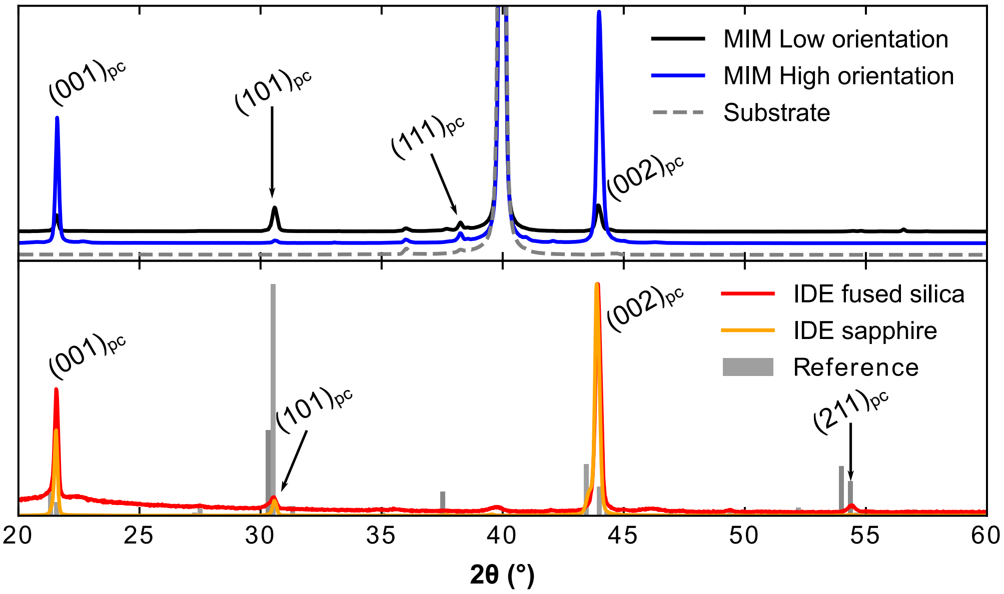

Figure III.5: Normalised x-ray diffraction patterns of (a) 255 nm-thick $PbZrO_3$ lower- and highly-oriented $PbZrO_3$ in MIM geometry (platinised silicon substrate) and (b) patterns of 255 nm-thick IDE sample deposited on fused silica and 850 nm-thick IDE sample deposited on sapphire.

orthorhomic cell of $PbZrO_3$ along the [002] orthorhombic direction.

III.2.e Film microstructure measured by SEM

Surface and cross-section of micrographs of $PbZrO_3$ have been acquired through Scanning Electron Microscopy to check the surface state, lateral grain size and thickness of the films.

On Fig. III.6, surfaces of respectively 85 and 170 nm films grown on Pt/Si (MIM geometry) display respectively grains of 86 ± 9 nm and 112 ± 13 nm lateral size.

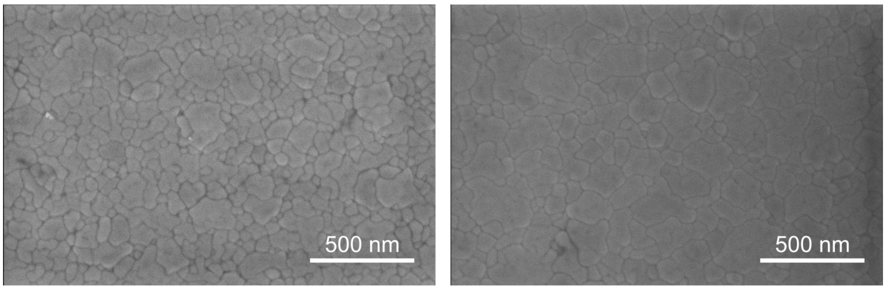

(a) (b)

Figure III.6: Scanning electron microscopy micrographs of the surfaces of (a) 85 nm-thick and (b) 170 nm $PbZrO_3$ MIM samples grown on a 1M-2P-based seed layer.

To compare the grain size, we took SEM micrographs of samples cross-section, as displayed in III.7. These two cross-sections highlight the similar grain width and the columnar structure common to the films grown on both substrates so for both sample geometries (MIM or IDE on fused silica). Taking cross-section micrographs can be especially useful for fused silica samples where surface pyrochlore is often seen. This pyrochlore phase must be a surface effect as it is not seen in x-ray diffraction.

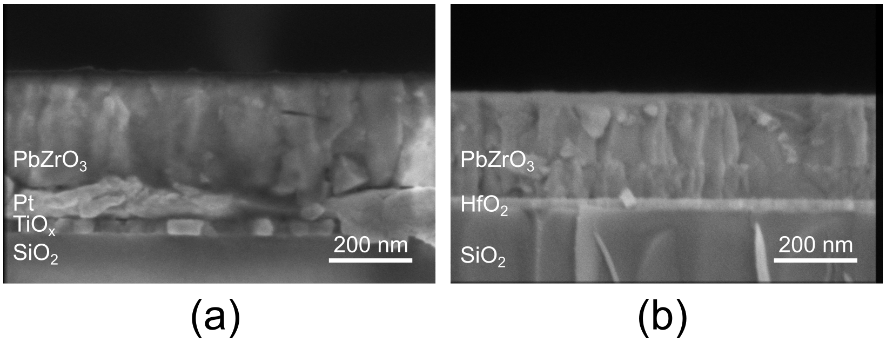

Figure III.7: Scanning electron microscopy micrographs of the cross-section of a 255 nm-thick samples: (a) MIM film grown on a 1M-2P seed layer and (b) IDE sample grown on fused silica.

III.2.f Pole figures to determine in-plane films orientation

Pole figures of a highly-oriented (i.e. using a 1M-2P seed layer) MIM sample and of a fused silica IDE samples have been measured, as shown in Fig. III.8. The three poles chosen were $(004)_{\mathrm{orthorhombic}}$ which is equivalent to the $(002)_{\mathrm{pseudo-cubic}}$, $(122)_{\mathrm{o}} = (101)_{\mathrm{pc}}$ and $(044)_{\mathrm{o}} = (112)_{\mathrm{pc}}$.

Around $(004)_{\mathrm{o}}$, the diffracted beam intensity is spread at the center of the pole figure, as expected from the film orientation. A noticeable difference is present between IDE and MIM, with the intensity gathered more tightly around the center of the pole figure in the MIM geometry than in the IDE. We interpret this difference as directly correlated with the difference of Lotgering factor, and hence of film orientation, observed between these two samples.

Around the $(122)_{\mathrm{o}}$ and $(044)_{\mathrm{o}}$ in-plane poles, the diffracted intensity is gathered in rings than are broader for the IDE sample than for the MIM sample. This difference of width can also be explained by the slight difference of texture quality between the two samples, indeed, the Lotgering factor of the studied MIM sample is 0.96 while the IDE sample has a factor of 0.84. However, the homogeneous distribution of intensity inside of these rings proves that the in-plane orientation is isotropic. This result is expected due to the growth mechanism of sol-gel thin films.

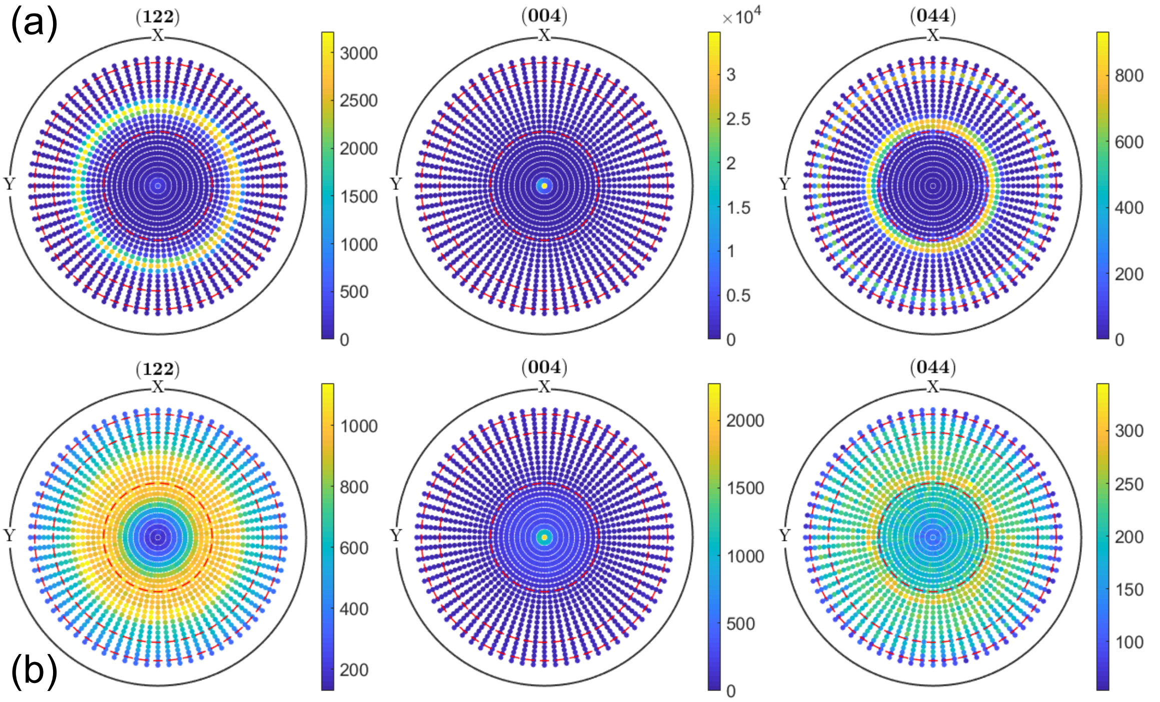

Figure III.8: Pole figures of (a) highly-oriented MIM and (b) IDE on fused silica of thickness of 255 nm

III.2.g Elemental homogeneity of the films by Secondary Ion Mass Spectroscopy

Secondary Ion Mass Spectrometry (SIMS) studies have been performed on both highly-oriented MIM and IDE on fused silica. This method allows us to verify how homogeneous in elemental composition the films are, throughout their thickness.

These measurements were run on a CAMECA C-Ultra. An area of 250 µm × 250 µm was sputtered and inside of this, a 60 µm area was bombarded by Cs^+ ions of 1 keV of energy.

To compare correctly between geometries, both films were synthesised in the same growth conditions, with the same seed layer, with 4 layers crystallised in a first annealing step then 2 extra layers in a second annealing step. The estimated thickness for both films is 255 nm.

The SIMS results are summarised on Fig. III.9 for both IDE on fused silica and MIM samples. The ratio of Pb/Zr is represented throughout the thickness of the film on Fig. III.9.a. Both films display a dip in the profile ratio around 2500 s of sputtering time and at the top surface. For 255 nm-thick samples, the process was to deposit two layers of solution on a substrate then doing a first annealing, adding four other layers of solution and finally do a last annealing. These dips in the SIMS ratio of Pb/Zr are coherent with the position of these annealings in the films. This could be explained by a slight depletion of Pb at the annealed surfaces, as lead is a very volatile element. However, it is worth noting that the SIMS Pb/Zr ratio seems to be relatively stable in the bulk of the film, and comparable in between the samples.

The signal relative to titanium Ti is shown on Fig. III.9.b. On the IDE sample on fused silica, a single sharp peak of Ti is present, signaling the presence of the seed layer. On the platinised silicon MIM sample, the figure shows only the top layer of the stack, i.e only $PbZrO_3$, $PbTiO_3$ and Pt are visible in that range, but two peaks are clearly present. The highest corresponds to the $PbTiO_3$ seed layer and the smallest corresponds to a limited diffusion of Ti from the seed layer into the bulk of $PbZrO_3$. Integrating the intensities of both peaks in the MIM sample gives a value close to the intensity of the IDE sample, proving that there is no diffusion from the substrate layer of titanium oxide TiO_x into the $PbZrO_3$ layer. This conclusion is reinforced by the zero intensity of Ti inside the substrate Pt layer.

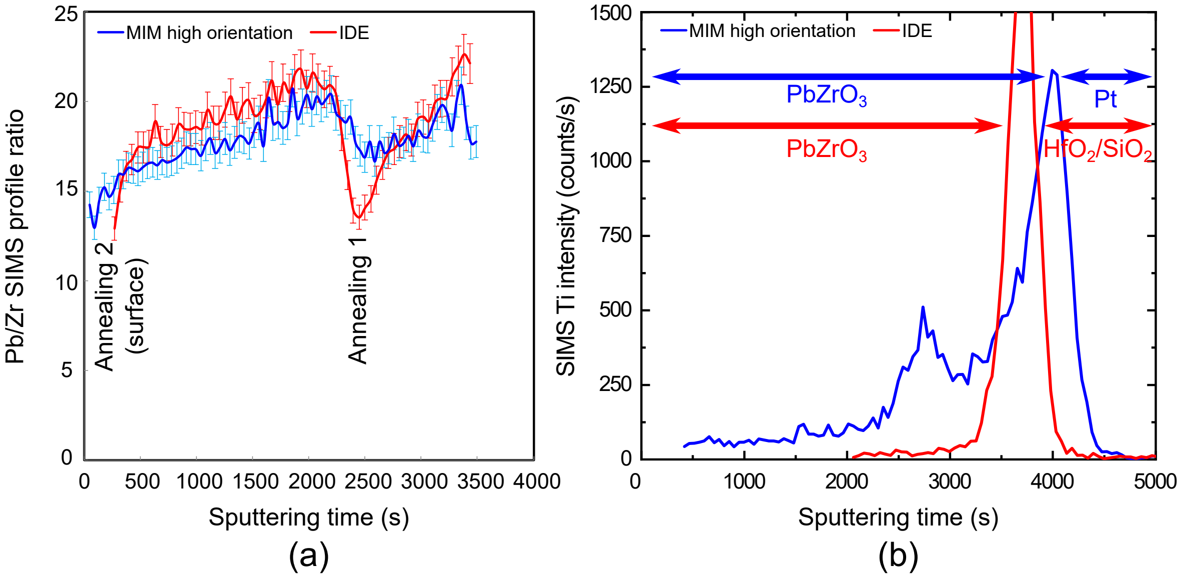

Figure III.9: (a) SIMS Pb/Zr ratio (this is not directly comparable to the stoichiometry of the film). (b) SIMS intensity of Ti through the film thickness of 255 nm-thick highly-oriented MIM sample (blue) and IDE sample on fused silica (red).

III.2.h Strain measurements by x-ray diffraction

We performed strain measurements on two different samples, one MIM grown on silicon and one IDE grown on fused silica.

The chosen reflection chosen was the pseudo-cubic $(111)_{\mathrm{pc}}$. This peak was measured as a function of the tilt angle Ψ, as shown in Figs. III.10.a. and III.10.b. The position of the $(111)_{\mathrm{pc}}$ peak shifts towards lower 2θ angles as Ψ increases in both samples. We can extract the interplanar distance $d_{(111)}(\Psi)$ from fitting these positions. Plotting $d_{(111)}(\Psi)$ with respect to $\sin^2 \Psi$, as showed in Fig. III.10.c., displays a linear trend with a positive slope.

It is worth noting that the $(111)_{\mathrm{pc}}$ reflection in the MIM geometry can be fitted satisfyingly only in a limited range of tilt angles $\varPsi$, due to the very high orientation of the film along the $(001)_{\mathrm{pc}}$ (Lotgering of 0.96). The trend of the shift is however still very clear.

The strain values were extracted from the linear regression of $d_{(111)}(\varPsi)$ with respect to $\sin^2\varPsi$. In order to do that, we had to approach the Poisson ratio and Young modulus of $PbZrO_3$ by the values found for antiferroelectric ceramics of 95/5 PZT [138]. The exact values of the calculated strains and stress should then be taken with caution, but can still be qualitatively used to compare the samples, as their orientation is comparable.

The in-plane calculated strain (respectively stress) in the MIM geometry is $\varepsilon_{11} = 0.37\ \%$ (respectively $\sigma_{11} =$ 598 MPa). For the IDE geometry, strain (respectively stress) is estimated to $\varepsilon_{11} = 0.20\ \%$ (respectively $\sigma_{11} =$ 325 MPa).

Both films are then in tensile strain, coherently with the fact that both substrates have lower thermal expansion coefficients (TEC) than $PbZrO_3$. Indeed, the TEC of silicon is $2.6 \times 10^{-6}\,\mathrm{K}^{-1}$) while for fused silica, the TEC is $5.5 \times 10^{-7}\,\mathrm{K}^{-1}$. $PbZrO_3$ has a much higher TEC, around $8.0 \times 10^{-6}\,\mathrm{K}^{-1}$ [139]. The difference of TEC between film and substrate for IDE sample is larger than the difference between film and MIM substrate. It then seems incoherent to find that MIM samples undergo a greater tensile strain than the IDE samples. This unexpected difference could be explained by a partial relaxation of the IDE films. This could be due to microcracks which are usually visible in SEM surface imaging but were here not observed. It is still unclear at this stage what is causing this discrepancy of strain and stress with respect to the TEC.

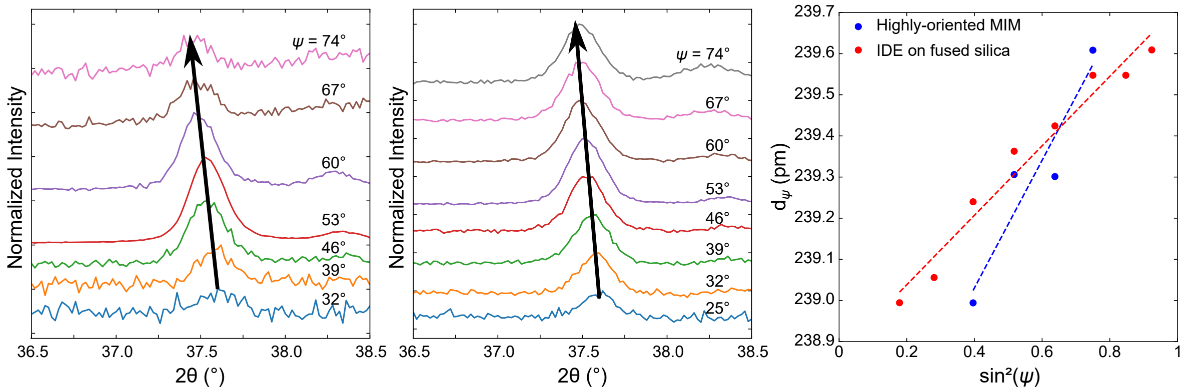

(a) (b) (c)

Figure III.10: $\varPsi$-dependent shift of the $(111)_{\mathrm{pc}}$ reflection for 255 nm-thick $PbZrO_3$ in a (a) highly-oriented MIM or (b) IDE on fused silica samples. (c) Linear regressions of $d_{(111)}(\varPsi)$ with respect to $\sin^2\varPsi$, highlighting a tensile state for both samples.

III.3 Out-of-plane and in-plane antiferroelectric switching

Polarization curves and switching currents have been investigated on films of different thicknesses and different substrates. These have been measured by applying triangular voltages of 100 Hz frequency and of increasing amplitude until the complete and saturated double hysteresis loop is seen.

III.3.a Influence of thickness and orientation on out-of-plane antiferroelectric switching (MIM samples)

Out-of-plane application of an electric field induces a reproducible antiferroelectric switching of the films on MIM samples, as shown in Fig. III.11.

For highly oriented MIM samples, i.e. grown on a 1M-2P-based seed layer, $E_{\mathrm{AFE}\rightarrow\mathrm{FE}}$ and $E_{\mathrm{FE}\rightarrow\mathrm{AFE}}$ are 474 and 256 kV cm^{-1}, extracted from the position of the fitted switching current peaks and averaged for the three sample thicknesses. The higher the thickness, the thinner the switching peaks are. Saturation polarisation P_s range between 22.3 and 25.3 µC cm^{-2}.

For samples grown on a 2-MOE-based $\mathrm{PbTiO_3}$ seed layer, in average $E_{\mathrm{AFE}\rightarrow\mathrm{FE}} = 400$ kV cm^{-1} and $E_{\mathrm{FE}\rightarrow\mathrm{AFE}} = 195$ kV cm^{-1} across all samples represented in Fig. III.11.b. Saturation polarisation P_s range between 27 and 31 µC cm^{-2}.

However, we can see notable differences between samples displaying high or low orientation along $[001]_{\mathrm{pc}}$. Indeed, polarization curves are much squarer and current switching peaks much sharper in highly-oriented $\mathrm{PbZrO_3}$ than they are for lower-oriented samples, as highlighted on Fig. III.11.b. for the 255 nm-thick MIM samples. The current peak width at half-maximum, estimated by a pseudo-Voigt fitting with no particular physical meaning, of the $E_{\mathrm{AFE}\rightarrow\mathrm{FE}}$ peak is around 29 kV cm^{-1} for the highly oriented MIM samples and around 95 kV cm^{-1} for the lower oriented ones.

III.3.b Measurement of permittivity ε & Curie temperature T_c in MIM samples

The evolution of the polarisation and current curves as well as the value of the dielectric constant of an 85 nm-thick highly-oriented MIM sample was studied as shown on Fig. III.12. To obtain this data, polarisation curves and capacitance measurements around 0 V were measured between 25 and 260 °C at 5 kHz, to prevent as much as possible the leakage due to thermal effects. The displayed measurements are the concatenated results of 3 different measurements of successive voltage ranges. Indeed, the electrodes of those samples were rarely resisting the

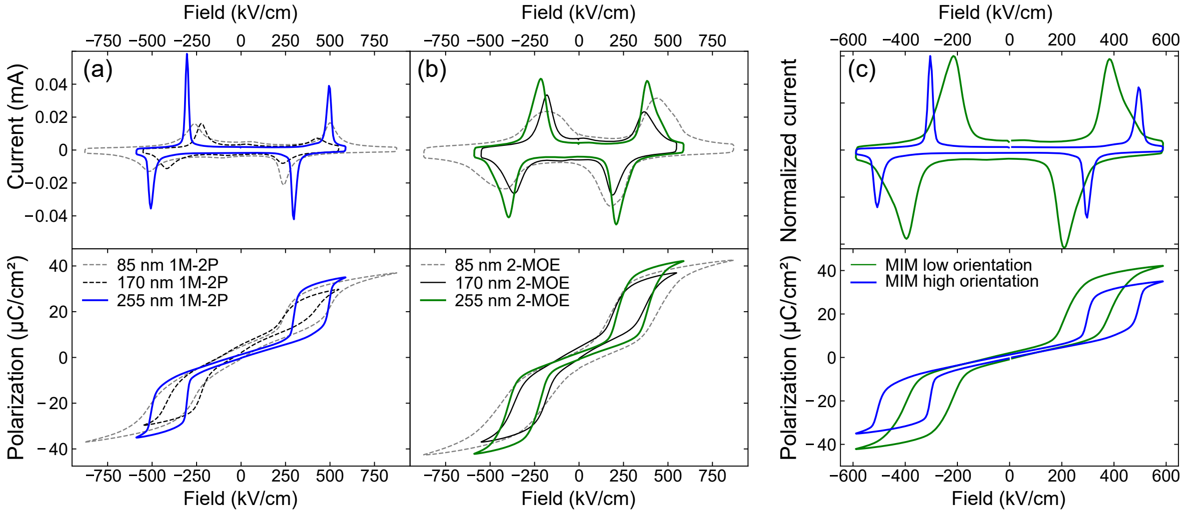

Figure III.11: Current and polarization curves of (a) highly-oriented and (b) lower-oriented PbZrO$_3$ films grown on platinised silicon substrates, i.e. in a MIM sample geometry. (c) displays a comparison between high- and low-orientation 255 nm-thick MIM samples.

sustained capacitance measurements or the aixACCT tips were often losing the contact to the electrodes.

Polarisation and current curves display a decrease in both $E_{\mathrm{AFE}\to\mathrm{FE}}$ and $E_{\mathrm{FE}\to\mathrm{AFE}}$ until around 230 °C where both P-E and I-E curves display more of a ferroelectric or leaky paraelectric behaviour. Indeed, the intensity of the current value of back-switching $E_{\mathrm{FE}\to\mathrm{AFE}}$ peak becomes low enough to be superimposed to the background.

We performed a mathematical fitting, i.e. without physical meaning, of the current peaks by pseudo-Voigt line-shapes at every measured temperature to follow the temperature evolution of the critical fields. Above 210 °C, the critical field $E_{\mathrm{FE}\to\mathrm{AFE}}$ cannot be fitted anymore and the current curves then display a single switching peak below 200 kV cm^{-1}.

The permittivity shows an increase typical of an antiferroelectric, from a value of 231 at 25 °C to a maximum value of 608 at 245 °C, increasing by 163 %. A dielectric anomaly is visible around 245 °C = 518 K, which gives an estimated Curie temperature of our films T_c. This value is slightly higher than the bulk T_c value of 505 K [23].

The single switching peak observed between 210 and 260 °C could be explained either by the increase with temperature of leakage as it can create a higher background than the height of the switching peak linked to $E_{\mathrm{FE}\to\mathrm{AFE}}$ or by an intermediate ferroelectric phase in between the antiferroelectric and paraelectric phases. However, the permittivity measurements hint at the former interpretation of high leakage, as a single dielectric anomaly is visible and around $T = 245$ °C.

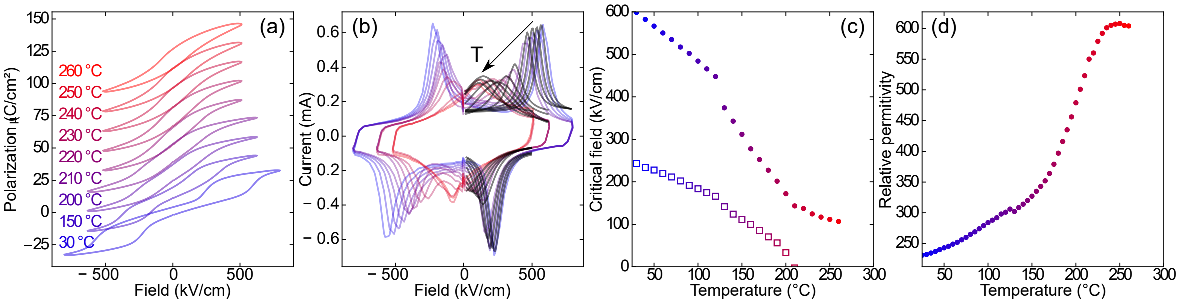

Figure III.12: (a) Polarisation curves and (b) switching current at selected temperatures. (c) shows the evolution of the critical field through the temperature range. (d) Evolution of the permittivity between 25 and 260 °C. Measurements performed on a highly-oriented 85 nm-thick MIM $PbZrO_3$ sample.

III.3.c Effect of frequency on $E_{\mathrm{AFE}\to\mathrm{FE}}$, $E_{\mathrm{FE}\to\mathrm{AFE}}$ in MIM samples

The effect of the measurement frequency on the critical fields $E_{\mathrm{AFE}\to\mathrm{FE}}$ and $E_{\mathrm{FE}\to\mathrm{AFE}}$ has been studied in a range of 10 Hz to 5 kHz for a 255 nm-thick highly-oriented MIM sample. The variation around the average measured value of $E_{\mathrm{AFE}\to\mathrm{FE}}$ and $E_{\mathrm{FE}\to\mathrm{AFE}}$ is around 5.5 %.

We can conclude that the variation of critical fields for MIM samples of different thicknesses at a given frequency is around the same order of magnitude than the variation of critical fields with respect to the measurement frequency.

III.3.d Isotropy of the permittivity ε measured in MIM samples

We performed permittivity measurements with respect to measurement frequency in 255 nm-thick MIM samples with higher and lower film orientation, as shown in Fig. III.14. $PbZrO_3$ is an anisotropic material and the permittivity should then be higher in the direction of the "electric dipoles", which are, in $PbZrO_3$, mostly due to antiparallel lead displacements. These displacements are along the [110] pseudo-cubic direction. From the Lotgering factor of 0.96, we know that the film with a higher orientation is very well oriented along the [001] direction, meaning that the antiparallel lead displacements are generally in the plane of the film. In the MIM sample with a low orientation, the Lotgering factor is around 0.4 meaning that there are more randomly oriented grains than in the other sample. This also means that there is bigger portion of lead displacements which are out-of-plane and then can contribute to the permittivity measured out-of-plane. We would then expect the "MIM low orientation" sample to display a higher permittivity than the "MIM high orientation" one.

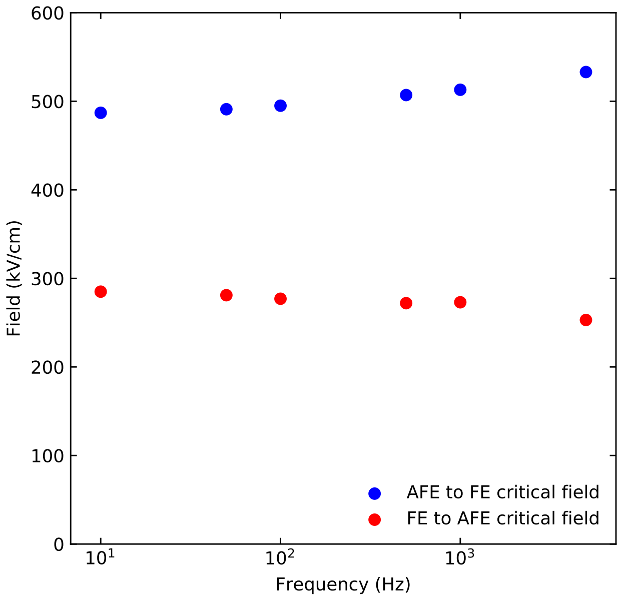

Figure III.13: Critical fields $E_{\mathrm{AFE}\to\mathrm{FE}}$ and $E_{\mathrm{FE}\to\mathrm{AFE}}$ of highly-oriented $PbZrO_3$ MIM films with respect to measurement frequency.

This is however not the case: the average permittivity is 210 for low-oriented and 218 for highly-oriented MIM samples with barely any variation over the frequency range studied. We then conclude that there is no strong anisotropy of the permittivity in our films.

It is worth noting that the bulk value of the permittivity of $PbZrO_3$ is around 120 [140]. Refs. [125, 141] found permittivity values around 400 for sputtered films.

III.3.e Influence of thickness on the in-plane antiferroelectric switching (IDE samples)

Antiferroelectric switching is also achieved for $PbZrO_3$ samples with interdigitated electrodes (IDE). The polarisation curves at different thicknesses for IDE samples grown on fused silica are represented on Fig. III.15.a. The measured critical fields $E_{\mathrm{AFE}\to\mathrm{FE}}$ and $E_{\mathrm{FE}\to\mathrm{AFE}}$ are respectively in average 279 kV cm^{-1} and 133 kV cm^{-1} across the three thicknesses. The polarisation P_s however clearly varies across the studied samples, with no obvious correlation with the thickness of the films. Indeed, P_s reaches a maximum for the intermediate thickness of 170 nm and P_s is minimum for the thickest (255 nm) sample. The reason for that strong variation of polarisation is not currently known.

We also deposited thicker samples on fused silica and sapphire in an IDE geometry to study the

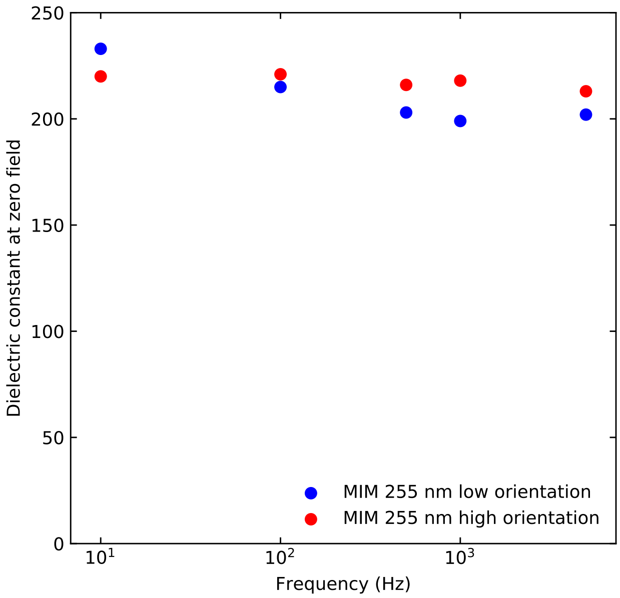

Figure III.14: Dielectric permittivity as a function of measurement frequency on 255 nm-thick low- (blue) and highly-oriented (red) MIM samples.

physical properties of the films across the field-induced phase transition. Both of these samples are 850 nm-thick and display a clear antiferroelectric switching. $E_{\mathrm{AFE}\to\mathrm{FE}}$ and $E_{\mathrm{FE}\to\mathrm{AFE}}$ are respectively 424 and 271 kV cm^{-1} for fused silica and 383 and 250 kV cm^{-1} for c-sapphire IDE. The measured P_s are respectively 17 and 28 µC cm^{-2}.

In the current characteristics of IDE films grown on either substrates, there is a clear peak present around at low electric fields, around 50 kV cm^{-1}. It is also present in a less pronounced fashion in MIM samples. This anomalous current peak intensity seems to increase with the $PbZrO_3$ thickness, as shown on Fig. III.15, and is accompanied by a small bulge around zero field, particularly visible on the c-sapphire polarisation curve. This gives a "triple loop" shape to the polarisation curves.

The existence of this peak could then be due to a potential ferroelectric contribution or to the presence of the ferroelectric $PbTiO_3$ seed layer below the $PbZrO_3$ film. Structural studies [25, 142–144] have raised evidence of polar lead displacements and other "triple hysteresis loops" have also been measured [145] from $PbZrO_3$ films. We will not conclude on the origin of this peak contribution.

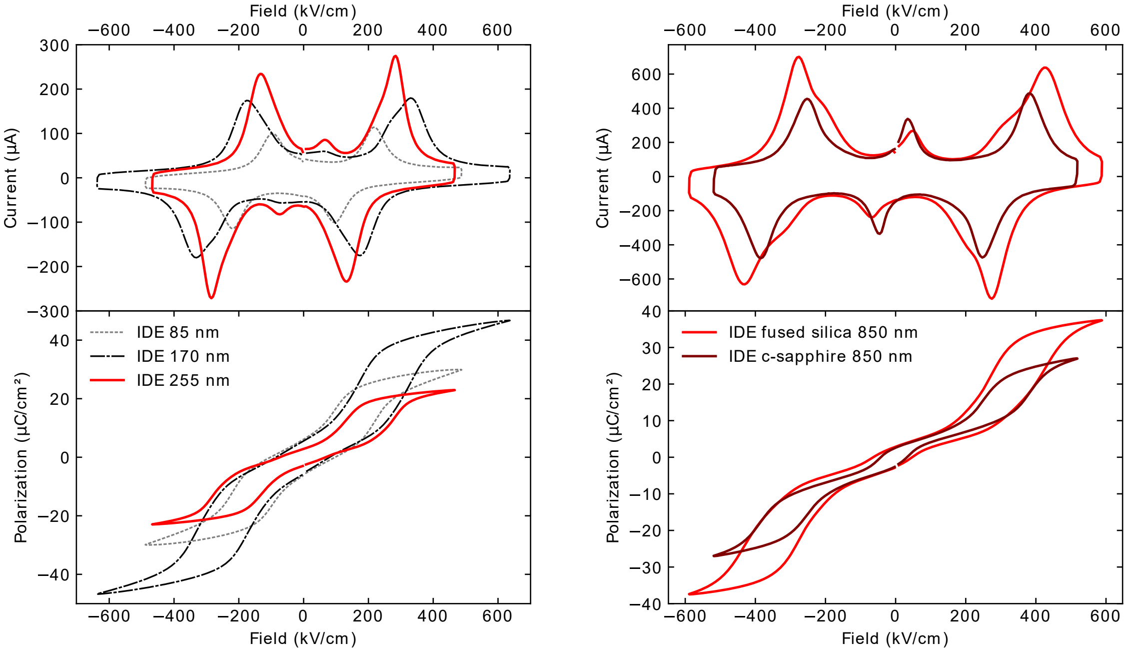

(a) (b)

Figure III.15: Current and polarization curves of $PbZrO_3$ films (a) deposited on fused silica at three different thicknesses and (b) 850 nm-thick films on fused silica and c-sapphire.

III.3.f Optical observation of the in-plane antiferroelectric switching in IDE samples

Both antiferroelectric and polar phase in $PbZrO_3$ are anisotropic, see Ref. [28], meaning that there is birefringence in both phases. However, antiferroelectric switching will change the symmetry of the material and hence the birefringence value. We qualitatively measured this difference of birefringence between the two phases by a simple electro-optic setup represented on Fig. III.16.

A polarised light Leica microscope is used as the basis for this setup. White light comes from the bottom source, then passes through the first polariser, collected by an objective and another polariser called the analyser. The resulting light is then collected on a CCD camera and acquired through Leica's proprietary software. Without a sample, when the two polarisers are parallel, the intensity is maximum, and when they are crossed, the intensity is zero. When any oriented birefringent single crystal is placed between two crossed polarisers, the maximum of light passing through it is when the extraordinary axis is oriented at $\pi/4$ in the plane of the polarisers.

These preliminary measurements consist then in putting our $PbZrO_3$ sample in between of the crossed polarisers with an angle between polarisers and electrodes of $\pi/4$ and then applying a dc electric field of a value superior to $E_{\mathrm{AFE}\rightarrow\mathrm{FE}}$, thanks to a Keithley 2410. Images are taken with and without field and shown on Fig. III.17. Exposure, brightness and colour temperature were

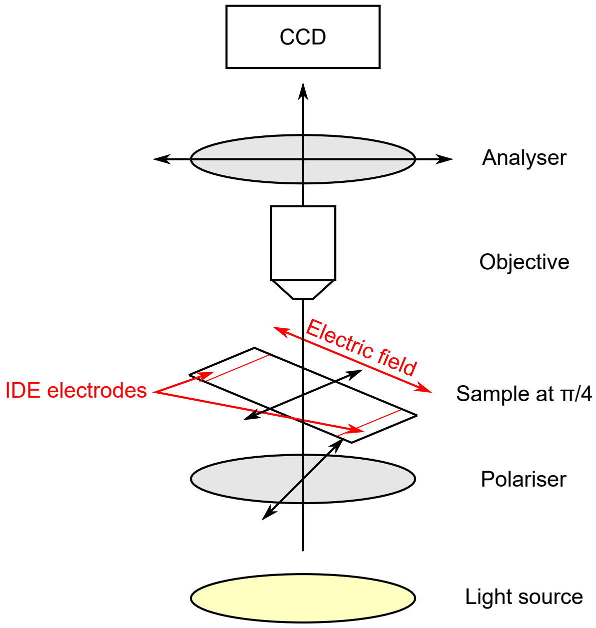

Figure III.16: Schematic birefringence setup using a polarised light microscope. Not in scale.

maintained constant between image acquisition. The sample used here is an IDE sample grown on fused silica and of thickness around 850 nm.

On Fig. III.17.a., no field is applied on the $PbZrO_3$ film and the two polarisers are crossed: there is then almost extinction of the light. Indeed, due to the intrinsic strain, the sample is slightly birefringent and some light still passes through the crossed polarisers. When the field is applied above the $E_{\mathrm{AFE}\rightarrow\mathrm{FE}}$ of the film, we observe a clear contrast between the switched film in between the interdigitated electrodes and the unswitched film. This measurement is only qualitative and should be taken a few steps further but highlight the interest of synthesising electrically switchable $PbZrO_3$ on transparent substrates.

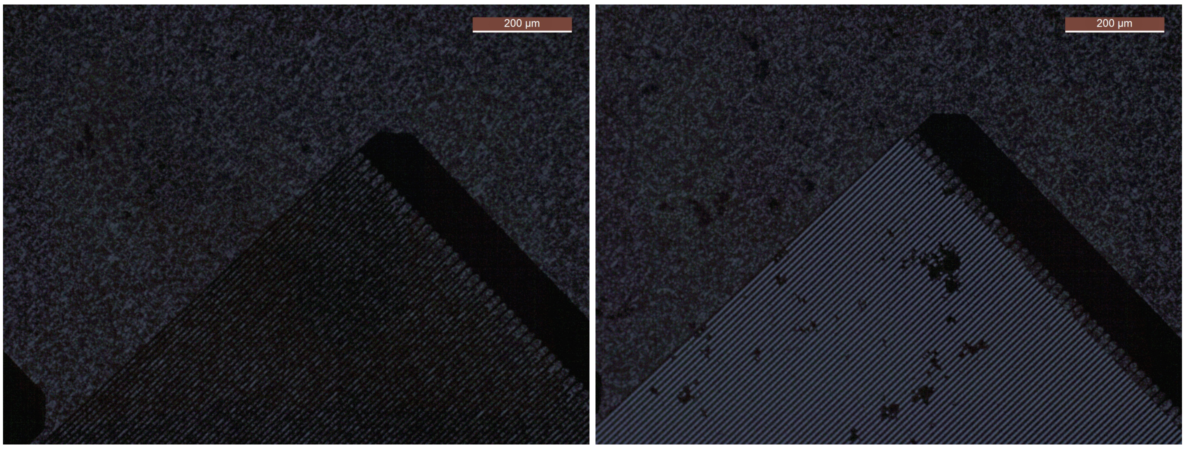

(a) (b)

Figure III.17: Microscope image of (a) a non-switched and (b) a dc-switched $PbZrO_3$ thin film placed between two polarisers at extinction. Brightness was increased on both pictures by 25 % in post-processing to highlight the electrically-induced birefringence.

III.4 Importance of film orientation on critical field $E_{\mathrm{AFE}\to\mathrm{FE}}$

III.4.a Antiferroelectric switching difference between MIM and IDE samples

Fig. III.18 shows the comparison between a 255 nm-thick highly-oriented $PbZrO_3$ film in MIM geometry and a $PbZrO_3$ film of same thickness grown on a fused silica and topped with IDE.

We observe two main differences between MIM and IDE geometries. Firstly, the switching peaks are much sharper in the MIM geometry (width at half-maximum $\approx$ 30 kV cm^{-1}) than with IDE (width $\approx$ 100 kV cm^{-1}). Secondly, there is an observable diffrence of the current peak position associated to the antiferroelectric switching in the IDE geometry compared to MIM samples, leading to a lowering of the critical fields $E_{\mathrm{AFE}\to\mathrm{FE}}$ and $E_{\mathrm{FE}\to\mathrm{AFE}}$.

III.4.b Simple model of antiferroelectric switching

To explain the observed difference in antiferroelectric switching, we formulated a simple thought experiment/toy model based on the film orientation and the direction of the applied electric field.

First, we assume that the stabilised polar phase under electric field would be the same for any direction of the applied electric field and of rhombohedral geometry. Such a polar rhombohedral phase is often considered for $PbZrO_3$, see section III.1. The polarisation in this polar phase is then oriented along the $(111)_{\mathrm{pseudo-cubic}}$ direction.

E_0 is the minimum field needed to switch the film to the polar phase. This value is only reached if the field is actually applied along the $(111)_{\mathrm{pseudo-cubic}}$ direction. For any other direction of the applied field with an angle θ with the closest $(111)_{\mathrm{pseudo-cubic}}$ direction, we assume that the

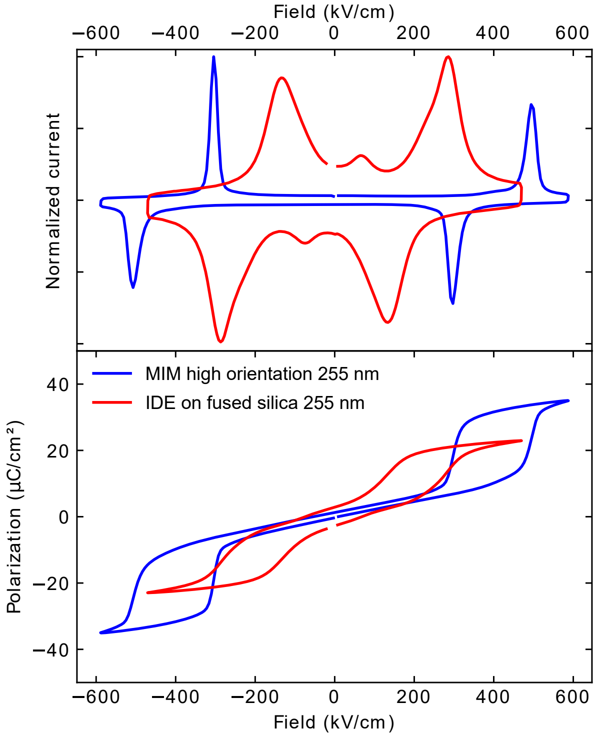

Figure III.18: Current and polarization of 255 nm films in highly-oriented MIM and IDE on fused silica configurations.

threshold value needed for the switching is $E_{\mathrm{FE}\rightarrow\mathrm{AFE}} = E_0/\cos\theta$.

Following these assumptions, we can then calculate E_θ in both MIM and geometries. It should be reminded that without any field, our films are mostly oriented along the $(001)_{\mathrm{pc}}$ direction for both highly-oriented MIM and IDE samples, according to our x-ray diffraction measurements. In-plane, every film is oriented isotropically, as shown in our pole figures measurements and represented on Fig. III.19.a.

In MIM geometry (Fig. III.19.b.), the field is applied along $(001)_{\mathrm{pc}}$. For any in-plane orientation of the unit cell, there is a single value of the angle θ between the applied field and the $(111)_{\mathrm{pc}}$. The calculated critical field E_θ is then $E_{\mathrm{AFE}\rightarrow\mathrm{FE}} \approx 1.73\ E_0$, as $\cos\theta = 1/\sqrt{3}$.

For films with IDE (Fig. III.19.c.), the situation is a bit more complex. Indeed, the field is applied in-plane and the isotropic in-plane lead to a range of θ angles between field and closest $(111)_{\mathrm{pc}}$ direction, as each grain can take any in-plane orientation. To simplify the problem, we consider the two extreme situations leading to the highest and lowest values of θ. Firstly, when the applied field is oriented along the $(110)_{\mathrm{pc}}$ direction of a specific grain, we get $\cos\theta = \sqrt{6}/3$ leading to a critical field value of $E^{\mathrm{min}}_{\mathrm{AFE}\rightarrow\mathrm{FE}} \approx 1.22\ E_0$. This situation is represented by the blue scheme on Fig. III.19.c. Now, when the applied field is oriented along either the $(100)_{\mathrm{pc}}$ or the $(010)_{\mathrm{pc}}$ direction of the grain, we find $\cos\theta = 1/\sqrt{3}$ leading to $E^{\mathrm{max}}_{\mathrm{AFE}\rightarrow\mathrm{FE}} \approx 1.73\ E_0$, shown in green on Fig. III.19.c.

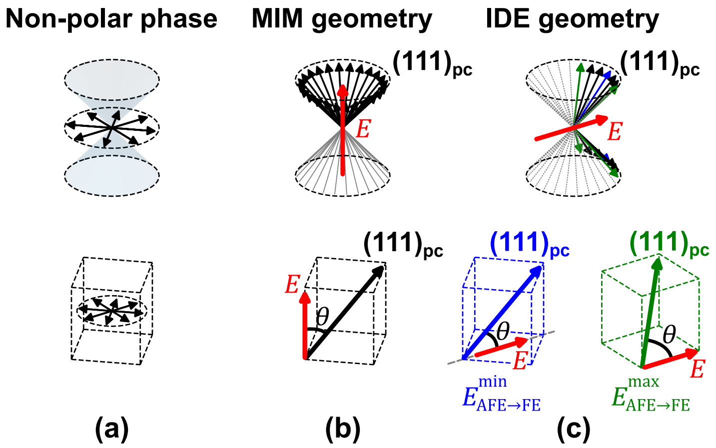

Figure III.19: Schematic representation of $PbZrO_3$ polycrystalline films in (a) a non-polar antiferroelectric phase, (b) an out-of-plane switched polar phase and (c) an in-plane switched polar. The top row represents the direction of the schematic electric dipoles in each case, while the bottom represent specific unit cells. Films are assumed to be perfectly $(002)_o$-oriented and the polar phase is assumed to be rhombohedral.

III.4.c Comparison with our measurements

This simple thought experiment allow is us to qualitatively explain the difference of switching between MIM and IDE orientation.

Indeed in MIM, a single value of critical is found, explaining the sharp measured switching peaks and hysteresis. The broader switching peaks can then be explained by the isotropic in-plane which leads to a different angle between applied field and in-plane axes for each grain of the film, hence a large range of critical fields.

The higher value of $E_{\mathrm{AFE}\to\mathrm{FE}}$ in MIM samples compared to the IDE geometry can also be explained, as the $E_{\mathrm{AFE}\to\mathrm{FE}}$ calculated by this model should be around $1.73\ E_0$ in MIM while the IDE film will already start switching when the applied field is of $1.23\ E_0$. However, this agreement is only qualitative, as the measured $E_{\mathrm{AFE}\to\mathrm{FE}}$ values do not agree with these simple calculations.

III.4.d Other factors potentially influencing $E_{\mathrm{AFE}\to\mathrm{FE}}$

While we think that the distribution of critical fields seen in the literature is principally explained by the film orientation, there are many other factors that can help widening the distribution.

First, the grain size can have a strong effect on the threshold electric field necessary to switch the film to a polar phase. Indeed, the smaller the grains, the more grain boundaries are present. In ferroelectrics, these grain boundaries can act in two opposite ways. Either boundaries effectively increase $E_{\mathrm{AFE}\to\mathrm{FE}}$ due to a potential drop at the boundaries [146] or they can decrease $E_{\mathrm{AFE}\to\mathrm{FE}}$ as they can act as nucleation points [147] hence facilitating the phase transition. However, our SEM micrographs show little variation of grain size across the samples and in a range that, according to Ref. [148, 149], plays only a minor role in the variation of critical fields. It is worth noting though that due to the columnar nature of our films, the number of grain boundaries traversed by the electric field is much greater for IDE (in-plane field) samples compared with MIM. As the critical field $E_{\mathrm{AFE}\to\mathrm{FE}}$ in the IDE geometry is much smaller than in MIM, we could assume that the columnar growth of the film helps the antiferroelectric switching, possibly due to the previous hypothesis of grain boundaries helping nucleation.

The strain difference between our films is due to different substrates, hence different thermal expansion coefficients (TEC), and could also shift the critical field $E_{\mathrm{AFE}\to\mathrm{FE}}$. In Ref. [150], samples have been processed on either $\mathrm{SiO_2/Si}$ or $\mathrm{SrTiO_3}$ substrates which lead respectively to either a tensile or a compressive stressed film. The authors conclude that a tensile state lead to an increase in $E_{\mathrm{AFE}\to\mathrm{FE}}$ while compression decreases $E_{\mathrm{AFE}\to\mathrm{FE}}$. This interpretation however does not help clarify why in our case of only tensile stressed films, we see such a decrease in $E_{\mathrm{AFE}\to\mathrm{FE}}$ in the IDE geometry. Also, according to [151], in CSD PZT with 5 % of Ti, a layer-by-layer deposition increases the residual tensile stress in films smaller than 0.5 µm, comparatively to depositing several layers at a time. The authors see that this increase of stress is accompanied by an increase of $E_{\mathrm{AFE}\to\mathrm{FE}}$, which is coherent with our results. However, the authors also recognise that the orientation of their lower-stressed films is quite random, making it difficult to untangle the two parameters. It is also important to note that they see a difference of less than 70 kV cm^{-1} for films of similar thicknesses, with respect to the average difference of around 200 kV cm^{-1} that we found between our MIM and IDE samples, which then cannot be entirely explained by the effect of strain in our samples.

In Ref. [125], the authors have measured the permittivity at 1 kHz of two samples on different substrates: the first one is strongly oriented along the [001] pseudo-cubic direction and the other one is randomly oriented. Both films display a permittivity value of 400(10). This value seems however uncorrelated to the switching properties of the film as the (001)-oriented film displays a ferroelectric behaviour and the randomly-oriented sample shows antiferroelectric switching. This is confirmed by our own measurements of permittivity on low and highly-oriented MIM samples, which display very different values of $E_{\mathrm{AFE}\to\mathrm{FE}}$ but little to no change of permittivity in between these different samples, see Fig. III.14. This shows that the difference in critical fields cannot be simply explained by a potential anisotropy in permittivity.

III.4.e Comparison with litterature

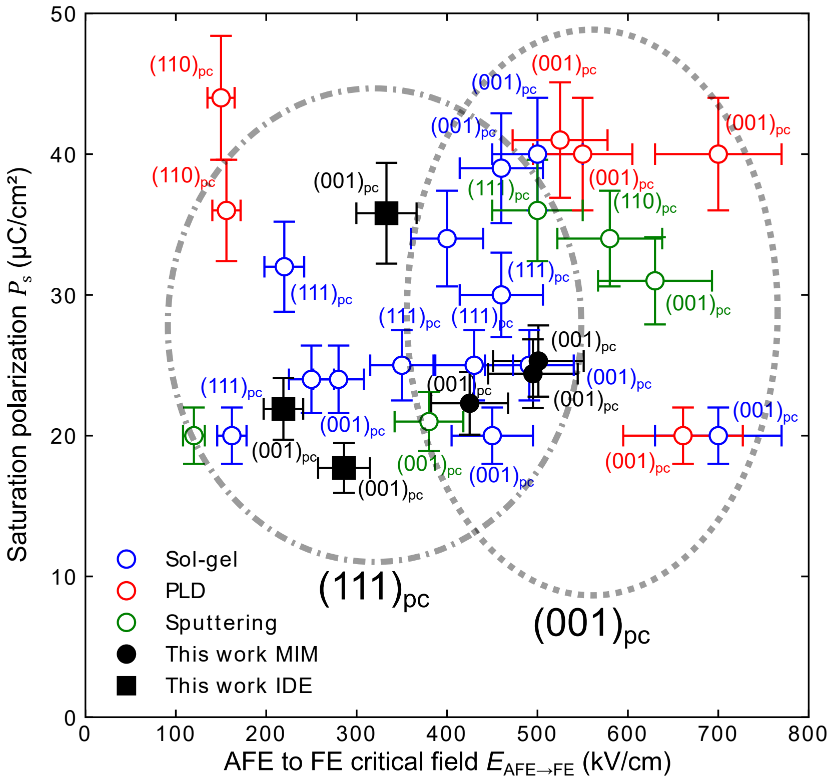

Figure III.20: Comparison of critical fields $E_{\mathrm{AFE}\rightarrow\mathrm{FE}}$ and saturation polarization P_s from literature with our own data. Orientations have been added to highlight the relevance of this parameter on the $E_{\mathrm{AFE}\rightarrow\mathrm{FE}}$ and P_s. Circle indicate the general tendencies observed.

We now present on Fig. III.20 a completed literature review that we first showed in I.1. Our previously presented samples were also added to this graph. A special care was put into adding the orientation of each film for which this information was available, or for which x-ray diffraction patterns were reported. This is however only indicative as, more often than not, no clear quantitative information such as Lotgering factors was available.

However, even with that factor in mind, two groups of samples can easily be seen: one at lower values of $E_{\mathrm{AFE}\rightarrow\mathrm{FE}}$ is mostly composed by $(111)_{\mathrm{pc}}$-oriented samples and the other one at higher $E_{\mathrm{AFE}\rightarrow\mathrm{FE}}$ comprising mostly of $(100)_{\mathrm{pc}}$.

These tendencies are coherent with our simple switching model, as it says that switching to a rhombohedral polar phase should require less electrical energy for a film-oriented along $(111)_{\mathrm{pc}}$ than for a $(100)_{\mathrm{pc}}$ film.

Once again however, the agreement is only qualitative as exact values do not match the $E_{\mathrm{AFE}\rightarrow\mathrm{FE}}$ values predicted by our model.

It is however worth noting that our model tends to validate the assumption of a rhombohedral polar phase. Indeed, a tetragonal phase for instance would display a very different distribution of $E_{\mathrm{AFE}\to\mathrm{FE}}$ than the one observed in Fig. III.3, as the $(100)_{\mathrm{pc}}$ would then occupy the lowest range of the critical fields.

While the critical field $E_{\mathrm{AFE}\to\mathrm{FE}}$ distribution seems to explained principally by the film orientation, the saturation polarisation P_s does not seem to be linked to this parameter. A possible explanation could be that any parasitic current that is not linked to the displacement current can contribute to the polarisation value, regardless of the intrinsic change of polarisation in $\mathrm{PbZrO_3}$. The apparent uncorrelation between P_s of film orientation is quite unlike ferroelectric materials, where the direction for which the coercive critical field is minimum is also the direction displaying the highest polarisation.

III.5 Conclusions and next steps

III.5.a Results summary

In this work, we first presented the synthesis of lead zirconate $PbZrO_3$ thin films processed on platinised silicon and transparent fused silica and sapphire substrates. Films grown on silicon could be switched successfully by applying an out-of-plane electrical field. More remarkably, we switched our films processed on fused silica and sapphire substrates by applying an in-plane electric field, in one of the first realisations of in-plane switching of lead zirconate. Thanks to the transparency of our substrates, we were also able to observe the in-plane switching optically through a change of birefringence.

We observed a clear difference in the critical fields of films switched in the two different geometries, with out-of-plane switching happening at much higher fields compared to in-plane switching. We then proposed and discussed a simple model of switching to explain this difference. This model assumes a perfect film orientation and is found to be coherent only assuming that the polar phase of $PbZrO_3$ is rhombohedral. The validity of our simple model of switching is also reaffirmed by a qualitative agreement with our review of literature data.

III.5.b Follow-up studies

Processing fully comparable samples grown on different substrates can prove to be quite difficult. Trying to process films in the two different switching geometries but on a single type of substrate could potentially help removing a few of the factors limiting the scope of the comparison, such as the difference in strain state, for instance. Another interest in terms of processing could be to try to tune the film orientation using different seed layers. This could be helpful to confirm the validity of our discussion on the strong influence of the film orientation on the critical fields but also to find the optimal film orientation to obtain the lowest switching fields.

Next steps could also be taken to draw on our transparent films topped with interdigitated electrodes. For instance, we could measure quantitatively the change of birefringence during the in-plane switching or we could also directly probe the polar phase through micro-spectroscopy or micro-scattering techniques. On a more applicative side, we could, for instance, estimate the adiabatic temperature change due to electrocaloric effect in our films.

Contributions

Thank you N. Godard, S. Glinšek and E. Defay for the development of seed layers which allowed us to compare samples in different switching geometries. Many thanks to S. Girod for the deposition of high-quality MIM and IDE electrodes. Thanks for your help Y. Fleming for the pole figure measurements and thank you B. El Adib and N. Valle for the SIMS measurements. I would also like to thank all of my colleagues who prepared solutions for me: S. Glinšek, V. Kovacova, A. Blazquez-Martinez, L. Song or formerly N. Godard. Thanks M. Guennou for leading this study.

This work was published in Applied Physics Letters in 2021, cf. Ref. [36].

Chapter IV

Francisite $Cu_3Bi(SeO_3)_2O_2Cl$: a potential Kittel antiferroelectric crystal

Kittel's model is still currently considered as the most consensual definition of antiferroelectricity in the community, yet, it lacks of a model material showing clearly defined sublattices of opposite polarisation. In that chapter, we will present and propose francisite $Cu_3Bi(SeO_3)_2O_2Cl$ as being the closest realisation, to our knowledge, of a uni-dimensional displacive Kittel antiferroelectric.

First, we will review the structure of the francisite $Cu_3Bi(SeO_3)_2O_2Cl$ before presenting its phase transition as well as the other existing francisites. $Cu_3Bi(SeO_3)_2O_2Cl$ undergoes a phase transition at $T_c = 115\,\mathrm{K}$ which has been studied through dielectric, Raman and infrared spectroscopy measurements as well as investigated through density functional theory.

In this work, Raman measurements as well as inelastic x-ray scattering and thermal diffuse scattering experiments were performed to follow the softening of the mode driving the phase transition. These measurements are presented and interpreted to shine light on the type and dynamics of the phase transition. Our attempt at switching $Cu_3Bi(SeO_3)_2O_2Cl$ to its polar phase is highlighted.

Lastly, the two remaining experimental and theoretical questions, i.e. the ability to switch to the polar phase of francisite and the apparent unability of DFT to predict the displacive character of the material, will be detailled.

IV.1 Review of phase transitions in francisite $Cu_3Bi(SeO_3)_2O_2Cl$

Francisite $Cu_3Bi(SeO_3)_2O_2Cl$ is a bright green adamantine mineral that was first retrieved by Glyn L. Francis in 1987 from the mine of Iron Monarch, South Australia (see Fig. IV.1). It was first characterised in Ref. [152], was later in the year named after its finder and approved by the International Mineralogical Association as being a new mineral. Since its discovery, a variety of francisites have been studied and synthesised, as we will see later on in I.1.a.

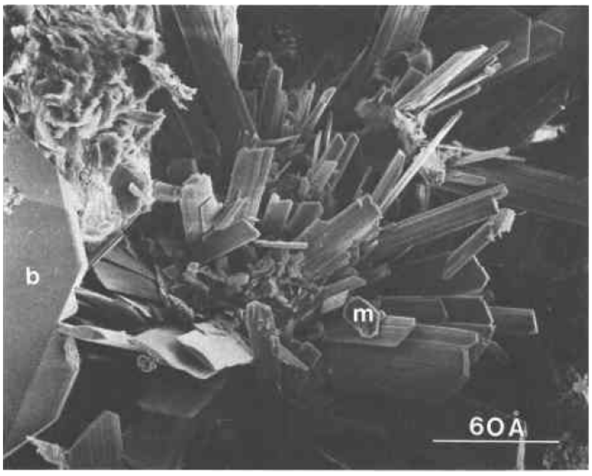

Figure IV.1: SEM micrograph of a francisite mineral. Label (b) indicates barite and (m) muscovite minerals. Adapted from [152].

IV.1.a Crystallographic structure of the francisite family

In its room temperature phase, francisite $Cu_3Bi(SeO_3)_2O_2Cl$ crystallises in an orthorhombic $Pmmn$ space group. At room temperature, the lattice parameters have been determined in Ref. [153] to be $a = 6.354$ Å, $b = 9.635$ Å and $c = 7.233$ Å. It can be described as two layers of hexagonal copper oxide forming a Kagome lattice in the ab-plane and separated vertically, i.e. along the c-axis, by Bi, Cl and SeO_3, as shown in Fig. IV.2.a.

A wide range of francisites can be obtained by chemically substituting certain atoms compared to the standard $Cu_3Bi(SeO_3)_2O_2Cl$. For instance, bismuth Bi by yttrium Y or rare-earths, selenium Se by tellurium Te or even chlorine Cl by other halogens such as bromine Br or iodine I.

Bromine francisite $Cu_3Bi(SeO_3)_2O_2\mathbf{Br}$ is in an orthorhombic $Pmmn$ phase at room temperature and below, see Ref. [69, 155]. Yttrium Y and rare-earth francisites do not have a different room temperature phase than the standard $Pmmn$ phase similar to $Cu_3Bi(SeO_3)_2O_2Cl$ [156–158]. However, it can be noted that there is a linear relation between the radius of the rare-earth ion and the volume of the unit cell [156].

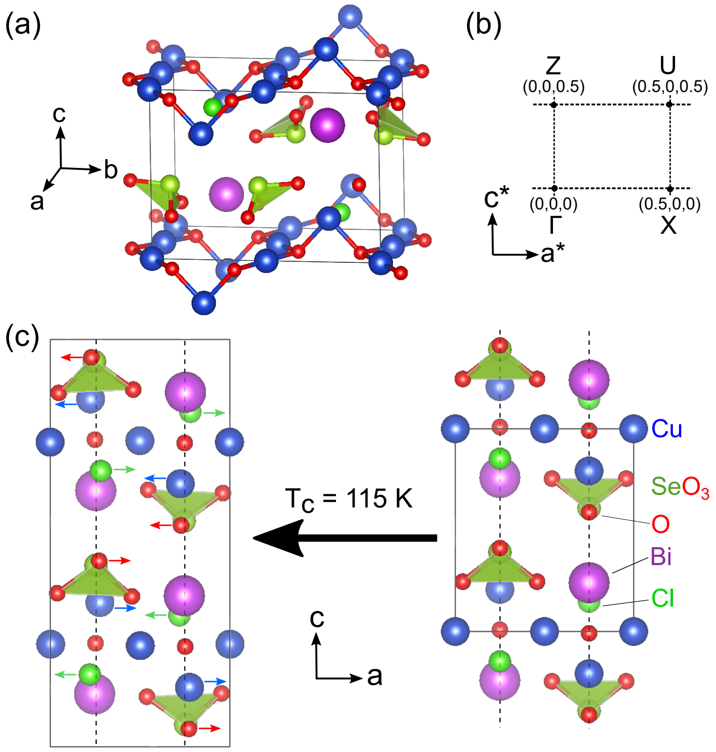

Figure IV.2: (a) Room temperature structure of francisite $Cu_3Bi(SeO_3)_2O_2Cl$. (b) Representation of the Brillouin zone with zone-boundary point labels according to Ref. [154]. (c) Francisite structure in the ab-plane, displaying antiparallel displacements at the phase transition and a doubling of the unit cell along the c-axis. Adapted from [70].

Most notably, $Cu_3Bi(\mathbf{Te}O_3)_2O_2Cl$ is reported to reach a $Pcmn$ phase at room temperature [159]. This effect could be explained geometrically by the higher constraints on the Cl ions due to the bigger ionic radius of ellurium Te (210 pm) compared to selenium Se (190 pm) along the c-axis, which might then be forced to move along a in an antiparallel fashion to minimise the coulombic interaction.

IV.1.b Below 25 K: magnetic ordering in francisites

In the ab-plane, francisites present a pseudo-kagome lattice. This kind of structure is often responsible for the apparition of non-colinear spin orders or magnetic orders due to the geometrical frustration it imposes. This is also the case in francisite $Cu_3Bi(SeO_3)_2O_2Cl$, as a next-nearest-neighbour antiferromagnetic ordering appears below $T_N = 25$ K [69, 152, 153, 160–162].

In $Cu_3Bi(SeO_3)_2O_2Br$, a magnetic ordering also appear at a critical temperature close to the Néel temperature $T_N \approx 25$ K of $Cu_3Bi(SeO_3)_2O_2Cl$.

IV.1.c A structural phase transition at 115 K in $Cu_3Bi(SeO_3)_2O_2Cl$

Under $T_c = 115$ K, $Cu_3Bi(SeO_3)_2O_2Cl$ displays an antiparallel motion of Cl and Cu along the a-axis and a doubling of the unit cell along c. This phase transition has been resolved by neutron diffraction experiments and corresponds to the symmetry lowering from an orthorhombic $Pmmn$ phase to an orthorhhombic $Pcmn$ phase [69]. In terms of symmetry, a mirror plane of $Pmmn$ is replaced below T_c by a glide plane along a single crystal axis. The lattice parameters of the $Pcmn$ phase at 50 K have been refined and found to be: $a = 6.340\,80$ Å, $b = 9.629\,30$ Å and $c = 14.418\,40$ Å [69]. There is then only a small thermal dilatation along a and b, while c is doubled.

In Ref. [160], the authors have measured the infrared reflectance spectra of $Cu_3Bi(SeO_3)_2O_2Cl$ along the three axes (a, b and c) with respect to the sample temperature, as shown in Fig. IV.3. The emergence of 16 new modes below $T_c = 115$ K shows the presence of the phase transition, even if their x-ray diffraction studies did not confirm it at the time.

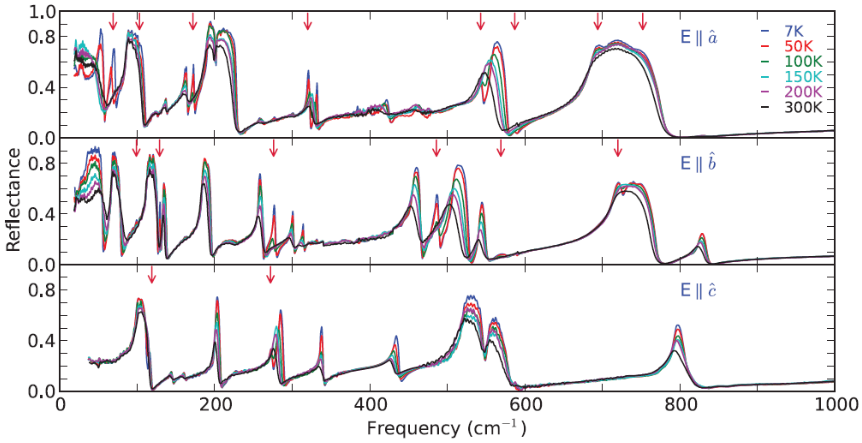

Figure IV.3: Reflectance spectra of $Cu_3Bi(SeO_3)_2O_2Cl$ at several temperatures. The arrows indicate the position of the modes appearing only below $T_c = 115$ K. Adapted from [160].

This is confirmed by the few Raman spectroscopy studies that have been performed on francisites [155, 160, 163]. In Ref. [155] and its preprint version [163], parallel and crossed polarisation Raman spectra are taken for both $Cu_3Bi(SeO_3)_2O_2Cl$ and $Cu_3Bi(SeO_3)_2O_2Br$ at room temperature. The number of modes visible in the spectra is coherent with the expected number of A_g and B_{1g} modes expected by group theory analysis. A complete temperature study of both francisites is then done in a range from 9 to 295 K.

In $Cu_3Bi(SeO_3)_2O_2Cl$ and below 115 K, a number of new modes emerge at the phase transition. Remarkably, the authors of Ref. [163] describe the softening of single mode below T_c. That evolution is represented in Fig. IV.4, and the trend describing the temperature-dependency of the mode frequency is a square-root law. In Ref. [155], the authors already call that phase "antiferroelectric" without linking this soft-mode to the driving mechanism of the paraelectric to antiferroelectric phase transition in $Cu_3Bi(SeO_3)_2O_2Cl$.

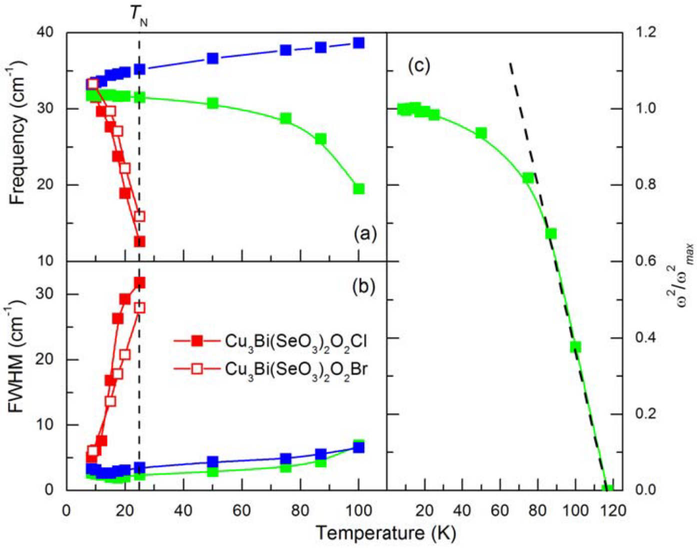

Figure IV.4: Low-temperature study of low frequency modes in francisites $Cu_3Bi(SeO_3)_2O_2Cl$ and $Cu_3Bi(SeO_3)_2O_2Br$. (a) Displays the change in frequency and (b) in peak width. (c) Frequency evolution of the soft-mode seen only in $Cu_3Bi(SeO_3)_2O_2Cl$, highlighting a square-root law over a very limited temperature range.

In Ref. [69], the authors have performed dielectric measurements on single crystals and pellets of $Cu_3Bi(SeO_3)_2O_2Cl$.

The authors have measured the dielectric permittivity of francisite, which displays a dielectric anomaly of very small amplitude at $T_c = 115\,\mathrm{K}$ between the two non-polar phases. This is also confirmed by measurements done in Ref. [155, 163], where the permittivity of both $Cu_3Bi(SeO_3)_2O_2Cl$ and $Cu_3Bi(SeO_3)_2O_2Br$ have been investigated. No dielectric anomaly is however visible in the latter.

It is however important to notice that the published dielectric measurements in Ref. [69] were performed along the c-axis and not along the a-axis which is the expected axis of the antiparallel ion displacements. The authors have repeated the measurements aligning the direction of the applied AC voltage with the a-axis that show a much clearer anomaly, independent of the measurement frequency in the studied range of 10 Hz to 100 kHz.

The authors also showed that an electrical polarisation could be induced, above a critical field, by a DC electric field while changing the temperature of the sample, see Fig. IV.5b. This polarisation was integrated from the pyroelectric current and could change sign by applying a DC electric field in the opposite direction. These pyroelectric measurements highlight the presence

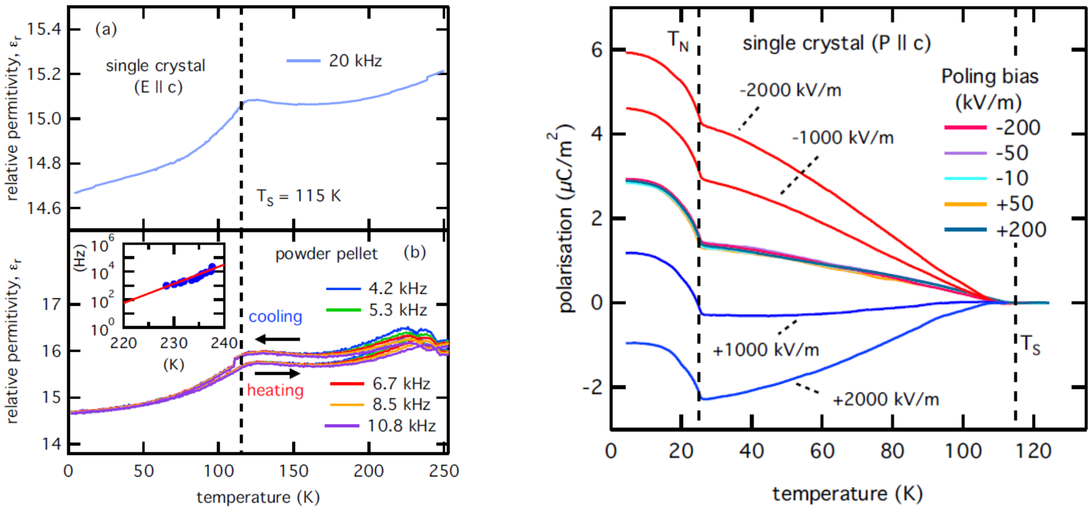

(a) (b)

Figure IV.5: (a) Dielectric anomaly visible at $T_c = 115\,\mathrm{K}$ in both single-crystals and pellets of francisite $Cu_3Bi(SeO_3)_2O_2Cl$. (b) Temperature-dependency of polarisation in francisite under an dc electric field. Adapted from Ref. [69].

of a polar phase reached for values of the electric field above a threshold critical field. Indeed, the $Pcmn$ phase below $T_c = 115\,\mathrm{K}$ is centrosymmetric and therefore should not display such a pyroelectric current. These measurements were realised in a static regime (DC field). Another possibility is that these currents are not pyroelectric but thermally stimulated discharge currents (TSDC), as seen in another model antiferroelectric in Ref. [67]. This could also explain the very low values of polarisation measured (order of magnitude: $0.0001\,\mu\mathrm{C\,cm}^{-2}$), which do not seem coherent with a switching towards a polar phase.

For a crystal displaying a phase transition, a comparison between experimental spectroscopic measurements and theoretical calculations of phonon dispersions in each phase and their instabilities can help us understand the dynamics of the transition. Instabilities are visible from calculated phonon dispersions as modes with imaginary frequencies. From these modes of imaginary frequency, the lowest-frequency mode is the leading instability. The unstable phase is then called a high-symmetry phase, as opposed to the low-symmetry phase which is a more stable phase derived from the instability. For a displacive system and when the material's temperature decreases towards the transition temperature T_c, this mode decreases in frequency, i.e. softens. Below T_c, this soft-mode condensates, meaning that the material reaches its low-symmetry phase (or ground state).

In Ref. [164], phonon dispersions of the three halogen francisites ($Cu_3Bi(SeO_3)_2O_2Cl$, [...]Br and [...]I) in their room temperature $Pmmn$ phase were calculated. Our collaborators also re-calculated phonon dispersions of $\mathrm{Cu_3Bi(SeO_3)_2O_2Cl}$ in both high- and low-symmetry through first-principles density functional theory computations, in order for us to access to the eigenvectors of the unstable modes. These calculations were performed in the DFT package VASP within the U-corrected Generalized Gradient Approximation (GGA+U) approximation. More technical details can be found in the supplementary materials of Ref. [70]. Most importantly, the phonon dispersion calculations of each phase were run in supercells to take into account the doubling of the unit cell along c across the phase transition.

For $\mathrm{Cu_3Bi(SeO_3)_2O_2Cl}$, both of these theoretical studies confirm the presence of unstable modes in the $Pmmn$ phase. The two lowest-frequency unstable modes are seen at the Γ point and at the Z point, see Fig. IV.6a or Ref [164]. The Γ point instability is polar and condensates to a ferroelectric $P2_1mn$ phase, while the Z instability condensates to a non-polar $Pcmn$ phase with a unit cell doubled along the c-axis compared to the $Pmmn$ unit cell. When looking into the eigenvectors linked to the non-polar mode located in Z, we can observe that this excitation is indeed antipolar, i.e. linked to the antiparallel displacements at the phase transition, as represented in Fig. IV.2.c. It is important to note that the mode located at the Γ point has a close, but higher, energy that the one at the Z point. When condensating each of these modes, the energy difference between $Pcmn$ and $P2_1mn$ is found to be small and around 3 meV/f.u. for the Cl francisite, with a lower energy for the non-polar $Pcmn$ phase. Ref. [164] finds also the same instabilities for the Br francisite while the I francisite is stable in its room temperature $Pmmn$ phase. Experimentally however, no phase transitions were observed in $\mathrm{Cu_3Bi(SeO_3)_2O_2Br}$.

On Fig. IV.6b are represented the DFT-calculated phonon dispersions of both $Pmmn$ and $Pcmn$ phases in the $Pcmn$ unit cell. In that case, it is important to notice that the most unstable mode of the high-symmetry phase (priorly located on the Z point) is on that representation folded onto the Γ point, due to the doubling of the unit cell along the c-axis.

IV.1.d Objectives of our experimental study of francisite $\mathrm{Cu_3Bi(SeO_3)_2O_2Cl}$

The first steps have been taken to prove that francisite $\mathrm{Cu_3Bi(SeO_3)_2O_2Cl}$ is an antiferroelectric. Namely, the presence of antiparallel displacements across the phase transition at $T_c = 115\,\mathrm{K}$ as well as the presence of a dielectric anomaly between high- and low-symmetry non-polar phases have been proven in earlier studies [69, 155]. The computational DFT study of the phonon dispersions [70, 164] brings, on top of this, another argument to the discussion, which is the proximity in energy from the supposed antiferroelectric phase to a polar phase.

This 115 K structural phase transition is of particular importance as it is a rare case of a unidi-

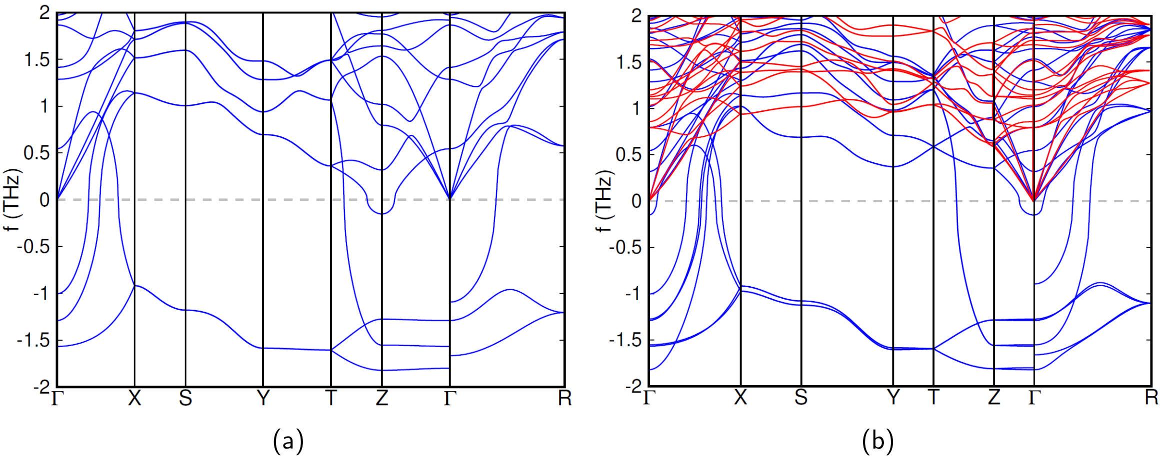

Figure IV.6: (a) DFT-calculated phonon dispersion of $Cu_3Bi(SeO_3)_2O_2Cl$ in the high symmetry $Pmmn$ phase in its primitive cell. (b) DFT-calculated phonon dispersions of $Cu_3Bi(SeO_3)_2O_2Cl$ in the high symmetry $Pmmn$ phase (in blue) and low symmetry $Pcmn$ phase (in red). Due to the doubling of the unit cell lattice at the phase transition, the dispersion for the high symmetry $Pmmn$ phase has been computed in a 1x1x2 supercell with respect to its primitive cell, so that it can be compared to the phonons of the low symmetry phase. Folding of the phonon branches should then be taken into account, as indicated in the main text.

mensional, non-ferroelastic (and even non-ferroic) phase transition that displays a mode softening.

In the following work, we will try to understand the driving mechanism of this candidate antiferroelectric phase transition by studying its low-frequency dynamics. Indeed, as shown in chapter I, if that phase transition is displacive, we should see a softening of the lowest-frequency mode driving the phase transition in the low-symmetry phase, such as the one seen in Refs. [155, 163]. The remaining question is then where is this soft-mode located in the Brillouin zone of the high-symmetry phase. If it is at the center, it would then be a polar mode. On the other hand, if it is located at the zone boundary, this mode would be antipolar. The latter is our hypothesis, due to the neutron diffraction experiments of Ref. [69].

IV.2 Experimental characterisation of the phase transition

IV.2.a Measured samples

The single crystals of $Cu_3Bi(SeO_3)_2O_2Cl$ studied in that work were synthesised by Helmuth Berger at the EPFL and given to us by Evan Constable from the TU Wien and collaborators. Due to the layered structure, francisite single-crystals grow in the ab-plane in thin slabs. The normal to the surface is then oriented along the c-axis. A picture of one of our sample is represented on Fig. IV.7 with its orientation.

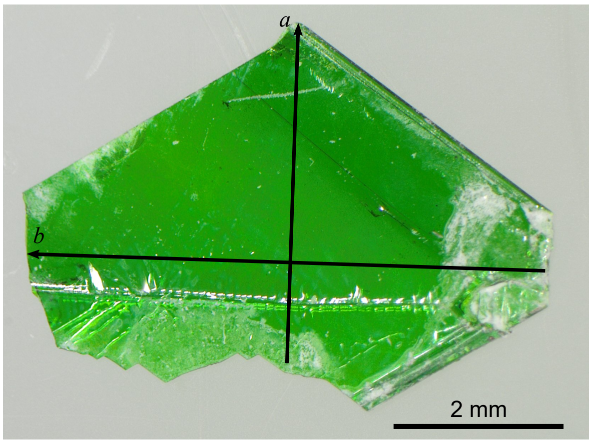

Figure IV.7: Optical image of a single crystal of francisite of $Cu_3Bi(SeO_3)_2O_2Cl$. a and b crystallographic axes are represented.

IV.2.b Softening of the mode at the Brillouin zone center below T_c by Raman spectroscopy

To study the phonon structure across the phase transition, we first performed temperature-dependent Raman spectroscopy measurements at high and low frequencies. The temperature range chosen was between room temperature and 10 K using our Oxford Instruments liquid He cryostat. However, we will purposefully not present in detail any spectrum below 30 K as the paramagnetic to antiferromagnetic phase transition taking place around $T_N = 25$ K was thoroughly studied in Refs. [155, 163] and not directly relevant to our study of the 115 K phase transition.

For the high frequency spectra, a He-Ne laser line of wavelength $\lambda = 633$ nm was used alongside a 1800 lines/mm grating. Spectra were acquired for 10 minutes with a power of around 300 µW focused with a x50 objective.

In both low- $Pcmn$ and high-symmetry $Pmmn$ phases, only A_g, B_{1g}, B_{2g} and B_{3g} excitations are Raman-active. The sample was oriented horizontally along the b-axis and vertically along a.

Fig. IV.8 displays high-frequency spectra of Francisite on both sides of the phase transition with different polarisation configuration: Fig. IV.8.a. with incident and scattered polarisation parallel to b (Porto notation: $-Z(YY)Z$), Fig. IV.8.b. parallel to a ($-Z(XX)Z$) and Fig. IV.8.c. incident parallel to b and scattered parallel to a ($-Z(XY)Z$). In these scattering geometries, only A_g modes are seen in parallel polarisation and only B_{1g} modes are seen in crossed polarisations.

The clearest sign of the phase transition is the apparition of two phonon modes at $\approx 138\,\mathrm{cm}^{-1}$ and $\approx 198\,\mathrm{cm}^{-1}$ in the $-Z(YY)Z$ spectra and a peak at $\approx 507\,\mathrm{cm}^{-1}$ on the $-Z(XY)Z$. According to Refs. [155, 163], several other peaks of weak intensity should come from the doubling of the unit cell. A better signal/noise ratio would be needed to distinguish these other modes. We here only pinpoint the most obvious mode appearing at the transition in our measurements, as high-frequency spectra were not the focus of this study. Indeed, the filter used for these measurements cut the spectra off around $55\,\mathrm{cm}^{-1}$, preventing us from seeing the lowest frequency modes, most relevant for our work.

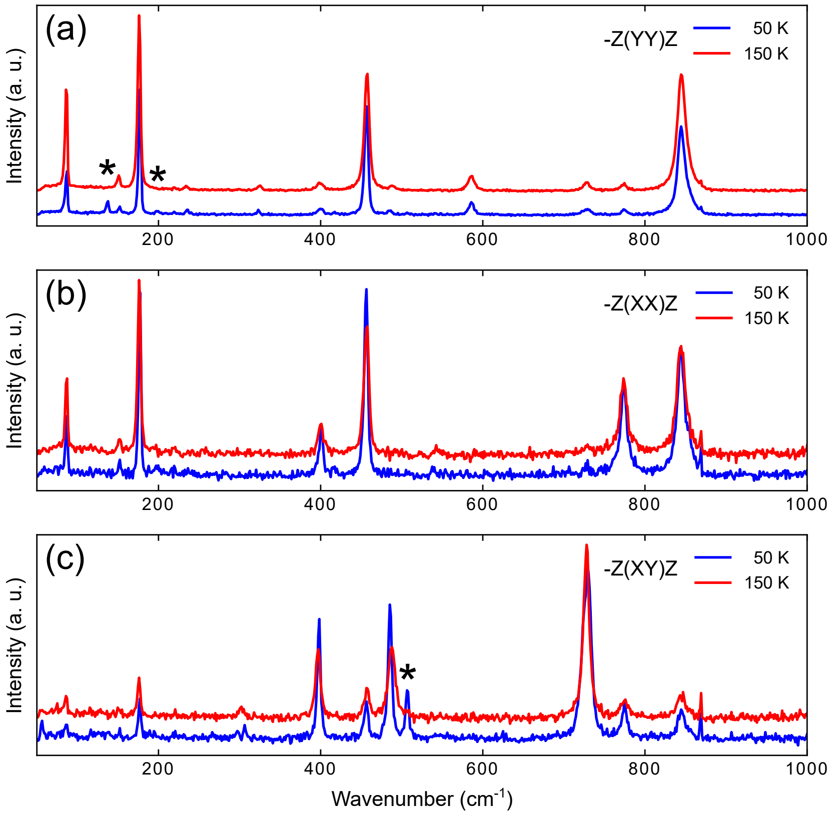

Figure IV.8: Raman spectra at 50 K and 150 K for different incident and scattered polarisations. (a) has both polarisations along the b, (b) both along a and (c) displays incident polarisation along a and scattered along b. Stars * indicate phonons appearing at the phase transition.

We used a He-Ne laser line of wavelength $\lambda = 633\,\mathrm{nm}$ and limited the spectra acquired to the lowest frequencies by using Bragg filters with a cut-off of around $10\,\mathrm{cm}^{-1}$ to remove most of the intensity of the peak due to elastic Rayleigh scattering. To get the best spectral resolution possible, we used the -1 order of a 2400 lines/mm grating. Spectra were acquired for 30 minutes with a power of around 300 µW focused with a x50 objective.

The Raman spectra of the low-frequency temperature study are represented on Fig. IV.9a. Incident polarisation was horizontal, i.e. parallel to the crystal b-axis. However, with these filters, no polariser was used on the optical path of the back-scattered beam. In that geometry, both A_g and B_{1g} excitations can be seen. We can clearly see six modes in the low frequency range between 0 and 100 cm^{-1}. We clearly see a mode softening from 30 K to around 115 K and disappearing above, in the high-symmetry phase. By comparison with the DFT-calculated mode frequencies and Ref. [163], the symmetry of the soft-mode is determined to be A_g.

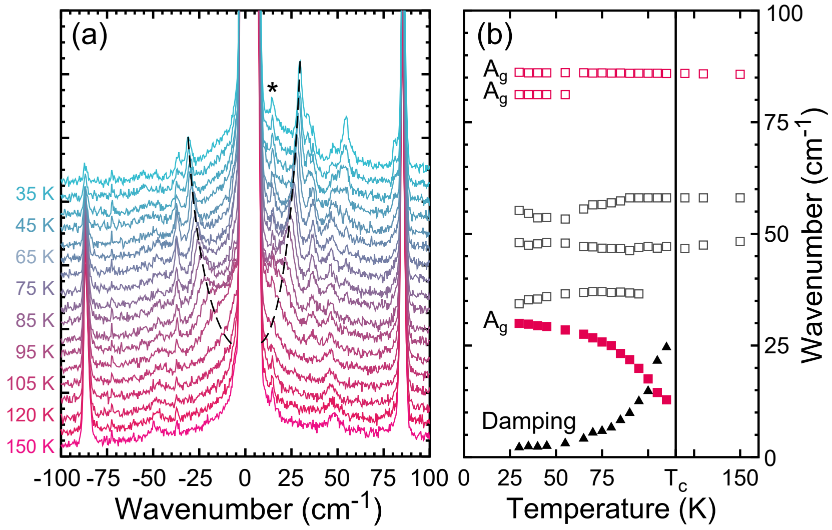

Figure IV.9: (a) Temperature-dependency of low frequency Raman spectra displaying both Stokes and anti-Stokes peaks. The softening of the lowest frequency mode is highlighted with dashed lines. The asterisk * indicates a low-frequency artefact present on every spectra on the Stokes side. (b) Temperature evolution of low-frequency modes. A_g modes are displayed on red. The soft-mode frequency is plotted with full squares and its damping with black triangles.

Spectra were fitted by damped harmonic oscillator line-shapes. The results of the fits are reproduced on Fig. IV.9b. where we can clearly see the softening of the lowest frequency mode, from 30 cm^{-1} at 30 K to around 13 cm^{-1} at 110 K. At the same time, the damping factor of the soft-mode increases until reaching an overdamping regime around 15 K below T_c, validating our choice of a damped harmonic oscillator line-shape over a lorentzian approximation.

The other hard modes barely see any changes frequency across the whole temperature range but some of them do disappear before the transition.

The presence of this soft-mode however is coherent with both a potential antiferroelectric $Pcmn$ phase driven by an antipolar instability and with a ferroelectric $P2_1mn$ induced by a polar instability. To confirm or infirm that this phase is antiferroelectric, we then needed a technique able to probe the whole Brillouin zone and see if we could observe this soft-mode in the high-symmetry phase, whether it is located at the $\mathit{\Gamma}$ or Z point. Given the description of the phase transition measured from neutron diffraction patterns [69] accompanied by a doubling of the unit cell along c, we think it more probable that the soft-mode is located at the Z point and therefore the transition to be towards an antipolar phase.

IV.2.c Probing the Brillouin zone boundary above T_C with inelastic x-ray scattering (IXS)

The techniques chosen for this study were inelastic x-ray scattering (IXS) and thermal diffuse scattering (TDS). As seen in chapter II, IXS and TDS allow for the study of phonon modes at zone boundaries near a phase transition. These experiments were performed at the ESRF ID28 beamline [102].

On Fig. IV.10.a., we display a characteristic inelastic x-ray spectrum acquired at the Z point $(5, 0, 0.5)$. The fitting was performed by using damped harmonic oscillators. Three modes and a pseudo-elastic central line fitted by a Lorentzian line-shape were enough to convincingly fit the IXS spectra until 125 K where the fitting model started to fail due to the overlapping of the lowest frequency mode with the central line. In the same wavenumber range (0 cm^{-1} to 120 cm^{-1}), we see more than three modes in our Raman spectroscopy measurements but also from the DFT-calculated mode frequency. This might be due to the 3 meV-resolution of the experiment. Indeed, it is difficult to separate the contributions of several modes that are close in energy and which are fitted by a single damped harmonic oscillator.

The lowest frequency ($\approx$ 3 meV) mode decreases in frequency with temperature, as shown in Fig. IV.10.b., and is identified as the soft-mode. The two-highest frequency modes are hard modes and might then be the result of a convolution of several modes. We will not push much further the investigation into the behaviour of these hard modes, as they are not directly influencing the phase transition.

On Fig. IV.11.a, IXS spectra were taken at room temperature at different (h 0 $-$0.5) points, where reciprocal coordinate h takes values between 5.0 and 5.5, i.e. along the $Z - U$ direction. On Fig. IV.11.b., the $\mathit{\Gamma} - Z$ direction is investigated by changing the reciprocal space coordinate l between $-$0.1 and $-$0.5 in (5 0 l) points. These same measurements have been repeated also at 200 K.

In both $\mathit{\Gamma} - Z$ and $Z - U$ directions, the further from Z the higher the frequency of the soft-

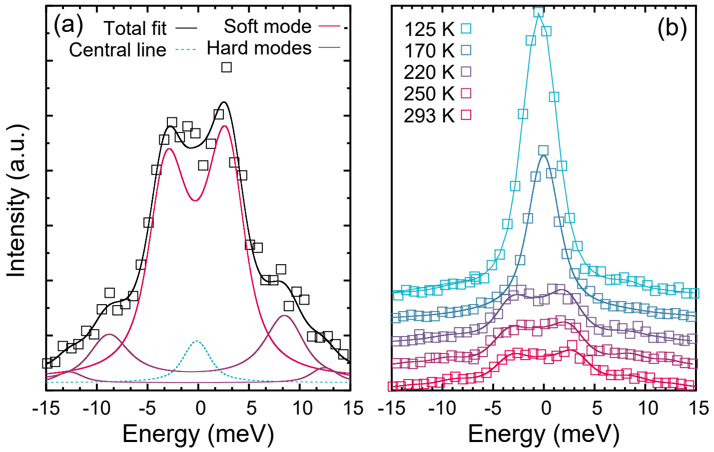

Figure IV.10: (a) Example of an IXS spectrum at room temperature at the Z point of coordinates $(5, 0, 0.5)$. Solid lines represent soft and hard modes fitted by damped harmonic oscillators. (b) Temperature-dependency of IXS spectra above $T_c = 115\,\mathrm{K}$.

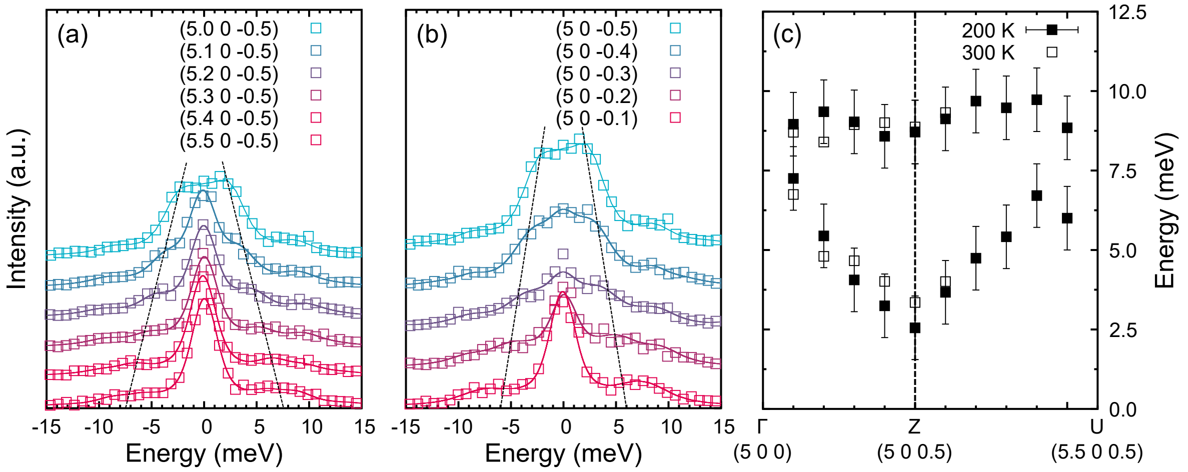

Figure IV.11: IXS spectra measured at room temperature along (a) $Z-U$ and (b) $\Gamma-Z$ directions. The soft-mode and first-mode positions were fitted for both 300 and 200 K. (c) represents these mode frequencies along the $\Gamma - Z - U$ Brillouin zone path.

mode is, while the lowest-energy hard mode keeps the same energy around 9 meV as represented in Fig. IV.11. These results first confirm that the lowest-frequency mode is an optical mode, as the energy of the mode does not go towards 0 meV. It also confirms the fact that the soft-mode is the lowest energy mode and is located on the Z point in the high-symmetry $Pmmn$ phase, as shown by the DFT calculations.

IV.2.d Probing at the Brillouin zone boundary above T_c with thermal diffuse scattering (TDS)

To extract at lower temperatures the soft-mode frequency, we also performed thermal diffuse scattering (TDS) experiments at the ESRF ID28 beamline [103].

From the IXS data, we can see that the dominant contribution of the spectrum is the soft-mode intensity. Hard modes do not significantly change in frequency across a wide range of temperature, so the temperature-dependency of the spectra is then principally due to the soft-mode. As discussed in chapter II and in Ref. [165], it becomes then relatively easy to extract the diffuse scattering intensity due to a single phonon with the help of previous IXS measurements.

To extract this thermal diffuse scattering intensity, reciprocal space maps of the $(h\ 0\ l)$ plane are then measured at temperatures between 100 K to room temperature and shown on Fig. IV.12.a. Blue circles represent the reflection (7 0 0.5) and red circles the (5 0 0.5). The temperature evolution of these reflections can be rescaled from the IXS data to extract the frequency of the soft-mode with respect to the temperature, as shown in Fig. IV.12.b. Data from IXS are also presented on the same graph and clearly follow the same square-root shape, typical of a soft-mode [10, 166]. There is a noticeable difference between the measured transition temperature ($\approx$ 107 K) and the usual experimental value of 115 K. This shift might simply be explained by the energy-limited resolution ($\approx$ 3 meV) IXS points used to rescale the TDS data.

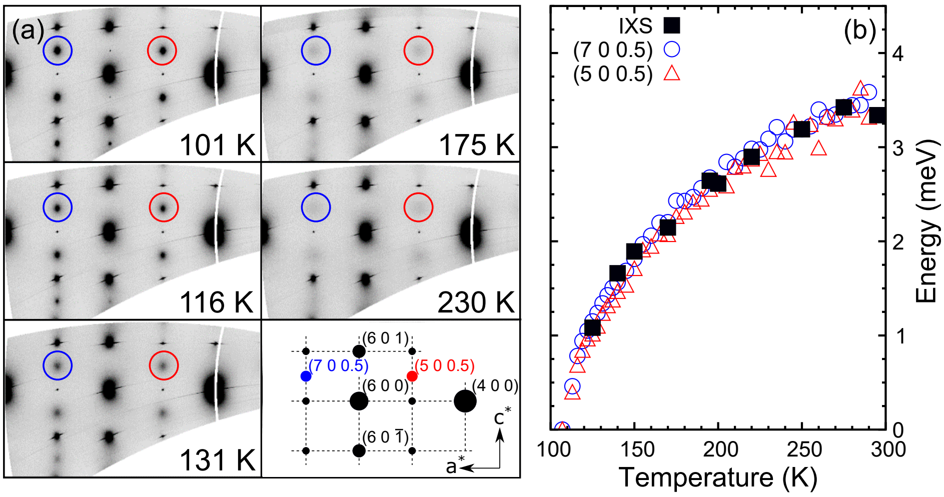

Figure IV.12: (a) Reciprocal space maps of $(h\ 0\ l)$ planes at different temperatures between 101 and 230 K. (b) Temperature dependency of the soft-mode above T_c extracted from IXS fitting and TDS analysis.

IV.2.e A clearly soft-mode driven antiferroelectric phase transition

Data from the three spectroscopic experiments are gathered on Fig. IV.13. There, the squared energy of the soft-mode is represented as a function of the temperature on the whole range studied.

In chapter I, we saw that in a displacive ferroic transition, the squared soft-mode frequency ω^2 is proportional to the second derivative of the free energy F with respect to the order parameter η:

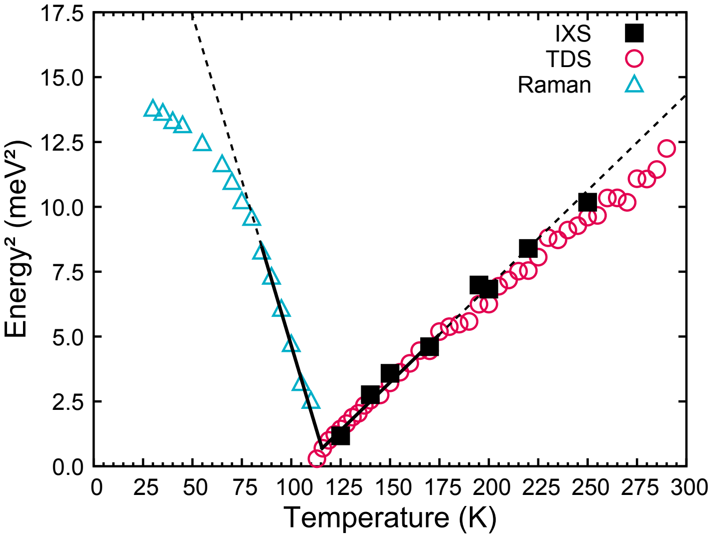

Figure IV.13: Evolution of the soft-mode squared energy above and below T_c, combining Raman, IXS and TDS measurements. The solid line shows the region used for the linear fitting while dashed lines show the extrapolation of these linear regressions.

$\frac{\partial^2 F}{\partial \eta^2}$. For a second-order transition described by a 2-4 Landau potential, we showed that this varies following $|T - T_c|$ above T_c and following $2|T - T_c|$ above T_c. For a tricritical phase transition, i.e. modelled by a 2-6 Landau potential, $\omega^2 \propto |T - T_c|$ above T_c and $\omega^2 \propto 4|T - T_c|$ below T_c.

In francisite, a linear behaviour is clearly visible in the vicinity of the phase transition. This linear fitting model starts to fail around 75 K in the lower-end of the temperatures, while it starts failing around 225 K above T_c.

The ratio of the slopes of these linear fits on each side of the transition is around 3.4, displaying a behaviour in between a tricritical (ratio of 4) and a second-order phase transition (ratio of 2). Such a behaviour has been seen in the model antiferrodistortive strontium titanate $SrTiO_3$ [167, 168].

At temperatures lower than T_c, it is known that magnetic ordering starts appearing. Indeed, Ref. [69] shows that there is a deviation of the magnetic susceptibility with respect to the classic Curie-Weiss law. Coupling between magnetic order and lattice could then explain, at least part of, the deviation from linearity in the low temperature range. Above T_c, the deviation might be due to a coupling or crossing with one of the hard modes.

IV.2.f Detailed analysis of the atomic contributions to the phonon eigenvectors

From the earlier neutron diffraction studies [69], only Cu and Cl ions appear to be shifting at the phase transition, picturing a very simple displacive transition. However, we now want to determine exactly which atoms move at the phase transition. To do this, thanks to the eigenvectors calculated by our collaborators from DFT, we project the atomic displacements of the soft-mode in the high-symmetry phase on the basis of the low-symmetry phase.

The main result of that analysis is that the A_g soft-mode in the high-symmetry phase projection is split onto some of the higher-frequency A_g modes of the low-symmetry phase, while higher frequency A_g modes of the high-symmetry phase fully contribute to the two lowest A_g modes of the low-symmetry phase. Fig. IV.14 visually represents this projection. In terms of atomic displacements, that means that the soft-mode above T_c is mainly due to the antiparallel displacements of Cl atoms while the soft-mode below T_c is a sum of displacements of Cl, Cu, Se and Bi atoms. The consequence of such a coupling will be explained in the next section.

As the behaviour of this phase transition is so close to a textbook Landau transition with a clear softening of the driving mode and given the dielectric anomaly between the two non-polar phase, the antiparallel displacements in the low-symmetry phase and the proximity of a polar mode shown by DFT, we feel confident in affirming that we have characterised the closest realisation of a Kittel-like antiferroelectric phase transition, which happens to be clearly a displacive phase transition.

IV.2.g Spectroscopy of francisite under electric field

The last proof needed to make francisite a textbook antiferroelectric is switching to a polar phase under electric field. However, studying the transition to a polar phase need not be measured directly via a polarisation curve but could be seen indirectly through diffraction or spectroscopy, and notably Raman spectroscopy.

For a displacive phase transition such as the one studied here, the soft-mode should be the most sensitive to an applied of the electric field. If the structure is entirely switched, some hard modes should also appear, disappear, split or shift depending on the symmetry of the polar phase and its selection rules.Experimentally, we tried to induce an antiferroelectric to ferroelectric phase transition by applying an electric field to our francisite crystal. This required to modify our low-temperature setup in our liquid He cryostat without success.

Francisite is a layered material, which makes it a delicate crystal to handle, prone to breaking easily. Our samples underwent a variety of different treatments, such as polishing, cutting, gluing amongst others. The temperature-induced phase transition was however found not to be reproducible, despite our attempts at cycling the sample in temperature and at applying small electric fields in both direction.

We will now show our first attempt at switching our francisite sample when the low-symmetry

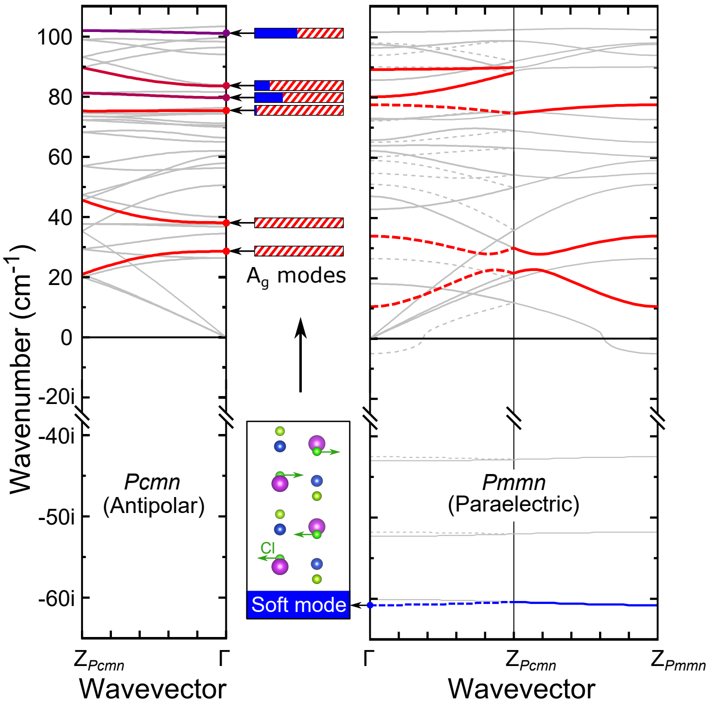

Figure IV.14: DFT-calculated phonon dispersions in the $\Gamma - Z$ branch in the low-symmetry $Pcmn$ (left hand-side) and high-symmetry $Pmmn$ (right hand-side) phases. The $Pmmn$ phase is showm in both its primitive cell and folded into the primitive cell of $Pcmn$, due to the doubling of unit cell at the phase transition. The branches connecting Γ to the Z point in the doubled cell (Z_{Pcmn}) are dashed for clarity. The soft-mode appears in blue while the other A_g modes are in red. The bars next to the A_g modes of the low-symmetry shows the contribution to the high-symmetry A_g modes coming from the low-symmetry soft-mode (blue filling) or low-symmetry A_g modes (dashed red filling).

could be reached. The sample was oriented and put on top of two large Pt electrodes separated by a 10 µm gap. Some silver paste was then applied on the sample surface to bring the electric field on the probed area. The gap between the two electrodes was around 150 µm. Fig. IV.15a displays the sample cryostat as-placed in the cryostat. These electrical contacts were then connected to a Keithley 2410 source meter.

Small electric fields of maximum 3.33 kV cm^{-1} were applied resulting in no visible changes in the position of the soft-mode or any other modes in the range of 10 to 400 cm^{-1}. The very small intensity variations between peaks could be linked with the small heating due to the average current flowing through the sample during the scan. On Fig. IV.15b, the results are summarised with full Raman spectra at different voltages and also zooms on the characteristic modes of the low-symmetry phase (soft-mode and mode around 137 cm).

Our goal was to apply much larger field until we could see a clear effect on the measured Raman spectra but this could not be realised due to the bad reproducibility of the phase transition on our prepared samples.

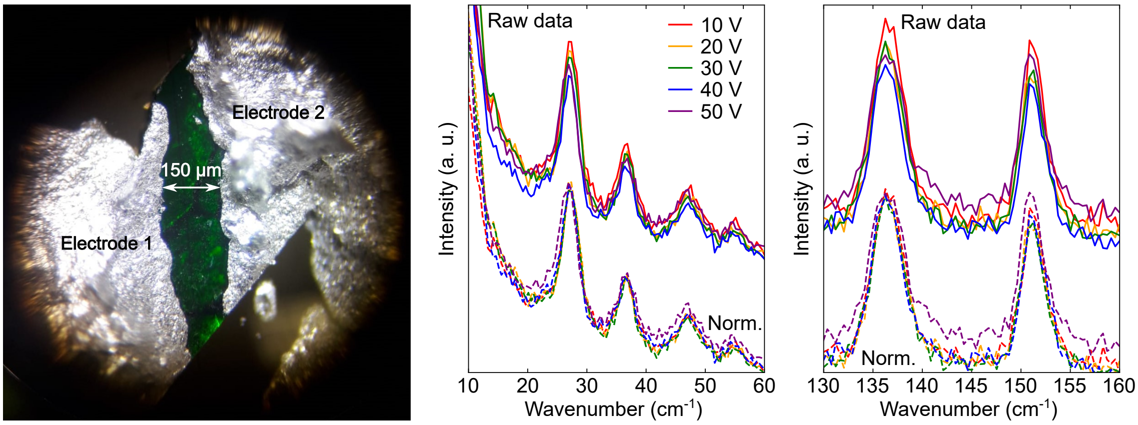

(a) (b)

Figure IV.15: (a) Picture of the sample surface and its painted electrical connections. (b) Barely no effect of the applied voltage on the sample is seen on the Raman spectra. Both raw data (full lines) and data normalised by the intensity of the 176 cm^{-1} mode (dashed lines) are represented.

IV.3 Conclusions and perspectives

IV.3.a Results summary

In this study of francisite, we drew a complete picture of the soft-mode dynamics around its 115 K phase transition. First, we measured with Raman spectroscopy the softening of the lowest-frequency phonon mode below $T_c = 115$ K and its disappearance above T_c. We then performed inelastic x-ray scattering experiments coupled with thermal diffuse scattering experiments and observed the softening of the lowest-frequency mode above T_c. The temperature evolution of this mode on both sides of T_c follows a typical soft-mode square-root law, proving the displacive character of this phase transition. When representing the mode energy with respect to the temperature, we can measure the ratio between the slopes of linear fits on each side of T_c, and find a value which hints between a second-order and a tricritical phase transition.

IV.3.b Perspectives

Two main topics are left to study on antiferroelectric francisite $Cu_3Bi(SeO_3)_2O_2Cl$.

First, stabilising a polar phase under an applied electric field is one of the key properties of an antiferroelectric and then should be the priority of the next experimental studies on francisites. Antiferroelectric switching of a material can be pretty difficult, for instance due to a breakdown field lower than the switching field or leakage. Heating up the sample until a few kelvins under T_c should then lower the field required to reach the polar phase and enable switching, unless leakage is a real issue in francisites. Francisite $Cu_3Bi(SeO_3)_2O_2Cl$ might however not be the ideal francisite to switch to a polar phase, due to the need of cryogenic cooling to reach a temperature lower than $T_c = 115$ K. For instance, $Cu_3Bi(TeO_3)_2O_2Cl$ may be more ideal as the antiferroelectric phase is already stable at room temperature [159]. Switching francisite to its polar phase is not only interesting to definitely prove that francisite is antiferroelectric but also because it displays a antiferromagnetic order below 25 K, making of francisite a unique antiferromagnetic/antiferroelectric magnetoelectric.

In the lower-symmetry phase between Γ and Z, the unstable phonon branch carrying the soft-mode is almost flat, according to the density functional theory calculations. An entirely unstable and flat branch typically describes an order-disorder transition, as no phonon modes can drive the transition, i.e. there is no softening. The shape of the dispersion would then argue for an order-disorder transition rather than a displacive one. This result is in direct contradiction with our results on mode-softening and raises also a more fundamental question on why DFT calculations could not predict the displacive character of this phase transition. One of the reasons could be that these DFT calculations have been performed at an effective temperature of 0 K and thus does not take into account any anharmonic effects. Building such an anharmonic model is not a trivial work but would however be necessary to really predict the temperature-dependent phonon dispersions of francisite, and hence try to see if DFT can reproduce the displacive character of the phase transition.

Contributions

I would like to first thank our external collaborators E. Constable, V. Simonet and S. de Brion for sharing the samples, the beam-time and their expertise with us and for all of the fruitful discussions around the paper. Many thanks to L. Paolasini and A. Bosak for the TDS data analysis, discussions, sample and beamtime preparation and for running the beamline so smoothly. I also would like to thank H. Berger for synthesising the samples.

Special thanks to C. Toulouse for designing and setting up the whole low-temperature Raman setup as well as your precious help for the measurements and the writing of the paper. A great thanks to H. Aramberri Del Vigo and J. Íñiguez Gonzalez for the scientific discussion and the DFT calculations that helped us greatly in understanding the atomistic picture of the transition. Thank you M. Guennou, for leading this study.

This work was published in Physical Review Letters in 2020, c.f. Ref. [70].

Conclusions

In the following paragraphs, I will summarise and highlight the importance of the results obtained during my Ph.D.

We first synthesised high-quality thin films of canonical antiferroelectric $PbZrO_3$ and have shown that these films could be electrically switched in two different geometries: either with out-of-plane or in-plane applied fields. In-plane switching of antiferroelectric thin films have been seldom reported and, to the best of our knowledge, were never characterised as completely as in this work. Our optical observation of the antiferroelectric switching of our films is also original to this thesis. Our results on $PbZrO_3$ thin films might then encourage researchers to assess the interest of the in-plane geometry for antiferroelectric thin films applications but also to try to create optical devices based on this in-plane switching.

The lack of textbook antiferroelectrics led us to look for new model materials. For that reason, we performed a spectroscopic study of the lattice dynamics of francisite by combining lab-based and synchrotron-based scattering techniques. To us, francisite is an ideal candidate to fill in for the lack of models, as this material displays a unique combination of an antiferroelectric with a displacive phase transition. Our results on this material as our complete characterisation of this candidate model uncovers the first example of a displacive antiferroelectric to the antiferroelectric community.

Antiferroelectricity is on a period of growth and we hope that our work results in noticeable advances in applications of antiferroelectric thin films and on the fundamental understanding of these materials.

Appendix A

List of publications

Published journal articles from my PhD thesis:

- Archetypal Soft-Mode-Driven Antipolar Transition in Francisite $Cu_3Bi(SeO_3)_2O_2Cl$, C. Milesi-Brault et. al., Physical Review Letters **124**, 097603 (2020)
- Critical field anisotropy in the antiferroelectric switching of $PbZrO_3$films, C. Milesi-Brault et. al., Applied Physics Letters **118**, 042901 (2021)
- The other model antiferroelectric: $PbHfO_3$ thin films from ALD precursors, B. Hanrahan et. al., APL Materials **9**, 021108 (2021)

In-press:

- Solution-processed $BiFeO_3$ thin films with low leakage current, A. Blazquez-Martinez et. al., Journal of the European Ceramics Society, *just accepted* (2021)

References

[1] V. Wadhawan, Introduction to Ferroic Materials (CRC Press, Dec. 2000), p. 6.

[2] S. Gnewuch and E. E. Rodriguez, "The fourth ferroic order: Current status on ferrotoroidic materials", Journal of Solid State Chemistry **271**, 175–190 (2019).

[3] E. K. Salje, Phase Transitions in Ferroelastic and Co-elastic Crystals (Cambridge University Press, Jan. 1991).

[4] E. K. Salje, Ferroelastic materials, Aug. 2012.

[5] R. Becker and W. Döring, "Allgemeine Theorie des Ferromagnetismus", in Ferromagnetismus (1939), pp. 25–101.

[6] W. J. Merz, "The Electric and Optical Behavior of BaTiO3 Single-Domain Crystals", Physical Review **76**, 1221–1225 (1949).

[7] N. Wongdamnern, A. Ngamjarurojana, Y. Laosiritaworn, S. Ananta, and R. Yimnirun, "Dynamic ferroelectric hysteresis scaling of BaTiO3 single crystals", Journal of Applied Physics **105**, 044109 (2009).

[8] T. Furukawa, "Ferroelectric properties of vinylidene fluoride copolymers", Phase Transitions **18**, 143–211 (1989).

[9] K. M. Rabe, C. H. Ahn, and J.-M. Triscone, Topics in Applied Physics: Physics of Ferroelectrics, Vol. 105 (2007).

[10] M. T. Dove, "Theory of displacive phase transitions in minerals", American Mineralogist **82**, 213–244 (1997).

[11] R. J. Nelmes and W. F. Kuhs, "The crystal structure of tetragonal PbTiO3 at room temperature and at 700 K", Solid State Communications **54**, 721–723 (1985).

[12] I. Tomeno, J. A. Fernandez-Baca, K. J. Marty, K. Oka, and Y. Tsunoda, "Simultaneous softening of acoustic and optical modes in cubic pbtio$_3$", Phys. Rev. B **86**, 134306 (2012).

[13] J. Hlinka, B. Hehlen, A. Kania, and I. Gregora, "Soft mode in cubic PbTiO3 by hyper-Raman scattering", Physical Review B - Condensed Matter and Materials Physics **87**, 064101 (2013).

[14] W. Cai and A. Katrusiak, "Structure of the high-pressure phase IV of KH 2 PO 4 (KDP)", Dalton Trans. **42**, 863–866 (2013).

[15] S. Havlin, "Longitudinal and transverse dielectric constants of KDP-type ferro- and antiferroelectrics", Ferroelectrics **71**, 183–223 (1987).

[16] W. Zhong, D. Vanderbilt, and K. M. Rabe, "First-principles theory of ferroelectric phase transitions for perovskites: The case of BaTiO3", Physical Review B **52**, 6301–6312 (1995).

[17] E. A. Stern, "Character of order-disorder and displacive components in barium titanate", Physical Review Letters **93**, 1–3 (2004).

[18] C. Kittel, "Theory of antiferroelectric crystals", Phys. Rev. **82**, 729 (1951).

[19] C. Kittel, Introduction to solid state physics (Wiley, 1996), p. 673.

[20] A. Levanyuk and D. Sannikov, "Anomalies in Dielectric Properties in Phase Transitions", Soviet Journal of Experimental and Theoretical Physics **28**, 134 (1969).

[21] P. Tolédano and M. Guennou, "Theory of antiferroelectric phase transitions", Physical Review B **94**, 014107-1–014107-6 (2016).

[22] S. Horiuchi, R. Kumai, and S. Ishibashi, "Strong polarization switching with low-energy loss in hydrogen-bonded organic antiferroelectrics", Chem. Sci. **9**, 425–432 (2018).

[23] G. Shirane, E. Sawaguchi, and Y. Takagi, "Dielectric properties of lead zirconate", Physical Review **84**, 476–481 (1951).

[24] H. Fujishita and S. Katano, "Re-Examination of the Antiferroelectric Structure of PbZrO3", Journal of the Physical Society of Japan **66**, 3484–3488 (1997).

[25] X. Dai, J. F. Li, and D. Viehland, "Weak ferroelectricity in antiferroelectric lead zirconate", Physical Review B **51**, 2651–2655 (1995).

[26] R. Kagimura and D. J. Singh, "First-principles investigations of elastic properties and energetics of antiferroelectric and ferroelectric phases of $PbZrO_3$", Phys. Rev. B **77**, 104113 (2008).

[27] G. H. Haertling, "PLZT electrooptic materials and applications—a review", Ferroelectrics **75**, 25–55 (1987).

[28] F. Wang, K. K. Li, and G. H. Haertling, "Transverse electro-optic effect of antiferroelectric lead zirconate thin films", Optics Letters **17**, 1122 (1992).

[29] V. J. Tennery, “A Study of the Phase Transitions in PbZrO3”, Journal of The Electrochemical Society **112**, 1117 (1965).

[30] V. J. Tennery, “High-Temperature Phase Transitions in PbZrO3”, Journal of the American Ceramic Society **49**, 483–486 (1966).

[31] K. Roleder, G. E. Kugel, J. Handerek, M. D. Fontana, C. Carabatos, M. Hafid, and A. Kania, “The first evidence of two phase transitions in PbZrO3 crystals derived from simultaneous Raman and dielectric measurements”, Ferroelectrics **80**, 161–164 (1988).

[32] R. Faye, “Structure et propriétés d'un antiferroélectrique modèle : PbZrO3”, PhD thesis (Ecole Centrale Paris, 2014).

[33] H. Liu, “Origin of the intermediate phase in lead zirconate, $PbZrO_3$”, Journal of the American Ceramic Society **101**, 5281–5286 (2018).

[34] L. You, F. Zheng, L. Fang, Y. Zhou, L. Z. Tan, Z. Zhang, G. Ma, D. Schmidt, A. Rusydi, L. Wang, L. Chang, A. M. Rappe, and J. Wang, “Enhancing ferroelectric photovoltaic effect by polar order engineering”, Science Advances **4**, eaat3438 (2018).

[35] H. Aramberri and J. Íñiguez, “Antiferroelectricity in a family of pyroxene-like oxides with rich polymorphism”, Communications Materials **1**, 52 (2020).

[36] C. Milesi-Brault, N. Godard, S. Girod, Y. Fleming, B. El Adib, N. Valle, S. Glinšek, E. Defay, and M. Guennou, “Critical field anisotropy in the antiferroelectric switching of PbZrO3 films”, Applied Physics Letters **118**, 042901 (2021).

[37] G. A. Samara, “Pressure and Temperature Dependence of the Dielectric Properties and Phase Transitions of the Antiferroelectric Perovskites: PbZrO3 and PbHfO3”, Physical Review B **1**, 3777–3786 (1970).

[38] O. E. Fesenko and L. E. Balyunis, “The temperature-electric field phase diagram of lead hafnate”, Ferroelectrics **29**, 37–40 (1980).

[39] B. Hanrahan, C. Milesi-Brault, A. Leff, A. Payne, S. Liu, M. Guennou, and N. Strnad, “The other model antiferroelectric: PbHfO3 thin films from ALD precursors”, APL Materials **9**, 021108 (2021).

[40] M. H. Francombe and B. Lewis, “Structural and electrical properties of silver niobate and silver tantalate”, Acta Crystallographica **11**, 175–178 (1958).

[41] D. Fu, M. Endo, H. Taniguchi, T. Taniyama, and M. Itoh, “Agnbo3: a lead-free material with large polarization and electromechanical response”, Applied Physics Letters **90**, 252907 (2007).

[42] L. Cross and B. Nicholson, "LV. The optical and electrical properties of single crystals of sodium niobate", The London, Edinburgh, and Dublin Philosophical Magazine and Journal of Science **46**, 453–466 (1955).

[43] A. C. Sakowski-Cowley, K. Łukaszewicz, and H. D. Megaw, "The structure of sodium niobate at room temperature, and the problem of reliability in pseudosymmetric structures", Acta Crystallographica Section B Structural Crystallography and Crystal Chemistry **25**, 851–865 (1969).

[44] P. Tolédano and D. D. Khalyavin, "Symmetry-determined antiferroelectricity in $\mathrm{PbZrO_3}$, $\mathrm{NaNbO_3}$, and $\mathrm{PbHfO_3}$", Physical Review B **99**, 024105–024105 (2019).

[45] D. Arnold, "Composition-driven structural phase transitions in rare-earth-doped BiFeO3 ceramics: A review", IEEE Transactions on Ultrasonics, Ferroelectrics, and Frequency Control **62**, 62–82 (2015).

[46] I. Anusca, S. Balčiūnas, P. Gemeiner, Š. Svirskas, M. Sanlialp, G. Lackner, C. Fettkenhauer, J. Belovickis, V. Samulionis, M. Ivanov, B. Dkhil, J. Banys, V. V. Shvartsman, and D. C. Lupascu, "Dielectric Response: Answer to Many Questions in the Methylammonium Lead Halide Solar Cell Absorbers", Advanced Energy Materials **7**, 1–12 (2017).

[47] Z. Wu, X. Liu, C. Ji, L. Li, S. Wang, Y. Peng, K. Tao, Z. Sun, M. Hong, and J. Luo, "Discovery of an Above-Room-Temperature Antiferroelectric in Two-Dimensional Hybrid Perovskite", Journal of the American Chemical Society **141**, 3812–3816 (2019).

[48] T. Hirose and K. Furukawa, "Dielectric anomaly of tungsten trioxide WO3 with giant dielectric constant", Physica Status Solidi (A) Applications and Materials Science **203**, 608–615 (2006).

[49] H. Hamdi, E. K. H. Salje, P. Ghosez, and E. Bousquet, "First-principles reinvestigation of bulk WO3", Physical Review B **94**, 245124 (2016).

[50] Y. Liu, X. Yang, C. He, X. Li, Z. Wang, Y. Xiao, and X. Long, "Domain and antiferroelectric properties of Pb(Lu1/2Nb1/2)O3 single crystals and their superlattice structure", RSC Advances **7**, 3704–3712 (2017).

[51] M. Pešić, M. Hoffmann, C. Richter, T. Mikolajick, and U. Schroeder, "Nonvolatile random access memory and energy storage based on antiferroelectric like hysteresis in zro2", Advanced Functional Materials **26**, 7486–7494 (2016).

[52] M. Hoffmann, T. Schenk, M. Pešić, U. Schroeder, T. Mikolajick, M. Hoffmann, T. Schenk, and M. Pe, "Insights into antiferroelectrics from first-order reversal curves Insights into antiferroelectrics from first-order reversal curves", **182902** (2017).

[53] H. Unoki and T. Sakudo, "Dielectric Anomaly and Improper Antiferroelectricity at the Jahn-Teller Transitions in Rare-Earth Vanadates", Physical Review Letters **38**, 137–140 (1977).

[54] R. Ramirez and J. A. Gonzalo, "Comparative analysis of the antiferroelectric behaviour in C4O4H2 and NH4H2PO4", Solid State Communications **75**, 481–482 (1990).

[55] B. Lamotte, J. Gaillard, and O. Constantinescu, "Esr identification of slater configurations and of exchange of the (aso4)4−− radical in irradiated ferroelectric kh2aso4 and kd2aso4 and antiferroelectric nh4h2aso4 and nd4d2aso4", The Journal of Chemical Physics **57**, 3319–3329 (1972).

[56] J. Gaillard and P. Gloux, "Etude du comportement de radicaux libres à la transition de phase et en phase antiferroélectrique de nh4h2aso4", Molecular Physics **44**, 841–847 (1981).

[57] Y. Makita, "Phase transition in csh3(seo3)2", Journal of the Physical Society of Japan **20**, 1567–1575 (1965).

[58] J. Roos and R. Kind, "The structure of ag2h3io6 in the antiferroelectric phase determined by quadrupole perturbed nmr-spectroscopy", Ferroelectrics **8**, 553–554 (1974).

[59] J. Roos, R. Kind, and J. Petzelt, "Phase transitions and lattice dynamics in Ag2H3IO6 and (NH4)2H3IO6", Zeitschrift für Physik B Condensed Matter and Quanta **24**, 99–112 (1976).

[60] K. Okada, "Antiferroelectric phase transition in copper-formate tetrahydrate", Phys. Rev. Lett. **15**, 252–254 (1965).

[61] Y. Makita and I. Seo, "Critical slowing-down process of dielectric relaxation in antiferroelectric cu(hcoo)2·4h2o", The Journal of Chemical Physics **51**, 3058–3065 (1969).

[62] K. Kobayashi, S. Horiuchi, S. Ishibashi, Y. Murakami, and R. Kumai, "Field-Induced Antipolar–Polar Structural Transformation and Giant Electrostriction in Organic Crystal", Journal of the American Chemical Society **140**, 3842–3845 (2018).

[63] R. R. dos Santos, B. Koiller, J. P. von der Weid, S. C. Ribeiro, A. S. Chaves, and F. C. S. Barreto, "The antiferroelectric phase in KCN", Journal of Physics C: Solid State Physics **11**, 4557–4564 (1978).

[64] A. Anderson, P. Gash, and F. Lüty, "Lattice Dynamics of KCN and NaCN in the Anti-Ferroelectric Phase", physica status solidi (b) **105**, 315–325 (1981).

[65] H. T. Stokes and D. M. Hatch, "Model for the ordered phases in KCN and NaCN", Physical Review B **30**, 3845–3858 (1984).

[66] H. L. Liu, C. R. Huang, G. F. Luo, and W. N. Mei, "Optical properties of antiferroelectric Cs2Nb4O11 : Absorption spectra and first-principles calculations", Journal of Applied Physics **110**, 103515 (2011).

[67] K. Geirhos, J. Langmann, L. Prodan, A. A. Tsirlin, A. Missiul, G. Eickerling, A. Jesche, V. Tsurkan, P. Lunkenheimer, W. Scherer, and I. Kézsmárki, "Antiferroelectricity Driven by Cluster Jahn-Teller Effect in the Lacunar Spinel $GaNb_4S_8$", arXiv cond-mat.str-el **2009.07680** (2020).

[68] P. Shan, J. Xiong, Z. Wang, C. He, X. Yang, R. Su, and X. Long, "Lead-free polar borate crystal K3Nb3B2O12: a novel antiferroelectric structure type", Journal of Materials Chemistry C **8**, 6654–6658 (2020).

[69] E. Constable, S. Raymond, S. Petit, E. Ressouche, F. Bourdarot, J. Debray, M. Josse, O. Fabelo, H. Berger, S. de Brion, and V. Simonet, "Magnetic and dielectric order in the kagomelike francisite $Cu_3Bi(SeO_3)_2O_2Cl$", Phys. Rev. B **96**, 014413 (2017).

[70] C. Milesi-Brault, C. Toulouse, E. Constable, H. Aramberri, V. Simonet, S. De Brion, H. Berger, L. Paolasini, A. Bosak, J. Íñiguez, and M. Guennou, "Archetypal Soft-Mode-Driven Antipolar Transition in Francisite Cu3Bi (SeO3)2 O2Cl", Physical Review Letters **124**, 5–10 (2020).

[71] Z. Liu, T. Lu, J. Ye, G. Wang, X. Dong, R. Withers, and Y. Liu, "Antiferroelectrics for Energy Storage Applications: a Review", Advanced Materials Technologies **3**, 1800111–1800111 (2018).

[72] A. S. Mischenko, Q. Zhang, J. F. Scott, R. W. Whatmore, and N. D. Mathur, "Giant electrocaloric effect in thin-film PbZr0.95Ti 0.05O_3", Science **311**, 1270–1271 (2006).

[73] A. Torelló, P. Lheritier, T. Usui, Y. Nouchokgwe, M. Gérard, O. Bouton, S. Hirose, and E. Defay, "Giant temperature span in electrocaloric regenerator", Science **370**, 125–129 (2020).

[74] J. Ding, D.-F. Shao, M. Li, L.-W. Wen, and E. Y. Tsymbal, "Two-dimensional antiferroelectric tunnel junction", Phys. Rev. Lett. **126**, 057601 (2021).

[75] G. Apachitei, J. J. P. Peters, A. M. Sanchez, D. J. Kim, and M. Alexe, "Antiferroelectric Tunnel Junctions", Advanced Electronic Materials **3**, 1700126–1700126 (2017).

[76] J. F. Scott, "Soft-mode spectroscopy: experimental studies of structural phase transitions", Rev. Mod. Phys. **46**, 83–128 (1974).

[77] W. J. Merz, "Double hysteresis loop of $batio_3$ at the curie point", Phys. Rev. **91**, 513–517 (1953).

[78]D. Lee, H. S. Kim, S. Y. Jang, K. W. Joh, T. W. Noh, J. Yu, C. E. Lee, and J. G. Yoon, "Double polarization hysteresis loop induced by the domain pinning by defect dipoles in HoMnO3 epitaxial thin films", Physical Review B - Condensed Matter and Materials Physics **81**, 2–5 (2010).

[79]G. Catalan, A. Janssens, G. Rispens, S. Csiszar, O. Seeck, G. Rijnders, D. H. Blank, and B. Noheda, "Polar domains in lead titanate films under tensile strain", Physical Review Letters **96**, 1–4 (2006).

[80]F. Borodavka, I. Gregora, A. Bartasyte, S. Margueron, V. Plausinaitiene, A. Abrutis, and J. Hlinka, "Ferroelectric nanodomains in epitaxial PbTiO3 films grown on SmScO3 and TbScO3 substrates", Journal of Applied Physics **113**, `10.1063/1.4801966` (2013).

[81]S. Matzen, O. Nesterov, G. Rispens, J. A. Heuver, M. Biegalski, H. M. Christen, and B. Noheda, "Super switching and control of in-plane ferroelectric nanodomains in strained thin films", Nature Communications **5**, 1–8 (2014).

[82]Y. Bai, X. Han, X. C. Zheng, and L. Qiao, "Both high reliability and giant electrocaloric strength in BaTiO 3 ceramics", Scientific Reports **3**, 3–7 (2013).

[83]T. Granzow, E. Suvaci, H. Kungl, and M. J. Hoffmann, "Deaging of heat-treated iron-doped lead zirconate titanate ceramics", Applied Physics Letters **89**, 262908 (2006).

[84]L. Čakare, B. Malič, M. Kosec, and A. Sternberg, "Antiferroelectric $PbZrO_3$ films prepared by sol-gel processing", Ferroelectrics **241**, 107–114 (2000).

[85]K. Budd, S. Dey, and D. Payne, "Sol-gel processing of pbtio3, pbzro3, pzt, and plzt thin films.", English (US), in British ceramic proceedings, edited by B. Steele (1985), pp. 107–121.

[86]C. Gutiérrez-Lázaro, I. Bretos, R. Jiménez, J. Ricote, H. E. Hosiny, D. Pérez-Mezcua, R. J. Jiménez Rioboó, M. García-Hernández, and M. L. Calzada, "Solution Synthesis of BiFeO 3 Thin Films onto Silicon Substrates with Ferroelectric, Magnetic, and Optical Functionalities", Journal of the American Ceramic Society **96**, edited by R. Riman, 3061–3069 (2013).

[87]T. Schenk, N. Godard, A. Mahjoub, S. Girod, A. Matavz, V. Bobnar, E. Defay, and S. Glinsek, "Toward thick piezoelectric hfo2-based films", physica status solidi (RRL) – Rapid Research Letters **14**, 1900626 (2020).

[88]I. Bretos, R. Jiménez, C. Gutiérrez-Lázaro, I. Montero, and M. L. Calzada, "Defect-mediated ferroelectric domain depinning of polycrystalline $BiFeO_3$ multiferroic thin films", Applied Physics Letters **104**, 092905 (2014).

[89]M. Eisa, E. MA, A. MF, and G. AM, "The system tio2-pb-o in air", (1980).

[90] J. Zhai and H. Chen, "Direct current field and temperature dependent behaviors of antiferroelectric to ferroelectric switching in highly (100)-oriented $PbZrO_3$ thin films", Applied Physics Letters **82**, 2673–2675 (2003).

[91] D. S. Yoon, C. J. Kim, J. S. Lee, W. J. Lee, and K. No, "Epitaxial growth of sol-gel PLZT thin films", Journal of Materials Research **9**, 420–425 (1994).

[92] A. W, N. Ashcroft, N. Mermin, N. Mermin, and B. P. Company, Solid state physics, HRW international editions (Holt, Rinehart and Winston, 1976).

[93] F. K. Lotgering, "Topotactical reactions with ferrimagnetic oxides having hexagonal crystal structures-I", Journal of Inorganic and Nuclear Chemistry **9**, 113–123 (1959).

[94] D. Damjanovic, "Hysteresis in piezoelectric and ferroelectric materials", in The science of hysteresis, Vol. 3 (Elsevier, 2006), pp. 337–465.

[95] E. Defaÿ, Integration of ferroelectric and piezoelectric thin films: [...] for microsystems, ISTE (Wiley, 2013).

[96] R. Nigon, T. M. Raeder, and P. Muralt, "Characterization Methodology for Lead Zirconate Titanate Thin Films with Interdigitated Electrode Structures — Supplementary material", Journal of Applied Physics **121**, 204101–204101 (2017).

[97] W. Hayes and R. Loudon, Scattering of light by crystals, English (Wiley New York, 1978), 360 p.

[98] E. Garmire, M. Cardona, J. Hammer, H. Kogelnik, T. Tamir, and F. Zernike, Light scattering in solids 1, Topics in Applied Physics (Springer Berlin Heidelberg, 2013).

[99] M. Cardona, R. Chang, G. Güntherodt, M. Long, and H. Vogt, Light scattering in solids 2, Topics in Applied Physics (Springer Berlin Heidelberg, 1982).

[100] M. C. Weber, "ELECTRONIC AND STRUCTURAL PROPERTIES OF BISMUTH- AND RARE-EARTH-FERRITES", PhD thesis (University of Luxembourg, 2016), p. 166.

[101] F. LaPlant, G. Laurence, and D. Ben-Amotz, "Theoretical and Experimental Uncertainty in Temperature Measurement of Materials by Raman Spectroscopy", Applied Spectroscopy **50**, 1034–1038 (1996).

[102] M. Krisch and F. Sette, "Inelastic X-Ray Scattering from Phonons", in Link.springer.com, Vol. 108, Chapter 5 (2006), pp. 317–370.

[103]A. Girard, T. Nguyen-Thanh, S. M. Souliou, M. Stekiel, W. Morgenroth, L. Paolasini, A. Minelli, D. Gambetti, B. Winkler, and A. Bosak, "A new diffractometer for diffuse scattering studies on the ID28 beamline at the ESRF", Journal of Synchrotron Radiation **26**, 272–279 (2019).

[104]T. Welberry and T. Weber, "One hundred years of diffuse scattering", Crystallography Reviews **22**, 2–78 (2016).

[105]A. Bosak, D. Chernyshov, B. Wehinger, B. Winkler, M. Le Tacon, and M. Krisch, "In-between Bragg reflections: thermal diffuse scattering and vibrational spectroscopy with x-rays", Journal of Physics D: Applied Physics **48**, 504003 (2015).

[106]C.-C. Hsueh and M. L. MeCartney, "Ten analyses of sol-gel derived and sputtered pzt thin films", MRS Proceedings **200**, 219 (1990).

[107]K. D. Preston and G. H. Haertling, "Microstructural investigation of acetate-derived plzt films", Integrated Ferroelectrics **1**, 89–98 (1992).

[108]K. K. Li, F. Wang, and G. H. Haertling, "Antiferroelectric lead zirconate thin films derived from acetate precursors", Journal of Materials Science **30**, 1386–1390 (1995).

[109]X. G. Tang, J. Wang, X. X. Wang, and H. L. W. Chan, "Electrical properties of highly (111)-oriented lead zirconate thin films", Solid State Communications **130**, 373–377 (2004).

[110]X. Hao, J. Zhai, J. Zhou, Z. Yue, J. Yang, W. Zhao, and S. An, "Structure and electrical properties of $PbZrO_3$ antiferroelectric thin films doped with barium and strontium", Journal of Alloys and Compounds **509**, 271–275 (2011).

[111]M. D. Nguyen, T. T. Trinh, H. T. Dang, and H. N. Vu, "Understanding the effects of electric-field-induced phase transition and polarization loop behavior on the energy storage performance of antiferroelectric $PbZrO_3$ thin films", Thin Solid Films **697**, 137794 (2020).

[112]X. Hao, J. Zhai, and X. Yao, "Improved energy storage performance and fatigue endurance of Sr-Doped $PbZrO_3$ antiferroelectric thin films", Journal of the American Ceramic Society **92**, 1133–1135 (2009).

[113]Z. Tang and X. Tang, "Structural, dielectric and optical properties of highly oriented lead zirconate thin films prepared by sol-gel process", Materials Chemistry and Physics **80**, 294–298 (2003).

[114]M. Guo, M. Wu, W. Gao, B. Sun, and X. Lou, "Giant negative electrocaloric effect in antiferroelectric $PbZrO_3$ thin films in an ultra-low temperature range", Journal of Materials Chemistry C **7**, 617–621 (2019).

[115] M. Ye, Q. Sun, X. Chen, Z. Jiang, and F. Wang, "Effect of Eu doping on the electrical properties and energy storage performance of $PbZrO_3$ antiferroelectric thin films", Journal of the American Ceramic Society **94**, 3234–3236 (2011).

[116] J. Zhai, Y. Yao, X. Li, T. F. Hung, Z. K. Xu, H. Chen, E. V. Colla, and T. B. Wu, "Dielectric properties of oriented $PbZrO_3$ thin films grown by sol-gel process", Journal of Applied Physics **92**, 3990–3994 (2002).

[117] T. Tani, J. F. Li, D. Viehland, and D. A. Payne, "Antiferroelectric-ferroelectric switching and induced strains for sol-gel derived lead zirconate thin layers", Journal of Applied Physics **75**, 3017–3023 (1994).

[118] S. S. N. Bharadwaja and S. B. Krupanidhi, "Dielectric and dc electrical studies of antiferroelectric lead zirconate thin films", Materials Science and Engineering B: Solid-State Materials for Advanced Technology **B78**, 1–10 (2000).

[119] S. S. Bharadwaja and S. B. Krupanidhi, "Growth and study of antiferroelectric lead zirconate thin films by pulsed laser ablation", Journal of Applied Physics **86**, 5862–5869 (1999).

[120] P. S. Dobal, R. S. Katiyar, S. S. N. Bharadwaja, and S. B. Krupanidhi, "Micro-Raman and dielectric phase transition studies in antiferroelectric $PbZrO_3$ thin films", Applied Physics Letters **78**, 1730–1732 (2001).

[121] K. Boldyreva, D. Bao, G. Le Rhun, L. Pintilie, M. Alexe, and D. Hesse, "Microstructure and electrical properties of $(120)_O$-oriented and of $(001)_O$-oriented epitaxial antiferroelectric $PbZrO_3$ thin films on (100) $SrTiO_3$ substrates covered with different oxide bottom electrodes", Journal of Applied Physics **102**, 044111–044111 (2007).

[122] M. D. Nguyen and G. Rijnders, "Electric field-induced phase transition and energy storage performance of highly-textured $PbZrO_3$ antiferroelectric films with a deposition temperature dependence", Journal of the European Ceramic Society **38**, 4953–4961 (2018).

[123] X. Guo, J. Ge, F. Ponchel, D. Rémiens, Y. Chen, X. Dong, and G. Wang, "Effect of Sn substitution on the energy storage properties of high (001)-oriented $PbZrO_3$ thin films", Thin Solid Films **632**, 93–96 (2017).

[124] J. Ge, D. Remiens, X. Dong, Y. Chen, J. Costecalde, F. Gao, F. Cao, and G. Wang, "Enhancement of energy storage in epitaxial $PbZrO_3$ antiferroelectric films using strain engineering", Applied Physics Letters **105**, 1–6 (2014).

[125]I. Kanno, T. Inoue, T. Suzuki, H. Kotera, and K. Wasa, "Electric field-induced strain of $PbZrO_3$ films", Japanese Journal of Applied Physics **45**, 7258–7261 (2006).

[126]B. Jaffe, W. R. Cook, and H. Jaffe, "Chapter 6 - properties of $PbTiO_3$, $PbZrO_3$, $PbSnO_3$, and $PbHfO_3$ plain and modified", in Piezoelectric ceramics, edited by B. Jaffe, W. R. Cook, and H. Jaffe (Academic Press, 1971), pp. 115–134.

[127]D. J. Singh, "Structure and energetics of antiferroelectric $PbZrO_3$", Phys. Rev. B **52**, 12559–12563 (1995).

[128]S. E. Reyes-Lillo and K. M. Rabe, "Antiferroelectricity and ferroelectricity in epitaxially strained $PbZrO_3$ from first principles", Physical Review B - Condensed Matter and Materials Physics **88**, 180102(R)–180102(R) (2013).

[129]R. Gao, S. E. Reyes-Lillo, R. Xu, A. Dasgupta, Y. Dong, L. R. Dedon, J. Kim, S. Saremi, Z. Chen, C. R. Serrao, H. Zhou, J. B. Neaton, and L. W. Martin, "Ferroelectricity in $Pb_{1+\delta}ZrO_3$ Thin Films", Chemistry of Materials **29**, 6544–6551 (2017).

[130]F. Zhongming, X. Fei, T. Goknur, C. Long-qing, and T. Xiaoli, "Interaction Dynamics Between Ferroelectric and Antiferroelectric Domains in a PbZrO 3 -Based Ceramic", Physical Review Applied **10**, 1 (2019).

[131]B. Liu, X. Tian, L. Zhou, and X. Tan, "Motion of phase boundary during antiferroelectric-ferroelectric transition in a PbZrO3 -based ceramic", Physical Review Materials **4**, `10.1103/PhysRevMaterials.4.104417` (2020).

[132]G. Shirane and S. Hoshino, " X-ray study of phase transitions in $PbZrO_3$ containing Ba or Sr ", Acta Crystallographica **7**, 203–210 (1954).

[133]O. E. Fesenko and V. G. Smotrakov, "Optic and dielectric study of lead zirconate crystals", Ferroelectrics **12**, 211–213 (1976).

[134]O. E. Fesenko, R. V. Kolesova, and Y. G. Sindeyev, "The structural phase transitions in lead zirconate in super-high electric fields", Ferroelectrics **20**, 177–178 (1978).

[135]A. V. Leyderman, I. N. Leont'ev, O. E. Fesenko, and N. G. Leon'tev, "Dipole order and stability of the ferroelectric and antiferroelectric states in lead zirconate", Physics of the Solid State **40**, 1204–1207 (1998).

[136]S. Lisenkov, Y. Yao, N. Bassiri-Gharb, and I. Ponomareva, "Prediction of high-strain polar phases in antiferroelectric $PbZrO_3$ from a multiscale approach", Physical Review B **102**, 104101 (2020).

[137] H. Fujishita and S. Katano, "Re-examination of crystal structure of $PbZrO_3$ by neurton diffraction", Journal of the Korean Physical Society **32**, 202–205 (1998).

[138] J. L. Wentz and L. Z. Kennedy, "Primary pyroelectric effect in the PZT 95/5 ceramic", Journal of Applied Physics **35**, 1767–1770 (1964).

[139] B. Xu, Y. Ye, Q. M. Wang, and L. E. Cross, "Dependence of electrical properties on film thickness in lanthanum-doped lead zirconate titanate stannate antiferroelectric thin films", Journal of Applied Physics **85**, 3753–3758 (1999).

[140] M. J. Haun, T. J. Harvin, M. T. Lanagan, Z. Q. Zhuang, S. J. Jang, and L. E. Cross, "Thermodynamic theory of PbZrO3", Journal of Applied Physics **65**, 3173–3180 (1989).

[141] I. Kanno, S. Hayashi, M. Kitagawa, R. Takayama, and T. Hirao, "Antiferroelectric PbZrO3 thin films prepared by multi-ion-beam sputtering", Applied Physics Letters **145**, 145 (1995).

[142] E. Sawaguchi, G. Shirane, and Y. Takagi, "Phase Transition in Lead Zirconate", Journal of the Physical Society of Japan **6**, 333–339 (1951).

[143] F. Jona and G. Shirane, "Optical Study of $PbZrO_3$, and $NaNbO_3$ Single Crystals", Physical Review **97**, 1584–1590 (1954).

[144] A. E. Pasto and R. A. Condrate, "Raman Spectrum of $PbZrO_3$", Journal of the American Ceramic Society **56**, 436–438 (1973).

[145] L. Pintilie, K. Boldyreva, M. Alexe, and D. Hesse, "Coexistence of ferroelectricity and antiferroelectricity in epitaxial $PbZrO_3$ films with different orientations", Journal of Applied Physics **103**, 024101–024101 (2008).

[146] H. Amorín, R. Jiménez, J. Ricote, T. Hungría, A. Castro, and M. Algueró, "Apparent vanishing of ferroelectricity in nanostructured $BiScO_3$-$PbTiO_3$", Journal of Physics D: Applied Physics **43**, `10.1088/0022-3727/43/28/285401` (2010).

[147] W. Meier, K. E. Meyer, D. F. Sava Gallis, M. A. Blea-Kirby, J. Roth, D. Felman, T. Breuer, G. J. Dension, F. J. Zutavern, W. Huebner, and G. L. Brennecka, "Highly Textured $BaTiO_3$ via Templated Grain Growth and Resulting Polarization Reversal Dynamics", Journal of the American Ceramic Society **99**, 922–929 (2016).

[148] S. Chattopadhyay, P. Ayyub, V. R. Palkar, A. V. Gurjar, R. M. Wankar, and M. Multani, "Finite-size effects in antiferroelectric nanoparticles", Journal of Physics: Condensed Matter **9**, 8135–8145 (1997).

[149] L. Kong and J. Ma, "Preparation and characterization of antiferroelectric PLZT2/95/5 thin films via a sol–gel process", Materials Letters **56**, 30–37 (2002).

[150] J. Ge, D. Remiens, J. Costecalde, Y. Chen, X. Dong, and G. Wang, "Effect of residual stress on energy storage property in $PbZrO_3$ antiferroelectric thin films with different orientations", Appl. Phys. Lett. **103**, 162903 (2013).

[151] S. Corkovic and Q. Zhang, "Correlation between critical coercive field and residual stress in antiferroelectric PZT 95/05 films", Funct. Mater. Lett. **01**, 13–18 (2008).

[152] A. Pring, B. M. Gatehouse, and W. D. Birch, "Francisite, cu3 bi(seo3)2o2 cl, a new mineral from iron monarch, south australia; description and crystal structure", American Mineralogist **75**, 1421–1425 (1990).

[153] P. Millet, B. Bastide, V. Pashchenko, S. Gnatchenko, V. Gapon, Y. Ksari, and A. Stepanov, "Syntheses, crystal structures and magnetic properties of francisite compounds $Cu_3Bi(SeO_3)_2O_2X$ (X = Br, Cl, I)", J. Mater. Chem. **11**, 1152–1157 (2001).

[154] M. I. Aroyo, D. Orobengoa, G. de la Flor, E. S. Tasci, J. M. Perez-Mato, and H. Wondratschek, "Brillouin-zone database on the *Bilbao Crystallographic Server*", Acta Crystallographica Section A **70**, 126–137 (2014).

[155] V. Gnezdilov, Y. Pashkevich, P. Lemmens, V. Kurnosov, P. Berdonosov, V. Dolgikh, E. Kuznetsova, V. Pryadun, K. Zakharov, and A. Vasiliev, "Lattice and magnetic instabilities in $Cu_3Bi(SeO_3)_2O_2X$ (X = Br, Cl)", Phys. Rev. B **96**, 115144 (2017).

[156] P. S. Berdonosov and V. A. Dolgikh, "Copper lanthanide selenite oxohalides with francisite structure: Synthesis and structural characteristics", Russian Journal of Inorganic Chemistry **53**, 1353–1358 (2008).

[157] K. V. Zakharov, E. A. Zvereva, M. M. Markina, M. I. Stratan, E. S. Kuznetsova, S. F. Dunaev, P. S. Berdonosov, V. A. Dolgikh, A. V. Olenev, S. A. Klimin, L. S. Mazaev, M. A. Kashchenko, M. A. Ahmed, A. Banerjee, S. Bandyopadhyay, A. Iqbal, B. Rahaman, T. Saha-Dasgupta, and A. N. Vasiliev, "Magnetic, resonance, and optical properties of Cu3Sm(SeO3)2O2Cl: A rare-earth francisite compound", Physical Review B **94**, 1–11 (2016).

[158] M. M. Markina, K. V. Zakharov, P. S. Berdonosov, V. A. Dolgikh, E. S. Kuznetsova, S. A. Klimin, O. B. Yumashev, and A. N. Vasiliev, "Thermodynamic properties and rare-earth spectroscopy of Cu3Nd(SeO3)2O2X (X=Cl, Br)", Journal of Magnetism and Magnetic Materials **492**, `10.1016/j.jmmm.2019.165721` (2019).

[159] R. Becker and M. Johnsson, "Crystal structure of Cu3Bi(TeO3)2O2Cl: a Kagomé lattice type compound", Solid State Sciences **7**, 375–380 (2005).

[160] K. H. Miller, P. W. Stephens, C. Martin, E. Constable, R. A. Lewis, H. Berger, G. L. Carr, and D. B. Tanner, "Infrared phonon anomaly and magnetic excitations in single-crystal $Cu_3Bi(SeO_3)_2O_2Cl$", Phys. Rev. B **86**, 174104 (2012).

[161] M. Pregelj, O. Zaharko, A. Günther, A. Loidl, V. Tsurkan, and S. Guerrero, "Magnetic ground state and two-dimensional behavior in pseudo-kagome layered system $Cu_3Bi(SeO_3)_2O_2Br$", Phys. Rev. B **86**, 144409 (2012).

[162] I. Rousochatzakis, J. Richter, R. Zinke, and A. A. Tsirlin, "Frustration and Dzyaloshinsky-Moriya anisotropy in the Kagome francisites $Cu_3Bi(SeO_3)_2O_2X$ (X = Br, Cl)", Phys. Rev. B **91**, 024416 (2015).

[163] V. Gnezdilov, Y. Pashkevich, V. Kurnosov, P. Lemmens, E. Kuznetsova, P. Berdonosov, V. Dolgikh, K. Zakharov, and A. Vasiliev, "Longitudinal magnon, inversion breaking and magnetic instabilities in the pseudo-kagome francisites $Cu_3Bi(SeO_3)_2O_2X$ with X = Br, Cl", arXiv:1604.04249v1 (2016).

[164] D. A. Prishchenko, A. A. Tsirlin, V. Tsurkan, A. Loidl, A. Jesche, and V. G. Mazurenko, "Antiferroelectric instability in the kagome francisites $Cu_3Bi(SeO_3)_2O_2X$ (X = Br, Cl)", Phys. Rev. B **95**, 064102 (2017).

[165] A. Girard, H. Taniguchi, S. M. Souliou, M. Stekiel, W. Morgenroth, A. Minelli, A. Kuwabara, A. Bosak, and B. Winkler, "Competing structural instabilities in Bi_2SiO_5", Phys. Rev. B **98**, 134102 (2018).

[166] R. Blinc and B. Žekš, Soft modes in ferroelectrics and antiferroelectrics (American Elsevier publishing company, 1974).

[167] E. K. H. Salje, M. C. Gallardo, J. Jimenez, F. J. Romero, and J. d. Cerro, "The cubic-tetragonal phase transition in strontium titanate: excess specific heat measurements and evidence for a near-tricritical, mean field type transition mechanism", J. Phys.: Condens. Matter **10**, 5535–5543 (1998).

[168] M. A. Carpenter, "Elastic anomalies accompanying phase transitions in $(Ca,Sr)TiO_3$ perovskites: Part I. Landau theory and a calibration for $SrTiO_3$", Am. Mineral. **92**, 309–327 (2007).